Investigation and Mitigation of Powder Anomalies Induced Porosity in Powder Bed Additive Manufacturing

Submitted in partial fulfillment of the requirements for

the degree of

Doctor of Philosophy

in

Materials Science and Engineering

Ziheng (Dino) Wu

B.S., Materials Engineering, Purdue University

M.S., Materials Science & Engineering, Carnegie Mellon University

Carnegie Mellon University
Pittsburgh, PA

December, 2021

Dedicated to my family,

Xiaoqun, Cong, and Danli

Abstract

Defect content is one of the major obstacles to the wider adoption of additive manufacturing (AM) as the field is still actively learning how to control it, developing standards to quantify it, and building up knowledge of its formation and impacts. On the other hand, there is a growing interest in reducing AM fabrication cost by using recycled materials and economically produced powder. State-of-the-art powder-based AM processes typically accept gas-atomized spherical powder with low entrapped gas porosity. However, using non-standard powder feedstock, e.g., the non-spherical hydride-dehydride (HDH) Ti-6Al-4V powder and the highly porous 17-4 PH stainless steel powder, can be more cost-efficient. This work presents two successful applications of the non-standard feedstocks through process optimization by measuring the process windows for the fully dense components and achieving comparable mechanical properties as the standard AM counterparts. Additionally, the author used synchrotron-based high-speed imaging technique to visualize and quantify the porosity formation processes induced by the anomalies of the non-standard powders, i.e., irregular morphology and powder porosity. By coupling them with pore shape analysis and powder packing analysis, three powder induced porosity formation mechanisms were proposed. Melt pool dynamics, powder packing characteristics, and powder-laser interactions are believed to be the key factors for powder induced porosity formation. The optimization guideline and the better understanding of the porosity formation can certainly be generalized for the application of other non-standard feedstocks which could benefit the AM community.

Acknowledgements

It has been a great run! The Ph.D. career has been the most amazing journey in my life so far. It was about the teamwork and about the process. For the many people who offered me help and wisdom, it was you who made the process enjoyable and turned me into a better version of myself. The first person I would like to acknowledge is my advisor Professor Anthony Rollett. Thanks for your patience and guidance. It was you who showed me a model of a good researcher by being one. Your passion for science and your constant excitement for new ideas and new techniques are incredibly valuable gifts for me to imitate in research and in my life. I am very grateful to have Dr. Sandra DeVincent Wolf in my committee. She helped me develop my future goal by offering invaluable career advice and gave me many opportunities to practice my skills and build my reputation. She taught me the importance of sharing and exposing research works and networking. I truly enjoy working with you and hope someday I can be a great program manager like you. I would also like to thank the rest of my committee, Dr. Bryan Webler, Dr. Jack Beuth, and Dr. Tao Sun for their time to give constructive criticism and help me present a full story in this thesis.

Next, I would like to thank Todd Baer for all his help on sample fabrication. Without your help, this work would not be possible. I appreciate Dr. Sneha Prabha Narra for her guidance and collaboration, which shortened my learning curve of conducting AM research, at the beginning of my Ph.D. career. I would also like to thank all my collaborators who made significant contributions to this work: Dr. Benjamin Gould, Muktesh Paliwal, Joe Capone, John Meyer, and Elizabeth Larson. Your ideas and feedback were critical for the several publications directly resulted from this work. Additionally, I would like to thank Dr. Amir Mostafaei and Mohammadreza Asherloo for their direct contributions and future collaborations on the topic of

hydride-dehydride powder. Dr. Xianghui Xiao, Dr. Pavel Shevchenko, and all the 2-BM beamline staff at the Advanced Photon Source are thanked for assisting in the acquisition of the synchrotron tomography data. Dr. Niranjan Parab, Dr. Cang Zhao and all the 32-ID beamline staff at the Advanced Photon Source are thanked for assisting in the acquisition of the DXR data.

It has been an honor to spend my graduate career in the Carnegie Mellon research community with many talents who passionate about science and engineering, especially the Rollett Group. I enjoyed every moment with my colleagues in Doherty A306 where facilitated many debates and curated many great ideas. I would like to thank Christopher Kantzos, Rachel Lim, Joseph Pauza, Matthew Wilkin, Debomita Basu, Ruby Jiang, Joseph Aroh, Lonnie Smith, Srujana Rao Yarasi, Nicholas Lamprinakos, Junwon Seo, Nihal Sivakumar, Robin Kuo as well as the rest of the group for their support.

Lastly, I would like to thank my parents, Xiaoqun and Cong, and my families who encouraged me to pursue a career in science and gave me unlimited support. I would also like to thank my partner Danli Luo and my friend Dian Yu who offered countless encouragements to help me traverse the ups and downs in my life.

This work is supported by several grants and agencies. This HDH work is supported by the Pennsylvania Infrastructure Technology Alliance, a partnership of Carnegie Mellon, Lehigh University and the Commonwealth of Pennsylvania's Department of Community and Economic Development (DCED). The author recognizes Reading Alloys (formerly affiliated with AMETEK Inc., now a part of Kymera International), especially Mike Marucci, for providing the Ti-6Al-4V powder used in this work and their assistance with the study. The author acknowledges the support of the NextManufacturing Center and the use of the Materials Characterization Facility, supported by grant MCF-677785, at Carnegie Mellon University. This

research used resources of the Advanced Photon Source, a US Department of Energy (DOE) Office of Science User Facility operated for the DOE Office of Science by Argonne National Laboratory under Contract No. DE-AC02-06CH11357 in addition to support through Laboratory Directed Research and Development (LDRD) funding from Argonne National Laboratory under the same contract.

Ziheng (Dino) Wu

Pittsburgh, PA

Oct 2021

List of Publications

The following publications directly contributed to this thesis:

1. Z. Wu, S. Rao Yarasi, A. Mostafaei, A.D. Rollett, (2020). Powder characterization for metal additive manufacturing, *ASM handbook, Volume 24*, Additive Manufacturing Processes, Ed. D. Bourell, W. Frazier, H. Kuhn, M. Seifi, ASM International.
2. S.P. Narra, Z. Wu, R. Patel, J. Capone, M. Paliwal, J. Beuth, A.D. Rollett, (2020). Use of non-spherical hydride-dehyride (HDH) powder in powder bed fusion additive manufacturing, *Additive Manufacturing*, *34, 101188*.
3. Z. Wu, D. Basu, J. Meyer, E. Larson, R. Kuo, J. Beuth, A. Rollett, (2020). Study of powder gas entrapment and its effects on porosity in 17-4 PH stainless steel parts fabricated in laser powder bed fusion, *JOM, 73*, 177 – 188.
4. D. Basu, Z. Wu, E. Larson, J. Meyer, R. Kuo, A. Rollett, (2021). Entrapped gas and process parameter induced porosity formation in additively manufactured 17-4 PH stainless steel, *Journal of Materials Engineering and Performance*, 1-8.
5. Z. Wu, M. Asherloo, R. Jiang, M. Delpazir, N. Sivakumar, J. Capone, B. Gould, A. Rollett, A. Mostafaei, (2021). Study of printability and porosity formation in laser powder bed fusion built hydride-dehydride (HDH) Ti-6Al-4V, *Additive Manufacturing*, *47, 102323.*

Table of Contents

List of Figures

List of Tables

List of Abbreviations

AM – Additive Manufacturing

APS – Advanced Photon Source

ANL – Argonne National Laboratory

BFE – Basic Flowability Energy

CT – Computed Tomography

DoE – Design of Experiment

DXR – Dynamic X-ray Radiography

EBAM – Electron Beam Additive Manufacturing

EB-PBF – Electron Beam Powder Bed Fusion

EDM – Electrical Discharge Machining

EIGA – Electron Induction Melting – Gas Atomization

ESD – Equivalent Spherical Diameter

FO – Focus Offset

FOV – Field of View

FT– Fourier Transform

GA – Gas Atomization

HDH – Hydride-Dehydride

HIP – Hot Isostatic Pressing

HS – Hatch Spacing

IPS – Induction Plasma Spheroidization

LD – Laser Diffraction

L-PBF – Laser Powder Bed Fusion

PBF – Powder Bed Fusion

PREP – Plasma Rotating Electrode Process

PSD – Powder Size Distribution

P-S – Plasma Spheroidization

P-V – Power-Velocity

SE – Specific Energy

SEM – Scanning Electron Microscopy

SF – Speed Function

SI – Stability Index

μXCT – Micro X-ray Computed Tomography

1. Background

1.1. Powder Bed Additive Manufacturing

Over the past three decades, additive manufacturing (AM) has been one of the fastest-emerging manufacturing technologies. Growing demand exists in various fields, e.g., aerospace, medical, and automotive, based on multiple advantages gained by adopting AM, such as minimizing tooling cost, increasing buy-to-fly ratio, reducing product development cycle, and advancing product innovation by enabling designs with more complex geometry [1]. There are a variety of commercially available metal AM systems which can be categorized based the heat source and material feedstock. Common heat source includes laser, electron beam, and arc, and common material feedstock include powder bed, powder stream and wire feed.

Powder bed fusion (PBF) processes are suitable for parts with small build volume < 0.01 m^3 and hundreds of micrometer in resolution [1]. In most of the PBF processes, the operation follows a repeated sequence of i) the build platform moves down by a set layer thickness, ii) the rake/recoater blade fetches powder onto the build platform, iii) the overhead energy source fuses powder, until a 3D part is complete. Among all the metal AM technologies, electron beam additive manufacturing (EBAM) and laser powder bed fusion (L-PBF) are the two most established powder bed fusion processes currently.

1.1.1. Laser Powder Bed Fusion

The high popularity of the L-PBF process is mainly due to the achievable fine feature resolution, its technical maturity, and wide spectrum of commercially available machines. As suggested by the name, L-PBF process utilizes a laser, sometimes multiple lasers, as the energy

source to fuse powder on the powder bed following the aforementioned sequence. L-PBF process normally operates at a preheat lower than 500°C and in an argon or nitrogen environment.

One of the biggest challenges in L-PBF process originates from the fast cooling. The high cooling rate (~ 10^5 K/s) acting together with the remelting cycles and the large thermal gradients leads to thermal distortion and hot cracking which constrain alloy choice and geometrical design. A solution to counteract the effects from residual stress is to add support structures to anchor parts to the build plate. Unlike in EBAM system, the supports in L-PBF process are intended to bear load, meaning they are usually stronger and thicker but more difficult to be removed. The residual of the supports can affect the surface quality of the as-built parts which is concerning for surface sensitive applications. Many active researches [2] are currently developing novel methods for support removal. Sectioning as-built parts with residual stress from the build plate can potentially damage the parts. Thus, stress relief heat treatment in an inert gas environment is normally conducted prior to sectioning of parts from the baseplate.

Typical powder feedstock in L-PBF sizes ranging from 15 to 45 μm [3–5] and has spherical morphology. Commercially available materials for L-PBF fabrication includes Ti-6Al-4V, IN718, AlSi10Mg, stainless steels, maraging steel, CoCr alloys, etc.

1.1.2. Electron Beam Additive Manufacturing

Arcam AB, now GE Additive, is the only manufacturer of commercial use EBAM systems on the market. Arcam took a different approach to realize the concept of metal additive manufacturing by using an electron beam as the heat source instead of a laser. Because electron beam can move several orders faster than laser can, it certainly provides greater potentials for EBAM process to improve build rate/productivity. However, the usage of election beam results in complete different challenges for EBAM process to fabricate quality parts.

One of the biggest challenges is the issue of *smoke*, which refers the plume of charged powder particle ejected from the powder bed where the electron beam scans. *Smoke* is similar to the powder spattering in L-PBF process but in a much more chaotic manner. As the electrons are being decelerated by the powder bed, their kinetic energy converts into thermal energy which is the desired energy form to sinter/melt the feedstock as well as the undesired potential energy of powder particle which ejects powder off the powder bed [6]. At the same energy level, electron has much larger momentum in contrast to photons in laser light due to the measurable difference in mass. Additionally, electrons accumulate in the powder bed to cause the repelling of the negatively charged powder particles leading to more severe powder ejection during the scanning process [7]. Sigl *et al*. [6] have shown that the repulsive force between two adjacent powder particles is on the order of 10^{-6} N while the weight of a powder particle is on the order of 10^{-9} N assuming that an electron beam irradiates a specific region with 100 W power for 1 s. Apparently, severe *smoke* is detrimental to the quality of each powder layer, and it potentially introduces processing defects into the as-built parts and causes termination of a building process.

To mitigate the issue of *smoke*, many aspects of EBAM process were set up based on two essential ideas - i) improve electrical conductivity and ii) increase the energy barrier to eject particles from the powder bed. EBAM process operates at a high preheat temperature, i.e., > 700°C, in a controlled vacuum environment with small partial pressure of helium. The vacuum minimizes electron scattering and the addition of helium improves the electrical and thermal conductivity [8]. Besides the high preheat, the electron beam pre-sinters the powder bed with a low-power and low-speed setting. This step forms necks between particles to increase the number of pathways for electron dissipation and increase the weight of a single entity. Since little residual stress accumulates in the as-built EBAM parts due to the high preheat, no support

structure is needed to prevent thermal distortion; however, support structures are often used to prevent localized heat accumulation by offering additional channels for heat dissipation.

The feature resolution of the EBAM process, i.e., ~ 500 µm, is slightly coarser than that of the L-PBF process mainly due to the coarser feedstock size (45 – 106 µm) and the larger melt pool formed at high preheat. Compared with the alloys that can be fabricated in L-PBF process, the alloys available for EBAM process are limited including Ti-6Al-4V, CoCr, IN718, and titanium aluminide.

1.2. Powder for Additive Manufacturing

Metal powder has been used in various processes long before the advent of AM, including cold/hot isostatic pressing, press sintering, and injection molding [9]. The initial titanium powder 'sponge fines' are reduced from titanium tetrachloride or rutile using sodium/magnesium reduction so-called Hunter/Kroll process [10]. AM metal powder being expensive is mainly due to the high energy input in powder production and the low yield efficiency of powder with a suitable size distribution for AM application (< 100 µm). The yield efficiency of powder < 45 µm in a free-fall gas atomization process can be as low as 10 % [11]. Depending on the alloy properties, AM metal powder can be produced using methods like gas atomization (GA) [12], electron induction melting – gas atomization (EIGA) [13], plasma rotating electrode process (PREP) [14], induction plasma spheroidization (IPS) [15], water atomization [16], and hydride-dehydride process (HDH) [17,18].

1.2.1. Gas Atomized Powder for Additive Manufacturing

GA developed by Crucible Materials Corporation in 1980s [19] is the most popular production process for metal AM powder as of today. It utilizes high-velocity inert gas flow to disperse molten metal, which solidifies to spherical powder during falling as a result of surface

tension [20]. Three common configurations of GA are freefall, close-coupled and electrode-induction. Both the free-fall and the close-coupled atomization processes use molten pre-alloyed metal from a tundish. The close-coupled process improves the fine powder yield rate by applying pressurized gas right at the nozzle outlet. In the electrode-induction process, the tundish with molten metal is replaced by an induction coil and a metal rod [4].

1.2.2. Hydride-Dehydride Powder for Additive Manufacturing

HDH process is a chemical plus mechanical method of producing titanium powder from titanium ingot, billet, or scrap by utilizing the brittle nature of the hydrogenated titanium and the reversible reaction between titanium and hydrogen [21]. The process first hydrogenates and embrittles the prealloyed Ti-6Al-4V at above 700°C in a hydrogen atmosphere. This results in the formation of the friable intermetallic δ hydride phase, which is later milled into fine particles mechanically. The exothermic reaction ensures that the hydriding process is self-sustaining and further reduces energy consumption. The milled titanium hydride powder is then heated at an elevated temperature, 350 °C – 700 °C, in a vacuum environment until the hydrogen is fully released [17]. The particle size distribution (PSD) of HDH versus atomized powder in a given sieve range can be significantly different because of the different morphology. For instance, elongated HDH powder particles can easily fall through a fine mesh pore in the sieving process along the longer dimensions. It is often expected that the irregular morphology can result in poor powder packing and lower flowability. Therefore, plasma spheroidization is typically used to change the irregular particle morphology to spherical. However, the plasma spheroidization step adds to the cost of the powder.

Attempts have been made in the past to use non-spherical powder in powder bed AM processes. Guzmán *et al*. [22] generated a process map for fabrication using non-spherical HDH

Ti-53%Nb powder in a L-PBF process. Medina [20] and Kanou *et al*. [23] attempted to improve the density and tensile property of the as-built parts by blending angular HDH Ti-6Al-4V powder with spherical powder at different ratios in an electron beam powder bed fusion (EB-PBF) process. Xu *et al*. [24] successfully used HDH CP-Ti powder in a L-PBF process and demonstrated that the tensile property of the L-PBF built CP-Ti outperformed the as-cast CP-Ti and Ti-6Al-4V. However, the study focused on improving the flowability and spheroidicity of the HDH powder through prior ball milling. Yang *et al*. [25] applied both powder mixing approach and powder post-processing treatment to the fabrication of CP-Ti powder and identified an optimal blending ratio to achieve the best tensile performance. Powder mixing or post-processing steps, e.g., spheroidization, can certainly improve the powder uniformity to approximate the behaviors of powder atomized from the standard powder production techniques but inevitably increases the cost of the feedstock. There were also successful attempts of using non-spherical water atomized powder in L-PBF processes. Li *et al*. [26] concluded that the lower packing density and the higher oxygen content in the water atomized powder as compared with the gas atomized powder resulted in higher levels of porosity in the as-fabricated parts. This study mainly explored the pore formation mechanism in the L-PBF process but did not discuss parameter optimization to improve part density. More recent work by Rogalsky *et al*. [27] demonstrated a successful use of the water atomized powder to fabricate bulk parts and reported that the poor packing density affected the laser absorptivity which in turn altered the porosity content and the as-built microstructure. Another recent work by Fullenwider *et al*. [28] discussed the use of ball milling to convert machining chips to feedstock powder for AM application. The milled powder shared similar morphology as the HDH powder and was used to deposit single-bead melt tracks successfully. This study not only showed significant implications for

recyclability, but also demonstrated the advantages of being able to fabricate using alternative feedstock with irregular morphology. In summary, the efforts in this area are up and coming, and only limited work is available to lower the costs of the AM process by reducing the costs associated with the feedstock materials.

1.3. Defects in Additive Manufacturing

1.3.1. Defects in Powder-Based Additive Manufacturing

Despite many advantages gained by adopting AM, the transition from conventional manufacturing techniques is often not straightforward since many challenges cannot be anticipated. The non-steady state nature of AM imposed during repeated thermal spikes [29] and spatially and temporally varying control variables can induce defects and undesirable anisotropy. Many standards developed based on conventional manufacturing techniques are not applicable to AM parts; thus, this posts a major challenge for the adoption of AM technologies. As of now, many companies and researchers are actively developing new standards to qualify AM built parts.

Minimizing defect content in an AM component remains one of the first milestones when printing a new material. These defects are well-documented [30,31] stress concentration and crack initiation sites that can negatively impact the mechanical performance of AM parts, especially ductility and fatigue life. A fundamental understanding of the defect formation mechanisms, and its application to process controls to enable the fabrication of defect free parts, is essential to the commercial adoption of AM. Based on the formation mechanism, there are two major sources of defects in metal AM components – defects that arise during processing and those that originate from the feedstock.

Processing defects are often induced by suboptimal energy density. Excessive energy input leads to unstable keyhole penetration that gives rise to the formation of spherical keyhole pores [32–34]. Prior studies have used a criterion which compares the depth of a melt pool with its half-width to identify the keyholing condition [35,36]. The work of Francis [36] used this criterion to demonstrate that keyholing could be avoided by increasing the ratio of the laser spot to the melt pool width. By contrast, irregularly shaped lack-of-fusion porosity [37–39] forms owing to insufficient energy density often caused by high laser speed, low laser power, large layer thickness, or large hatch spacing. The geometry-based criterion developed by Tang *et al*. [40] provides a simple guideline to avoid the lack-of-fusion regime by estimating melt pool overlap when selecting process parameters.

Defects from feedstock [41], including powder entrapped gas, are often neglected as the resulting porosity is relatively small in size and low in concentration. This particular defect originates in gas atomization, which supplies the majority of powder for metal AM applications. In gas atomization, a continuous liquid metal stream flows through a nozzle and is disintegrated into droplets by a supersonic gas flow, commonly of argon or nitrogen. After exiting the supersonic gas flow structure, molten droplets spheroidize due to surface tension and rapidly solidify. The entrapped gas is sometimes unable to escape before solidification [42]. Cunningham *et al*. [43] have shown the thermally induced re-growth of entrapped gas porosity in Ti-6Al-4V when a hot isostatic pressed (HIP) component was exposed to elevated temperature. However, being able to control entrapped gas porosity is still attractive when an incremental gain in toughness or ductility can help to meet the stringent requirements for manufacturing components that are subject to high-temperature exposure in service or when HIP is too costly.

1.3.2. Characterization of Porosity Using X-Ray Techniques

Many efforts attempted to tackle the porosity formation problem using different approaches. Tan *et al*. [44] and Khairallah *et al*. [45] have developed multi-scale modeling tools which can capture the complex physics, e.g., heat transfer and fluid flow, in the melt track and simulate porosity formation and microstructure evolution. Many studies [46,47] tried to connect, control and predict porosity formation with signals emitted during AM fabrication, e.g., acoustic wave, image, and thermal signature. The current study uses synchrotron-based x-ray techniques to visualize internal defects and to understand porosity formation at a finer resolution which are impossible to be accomplished in a different way.

Computed tomography (CT) is a widely used research technique for dimensional measurement [48] and porosity analysis [49] in AM parts. This nondestructive method can reveal and quantify the spatial distribution, morphology, and size of internal features in 3D which is unmatched by other 2D characterization techniques. Thanks to the higher flux and energy, the synchrotron-based micro x-ray computed tomography (μXCT) can shorten the data acquisition time, enable a larger penetration depth, and achieve a finer feature resolution compared with the lab-scale CT albeit for samples limited to ~1 mm on a side. Tammas-Williams *et al*. [50] used CT to reveal the presence of entrapped gas porosity in powder particles and demonstrated the influence of process parameters on in-part porosity population in the EBAM process. Later, Cunningham *et al*. [51] used synchrotron-based μXCT to conclude that the populations of entrapped gas pores in powder and in the corresponding as-built parts were correlated based on the similarity of their size distributions. Several other studies [34,52–54] utilized CT to visualize internal anomalies in various AM processes and alloys to investigate the roles played by other

aspects of AM in defect formation, e.g., part geometry, post-processing, powder spreading, process parameters, etc.

μXCT is an attenuation-based x-ray technique which conveys information about physical density and atomic mass through the contrast on projections, i.e., a darker region corresponds to higher absorption. In a μXCT experiment, an x-ray beam irradiates a sample while it rotates with a small, fixed step size. The transmitted x-rays form a sinogram on a detector at each angular step until a half-turn is complete. The subsequent sinograms undergo a reconstruction process [55], generally via filtered back-projection, to generate horizontal 2D slices of the object which are later stacked together to arrive at a 3D image of the illuminated object. In μXCT measurement, the field of view (FOV), penetration depth, and spatial resolution are competing interests; larger FOV enables detection of larger, less common features which require sampling a larger volume while higher resolution favors detection of smaller, more common features which are still likely to be observed even for the reduced sample volume and FOV required to increase resolution. Many studies [56,57] discussed the reliability and accuracy of the measurement from μXCT by comparing it with other techniques. Reasonable agreement has been shown if a balanced magnification is chosen in accordance with the size of the interested feature.

Dynamic x-ray radiography (DXR) is a powerful tool for studying the dynamics during the rapid melting and solidification in L-PBF. In this method of characterization, an x-ray beam penetrates from the side of a powder bed where the laser scans across. The x-rays impinge on a scintillator which converts them to visible light while a high-speed camera, placed a fixed distance away from the sample, captures full field x-ray images [58,59]. More details of the experimental setup used in this work are outlined in section §2.2.3. Coupling x-ray radiography with high-speed imaging enables observation of *in-situ* interactions between the laser and

metal/powder [60]. Zhao *et al*. [61] and Cunningham *et al*. [32] identified the thresholds and the non-linear boundaries for the transition of melt pool from the conduction mode to the stable and unstable keyhole modes. They offered important insights into porosity formation and its correlation with process parameters in different regimes. Chiang *et al*. [62] studied hot cracking in an aluminum alloy by using DXR to visualize the initiation and propagation of cracks during rapid solidification. Many studies [63–66] used this technique to explain the dynamics of porosity formation, such as keyhole collapse, laser turnaround, and powder oxidation. Researchers also found valuable insights about other facets of AM such as phase transformation [67], powder spreading [68], and powder-spatter ejection [69] by using modified setups. Without the fine spatial and temporal resolutions offered by DXR, many of these hypotheses and phenomena would be difficult to test.

1.4. Materials

1.4.1. Ti-6Al-4V

The workhorse alloy in AM production, Ti-6Al-4V, is widely applied in aerospace industry [70,71] due to the outstanding mechanical properties (high strength-to-weight ratio) and corrosion resistance; it is also used in biomedical industry, mostly used for body prostheses and orthopedic implants, due to the well-studied biocompatibility [72,73]. The addition of vanadium partially stabilizes the β phase which makes Ti-6Al-4V a α + β alloy at room temperature with volume fractions about 90 %/10 %, respectively [74,75]. The as-built microstructure of Ti-6Al-4V strongly depends on the cooling rate of an AM process [76–78]. Fast cooling rate suppresses the diffusional phase transformation from β to α and instead drives the formation of a strained martensitic microstructure [3,79–81]. In the as-built condition of L-PBF, the α + β Ti-6Al-4V alloy contains mainly metastable α’ martensite [82,83] since the material experiences

diffusionless and displacive transformation at the high cooling rates obtained [79,84], and a small fraction of the orthorhombic α'' [84,85] in the vanadium-rich areas. Any subsequent heat treatment, however, modifies the microstructure to a predominantly basketweave type. By controlling the energy input and scan strategies during fabrication, studies [86,87] have also demonstrated the capability of producing fine lamellar (α + β) microstructures in the as-built component. By contrast, the EBAM process has much lower cooling rates and smaller thermal gradients due to the high preheat. The matrix of the as-built EBAM microstructure is primarily α + β meaning the as-built EBAM part exhibits lower strength but higher ductility compared with parts from L-PBF processes [3,80,88,89]. An important feature is the columnar prior β grain which makes the microstructure of the AM Ti-6Al-4V easily differentiated from conventionally manufactured microstructures. In AM processes, epitaxial growth is the dominant solidification mode meaning the β grain preferentially grows along one of the variants of the <100> crystal orientation which closely aligns with the largest thermal gradient [90]. Thijs *et al*. [79] and Narra *et al*. [91] have demonstrated the capability of varying the directional grain growth and the local grain size in different AM processes by controlling the scanning strategy.

1.4.2. 17-4 PH Stainless Steel

17-4 PH is a martensitic stainless steel which is precipitation strengthened by the addition of 4 % copper and the standard H900 heat treatment. As one of the earliest commercialized alloys in AM, 17-4 PH steel is widely used as a structural material in marine environments and power plants thanks to its superior corrosion resistance and strength. The common phases are austenite and martensite in 17-4 PH steel. Murr *et al*. [92] pointed out that the microstructure of the as-built 17-4 PH steel, e.g., the balance between martensitic and austenitic phases, depends on the atomization and AM fabrication atmospheres, e.g., nitrogen versus argon, and the

resulting nitrogen in the part since nitrogen is known as an austenite stabilizer. Many other aspects, e.g., parameter optimization, mechanical behavior, heat treatment, and microstructure of the AM built 17-4 PH stainless steel have been extensively discussed in the literature [93–95].

2. Experimental Methods

2.1. Parameter Optimization in Powder-Based Additive Manufacturing

All the as-built AM specimens were fabricated using the Arcam S12 EBAM process and the EOS M290 L-PBF process at Carnegie Mellon University. The as-built solid specimens contained various porosity levels which offered samples for the investigation of the formation mechanisms and revealed the pathway to the optimal parameter set. The parameter optimization used the standard process map approach which was first purposed by Beuth *et al*. [96]. The essential idea of this approach is to map the process outcomes, e.g., porosity content and grain size, in a space of process variables and to provide a direct visualization of regions representing different mechanisms. In the case of porosity, the common regions include keyhole, lack-of-fusion, balling, and process window.

Parameter optimization started with using the Rosenthal analytical solution [97] to estimate the melt pool size based on the process settings and alloy properties as follows

$$T_f = T_0 + \frac{Q\epsilon}{2\pi kr}\exp\left[-\frac{V(\xi + r)}{2\alpha}\right]$$

where T_f is the melting temperature, T_0 is the preheat temperature, Q is the laser power, V is the laser velocity, α is the thermal diffusivity and ϵ is the laser absorptivity. The melt pool geometry is described by ξ and r, where r is the melt pool radius and ξ is the distance from the heat source measured along the centerline.

Many criteria can be used to ensure that the selected parameter matrix sufficiently covers areas of the process space where different defect formation mechanisms, e.g., lack-of-fusion, balling, powder induced porosity, are dominant. In this study, only the lack-of-fusion criterion was used to assist the parameter selection. Based on the estimated melt-pool size, the lack-of-

fusion criterion developed by Tang *et al*. [40] can identify the potential boundary between the process window and the lack-of-fusion region as follows

$$\left(\frac{H}{W}\right)^2 + \left(\frac{L}{D}\right)^2 \leq 1$$

where H is the hatch spacing, W is the melt-pool width, L is the layer thickness, and D is the melt-pool depth. The criterion suggests that lack-of-fusion porosity forms when the melt pools at selected size and arrangement are not sufficient to cover the prescribed area.

For the parameter optimization in the EBAM process, the aforementioned calculations were not directly applicable since the process parameters were implicit, e.g., speed function. Additionally, the melt pool estimation using the Rosenthal analytical solution is not reliable since materials have different absorptivity when interacting with an electron beam; furthermore, the larger spot size in the EBAM process may invalidate the assumption of point heat source in the calculation.

2.2. Synchrotron-Based X-Ray Techniques

This section was adapted from the publication of Wu *et al*., Powder Characterization for Metal Additive Manufacturing published in ASM Handbook, Volume 24, Additive Manufacturing Processes (2020).

2.2.1. X-Ray Microtomography (μXCT)

μXCT is an attenuation-based x-ray technique which uses x-rays to illuminate an object from different directions and reconstructs the object in 3D form based on a series of sinograms. The contrast on the 2D sinograms reflects the different intensities of transmitted x-rays which depend on the integrated attenuation coefficient [98]:

$$I = I_0 exp\ (-\mu x)$$

where I is the transmitted x-ray intensity, I_0 is the intensity of the incident x-ray beam, μ is the linear attenuation coefficient (cm^{-1}) and x is the thickness of the object. The linear attenuation coefficient reflects the energy loss of the transmitted x-ray beam, also known as the amount of the photons were absorbed or scattered when the x-ray was traveling through the object. The coefficient is positively correlated with atomic number and depends on the density of the object [98]:

$$\mu = \left(\frac{\mu}{\rho}\right)\rho$$

where μ is the linear attenuation coefficient (cm^{-1}), $\left(\frac{\mu}{\rho}\right)$ is the mass attenuation coefficient (cm^2/g) and ρ is the density. Additionally, the linear attenuation coefficient also depends on the energy level of the x-ray beam since photons with lower energy are more likely to interact with the imaging object. By integrating the full spectrum of the x-ray beam energy into the linear attenuation coefficient, the transmitted x-ray intensity can be re-expressed as:

$$I = \int I_0(E)e^{-\mu(E)x}\,dE$$

where $I_0(E)$ and $\mu(E)$ represent the integrations of the initial beam intensities and the linear attenuation coefficients across all energy levels of the x-ray beam.

In a common μXCT setup, the three essential components - x-ray source, sample stage, and detector - are aligned along with the incident x-ray beam. Depending on the setup, either the sample stage or x-ray source and detector rotates through a full/half cycle to ensure sinograms are collected from all angles. Common beam types include parallel beam, pencil beam and fan (2D)/conical (3D) beam [99].

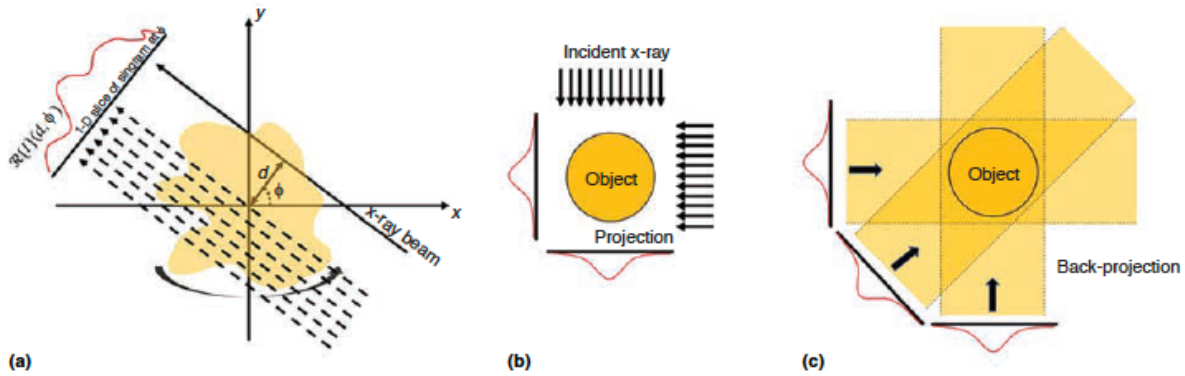

Figure 2.1(a) Schematic of an object illuminated by an x-ray beam shows the parameters used in the Radon transform. The subsequent schematics show (b) the one-dimensional (1-D) x-ray projection from a two-dimensional (2-D) cross-section of an object and (c) the back-projection reconstruction by placing the projections at their original projection angle.

In μXCT, the projection at each angle is the Radon transform of the object along the projection line. The Radon transform $\mathcal{R}$, named after Johann Radon, is an important concept in tomographic reconstruction as it describes how to map an object onto the projections as follows [100,101]:

$$\mathcal{R}\{I\}(d,\phi) = \int_{\mathcal{R}} I(d\cos\phi - s\sin\phi, d\sin\phi + s\cos\phi)ds$$

where I is the transmitted x-ray controlled by the attenuation coefficient, d is the distance from the x-ray beam to the center of the object, ϕ is the angle between the beam normal and the arbitrary x-axis and s is the direction along the x-ray as shown in Figure 2.1. Stacking the projection at each angle results in a sinogram in which one axis indicates the position on the detector and another axis indicates the angle ϕ, see Figure 2.2.

In general, reconstruction algorithms can be divided into three different categories: filtered back-projection, Fourier transform (FT) and iterative techniques. Back-projection is the standard technique used for reconstruction. As suggested by the name, the essential idea of back-

projection is to extrude each projection from the angle at which it was collected, Figure 2.1. The reconstructed image using only back-projection is a blurred version of the true object. To correct the blurring problem, the filtered back-projection technique [102,103] can be used. It applies a high-pass filter [104], which is designed to increase the brightness of the center pixel with respect to the surrounding pixels, to sharpen the edge of a feature before the back-projection; however, such a filter also amplifies noise. Depending on the feature(s) of interest, an appropriate kernel of the high-pass filter must be selected to balance the trade-off between low noise and high edge sharpness. For instance, if the features of interest are small and discrete, a sharp ('hard') kernel should be employed to accentuate the fine features but sacrifice the sharpness of the edges.

The FT techniques [105] are based on the central slice theorem [106,107], which equates the FT of the projection from an angle with a slice of the FT of the object along the same projection line. Stacking the FT of each projection in the scan gives the FT of the horizontal cross-section from the original object, which can be inverse Fourier transformed into the real space image as shown in Figure 2.2. Note that the 1-D FTs from different projection angles are stacked in a polar coordinate; however, by only using the 2D FT in the polar coordinate to reconstruct the real image is infeasible, because it leads to oversampling near the rotation axis, Figure 2.2. Thus, the main challenge with the FT technique is to accurately map the signal from the polar coordinate to the Cartesian coordinate in the frequency domain. Traditionally, algorithms [55] use an interpolation scheme to perform the mapping task; by contrast, the fast filtered back transform algorithm employs a technique named "gridding" [105], which assigns a weight factor to each element based on the nonuniformity of the polar grid, to improve the mapping accuracy.

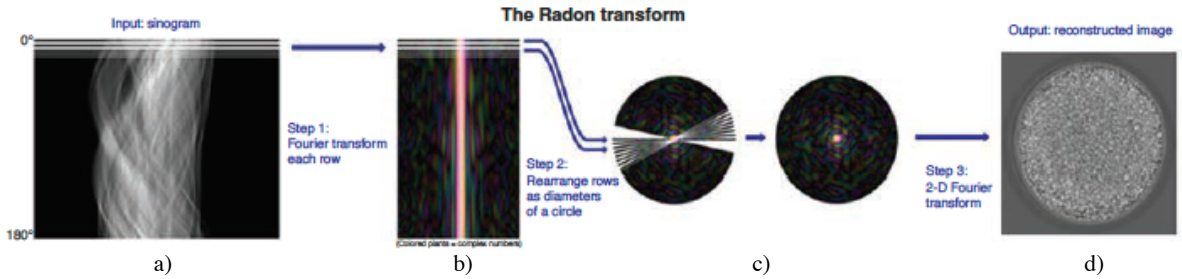

Figure 2.2 A general pipeline of the Fourier-transform-based reconstruction technique includes (a) stacking 1-D projections from a cross-section of a three dimensional object based on the projection angle to generate a sinogram, (b) performing Fourier transform on a sinogram, (c) reorienting the 1-D Fourier transform sinogram in a polar coordinate and mapping the signal from a polar to a Cartesian coordinate (adapted from Wiki by P. Selinger), and (d) performing inverse Fourier transform to reconstruct the cross-section in real space.

The iterative method [108,109] is an actively developing technique which is designed to reduce noise in the reconstruction via a sequence of improving approximations. It normally starts with comparing the reprojections of a filtered back-projected reconstruction to the actual projections, then performing filtered back-projection on the difference and adding to the original reconstruction to minimize error. Such a process iterates until a certain convergence criterion is satisfied. The iterative algorithm commonly outperforms the standard reconstruction method, but it is computationally intensive and requires longer reconstruction time.

Visualizing the μXCT reconstructed object/feature in 3-D is a computationally demanding process, requiring the algorithm to stack real space images to recover the volumetric dataset. Once the stack of 2-D images has been reconstructed, visualization can be accomplished with packages such as ImageJ, Dragonfly, Volume Graphics' VGSTUDIO MAX, and Thermo Fisher Scientific's Avizo, which have toolkits for segmentation and size and shape analysis. The major difficulty of segmentation is being able to separate powder particles from each other and

the intermediate gap from the powder porosity, especially when the powder size approaches the μXCT resolution. The watershed algorithm [110] is commonly used in image segmentation. The idea of watershed is to treat each object, in this case, powder particle, as a basin and each pixel value as topological information. By flooding the basins, the water will eventually meet at a boundary that is used to separate the objects. The accuracy of the segmentation of powder porosity may potentially be improved by postprocessing, for example, filtering interparticle vacancies from powder porosity by using shape descriptors.

μXCT was performed at the 2-BM beamline of the Advanced Photon Source (APS) at Argonne National Lab (ANL). Depending on the x-ray absorptivity of the sample, a monochromatic or a pink beam was chosen to illuminate the specimen. At the 5x objective, which is the magnification used to collect all the data in this study, the μXCT setup offers a 1.55 (L) x 1.55 (W) x 1.41 (H) mm^3 imaging volume, and 0.69 μm/pixel spatial resolution. Powder samples were packed in Kapton tubes with 1 mm inner diameter. As-built specimens of approximately 1 x 1 mm^2 square cross-section were removed from the as-built AM parts using a wire EDM. During 180° of sample rotation, the detector collected 1,500 sinograms at 0.12° angular step. These sinograms were then fed into TomoPy 0.0.3 [111] to perform reconstruction followed by segmentation, analysis, and visualization in FEI Avizo 9.1.1. 3D watershed algorithm was used to separate powder particles to perform size analysis.

2.2.2. Shape Analysis

Powder and porosity can be quantified by using the aforementioned packages if they are properly segmented. Due to the similar characteristics of powder and porosity, the same set of shape descriptors, e.g., anisotropy, elongation, and flatness, and size distributions, e.g.,

equivalent spherical diameter and Feret diameter, used to measure powder particles should also be applied to porosity quantification.

A reasonable metric to quantify the pore morphology is anisotropy, which describes the deviation from a spherical shape. The anisotropy calculation starts with finding the first order moments, i.e., centroid, of the object

$$M_{1x} = \frac{1}{V(X)} \sum_{X} x_i$$

where M_{1x} is the first order moment in x axis and $V(X)$ is the volume of the object involving points (x_i, y_j, z_k). The diagonal, e.g., M_{2xx}, and off-diagonal, e.g., M_{2xy}, second order moments are defined as

$$M_{2xx} = \frac{1}{V(X)} \sum_{X} (x_i - M_{1x})^2$$

$$M_{2xy} = \frac{1}{V(X)} \sum_{X} (x_i - M_{1x})(y_j - M_{1y})$$

Repeating the same calculation for y and z direction derives the coordinates of the centroid and results in the matrix of second order moments, i.e., variance-covariance matrix, of a 3D object

$$\boldsymbol{M} = \begin{bmatrix} M_{2xx} & M_{2xy} & M_{2xz} \\ M_{2xy} & M_{2yy} & M_{2yz} \\ M_{2xz} & M_{2yz} & M_{2zz} \end{bmatrix}$$

where the anisotropy is estimated based on its minimum, I_1, and maximum, I_2, eigenvalues.

$$Anisotropy = 1 - \frac{I_1}{I_2}$$

2.2.3. Dynamic X-Ray Radiography

DXR was performed at the 32-ID-B beamline of the APS at ANL. Zhao *et al.* [58] have demonstrated the setup for *in-situ* monitoring of the miniature L-PBF process which consists of

a ytterbium fiber laser (IPG YLR-500-AC, IPG Photonics, Oxford, USA, wavelength of 1070 nm, maximum output power of 540 W) placed directly above the sample, a thin-slab sample (300 – 500 µm thickness x 2.89 mm height) sandwiched by two glassy carbon plates (1 mm thickness x 3 mm height), and a powder layer (approx. 200 µm height) placed on top of the base plate, see Figure 2.3. Note that the thickness refers to the dimension along the direction of the x-ray beam and the height refers to the dimension along the direction of laser penetration.

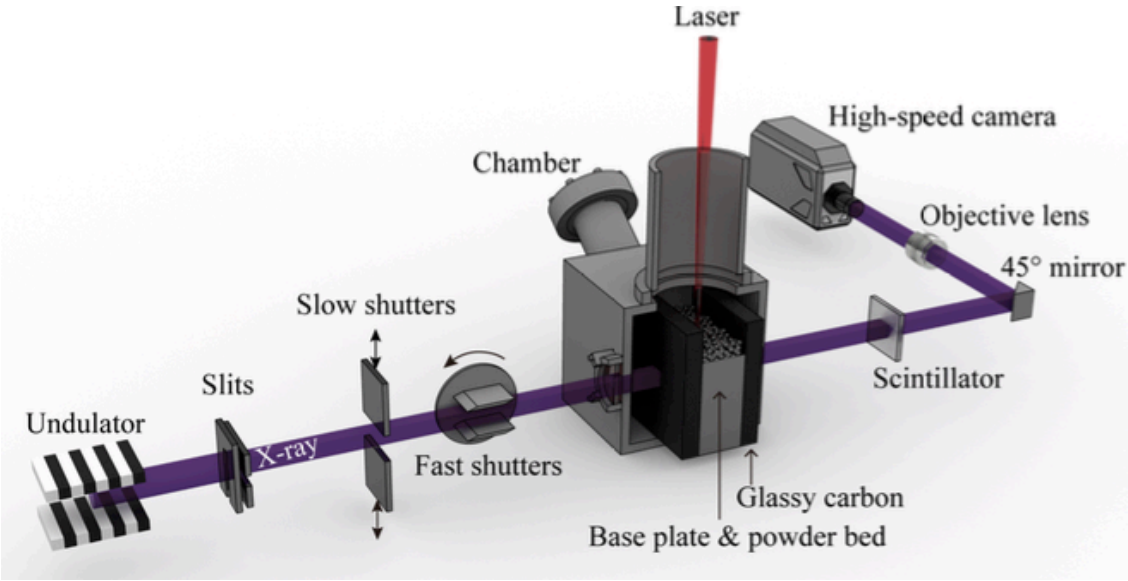

Figure 2.3 Schematic of the DXR setup for L-PBF experiments at 32-ID of the APS.

All the laser melting experiments were conducted inside an argon (1 atm) filled chamber to replicate the building condition of a powder-added single-bead experiment in a L-PBF machine. In the path of the x-ray beam, the miniature powder bed sample was positioned in the upstream and a high-speed imaging camera was placed 310 mm away from the sample in the downstream, see Figure 2.3. This study used a laser spot size of 67.8 µm, a frame rate of 50,000 frames per second, and polychromatic x-rays with the first harmonic energy of 24.4 keV and wavelength at 0.508 Å. DXR videos were processed frame by frame in ImageJ to optimize the

brightness and enhance the contrast to further distinguish the regions of interest, e.g., melt pool, vapor cavity, and pores, etc.

3. Printability of HDH Ti-6Al-4V Powder in EBAM & L-PBF

This chapter was adapted from two publications – 1) S.P. Narra and Z. Wu *et al*., Use of Non-Spherical Hydride-Dehydride (HDH) Powder in Powder Bed Fusion Additive Manufacturing published in Additive Manufacturing (2020), and 2) Z. Wu *et al*., Study of Printability and Porosity Formation in Laser Powder Bed Fusion Built Hydride-Dehydride (HDH) Ti-6Al-4V published in Additive Manufacturing (2021).

3.1. Introduction

There is a growing interest in using recycled materials and economically produced powder in AM processes. State-of-the-art PBF AM processes typically use spherical powders that are produced using atomization techniques since spherical powder is often considered better in flowability and packing. However, using irregularly shaped Ti-6Al-4V powder from the HDH process is more cost efficient because fewer processing steps are required, and it can use recycled materials as feedstock. This motivates the need for a design guideline and process window for the HDH powder, as well as an approach that can be applied to optimizing AM processes for other non-spherical powders. The current chapter investigates the powder spread, flow and packing characteristics and discusses the development of deposition parameters for using the HDH powder in an EBAM process and a L-PBF process. The results demonstrated that HDH powder can be used to fabricate nearly fully dense as-built parts in the two most popular AM systems with minor/no hardware modification using the optimized parameters.

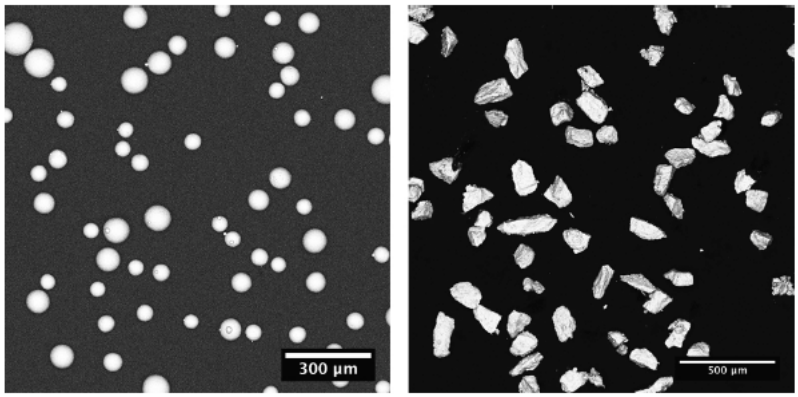

Figure 3.1 SEM micrographs of the standard EOS (left) and HDH Ti-6Al-4V (right) powder.

3.2. Hypothesis

Hypothesis 3.1. The EBAM parts in the HDH Ti-6Al-4V powder can be fabricated to reach > 99.9 % density by using optimal process parameters despite the irregular morphology and large powder size.

Hypothesis 3.2. The L-PBF parts in the HDH Ti-6Al-4V powder can be fabricated to reach > 99.9 % density by using optimal process parameters despite the irregular morphology and large powder size.

3.3. Methods

3.3.1. Fabrication in EBAM

All the EBAM samples used in this study were fabricated at Carnegie Mellon University using an Arcam S12 machine. The S12 machine equips with an electron beam that can operate at a maximum travel speed > 1000 m/s and power of 3500 W. Prior to deposition, the chamber developed a controlled vacuum (< 2×10^{-3} mbar) with low partial pressure of helium and the electron beam pre-heated the 210 × 210 mm^2 build plate in 304 stainless steel to 730 °C by raster scanning. After each spreading, the beam pre-sintered the powder layer using low energy input to consolidate the loose powder. As discussed in section §1.1.2., all the aforementioned steps aim to

increase the electrical conductivity of the powder bed and the environment to prevent the accumulation of electrostatic charges, thus, minimizing the issue of *smoke*.

This study varied three primary process parameters, speed function (SF), focus offset (FO), and hatch spacing (HS) to achieve the minimal defect concentration in the as-built HDH parts. Unlike other AM processes, neither the travel speed nor the beam power was disclosed by Arcam, and this made the parameter optimization process challenging. Mahale [112] and Narra *et al*. [91] have demonstrated that SF varied both beam power and travel speed to maintain the energy density and the resulting melt pool size according to the process conditions on the fly. Note that a smaller SF value corresponds to a higher energy density, i.e., larger melt pool. FO controls the defocusing of the beam, also known as the spot size. Francis [36] calibrated the beam diameter with respect to the FO value and reported that the spot size increased with the increasing FO value. HS defines the distance between the centerlines of two neighboring melt tracks.

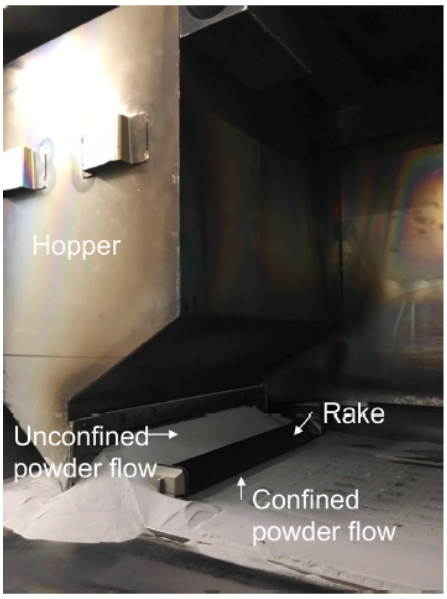

Figure 3.2 Interior of the Arcam S12 build chamber showing the HDH powder pile ready for spreading.

All the Arcam builds in this study used the standard slice layer thickness of 70 µm. Note that the slice layer thickness is different from the powder layer thickness. For instance, assuming the powder has a packing fraction of 0.5, a slice layer thickness of 70 µm results in a convergence to a 140 µm powder layer thickness (approximately twice as thick) after a few initial layers. Thus, the gap between the build plate and the rake was sufficient for depositing the larger HDH powder particles without causing powder bed streaking. As will be discussed in section §3.4.1., the HDH powder showed comparable flowability as the gas atomized Ti-6Al-4V powder. Thus, only minor hardware modification, to enlarge the opening of the hopper as shown in Figure 3.2, was needed. Before the modification, the size of the powder pile accumulated in front of the hopper was too small to be properly spread onto the build plate area.

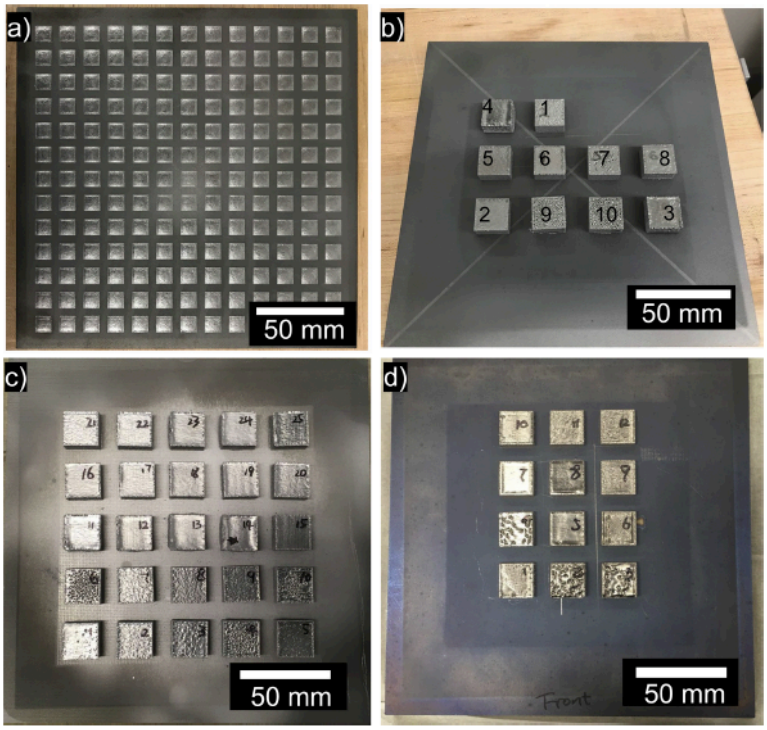

Figure 3.3 Four Ti-6Al-4V builds on the build plate to illustrate the layout in the a) porosity benchmarking build using the HDH powder, b) & c) parameter optimization build 1 & 2 using the HDH powder, and d) build using the standard atomized powder.

Figure 3.3 summarizes the four Ti-6Al-4V builds fabricated in this study including a porosity benchmarking study using the HDH powder, two parameter optimization builds using the HDH powder, and a build using the standard atomized powder as comparison.

The single-bead melt pool study fabricated 64 rectangular contours. A total of 56 different combinations of SF and FO shown in Table 3.1 were used to map the melt pool geometry as a function of process parameters. For each FO value in Table 3.1, the SF was varied between 06 and 42. Eight extra specimens were designed to investigate the spatial variation across the build plate. To reproduce the melt pool geometry in an actual build of solid specimens, a 140 µm thick powder layer (50 % shrinkage assumed) was deposited before preheating.

Table 3.1 Speed function and focus offset levels used in the single-bead experiments

Speed function	06, 12, 18, 24, 30, 36, 42
Focus offset (mA)	10, 19, 25, 30, 35, 40, 50, 60

Figure 3.3a shows the array of 13 x 13 blocks with dimensions of 10 mm (L) x 10 mm (W) x 10 mm (H) fabricated to benchmark the porosity concentration of the HDH parts built using the nominal parameter set (SF36FO19HS200). This build aimed to study the spreadability of the HDH powder in an Arcam powder spreading setup meanwhile to investigate the spatial variation of porosity concentration at a constant deposition condition. At the time of performing these tests, there was no equipment on the Arcam S12 to monitor the spreading of each layer and to capture images at the resolution of the powder size. The 169 blocks were evenly distributed on the start plate with 5 mm spacing between the adjacent specimens.

Prior work of Cunningham *et al*. [51] reported a reduction in powder entrapped gas induced porosity when the HS was decreased in a L-PBF process. One plausible explanation for this observation is that a pore is more likely to escape from the melt pool if it is surrounded by

liquid metal for a longer period. Albeit the different sources of porosity formation in the HDH builds, this approach should promote the escape of any pores from the melt pool and backfilling by the liquid metal. The parameter selection for the experiments using the HDH powder followed this essential idea. Thus, the process parameters (SF, FO, and HS) were varied systematically to i) increase the melt pool area, ii) increase the overlap between the adjacent melt tracks by decreasing the hatch spacing, and iii) increase the spot size to minimize the possibility for keyhole porosity/balling especially for cases with increased melt pool area. Table 3.2 summarizes the 9 parameter sets tested in the first optimization build. The second optimization build evaluated more parameter sets, see Table 3.3, by applying a wider grid to the parameter space. The reason of selecting each parameter set is given in the tables.

Table 3.2 Speed function, focus offset, and hatch spacing used in the first parameter optimization build.

Sample number	SF	FO (mA)	HS (μm)	Description
1	36	19	200	Nominal melt pool area
2	36	19	100	Nominal melt pool area with decreased HS
3	24	30	200	Remelting with ~1.5 x nominal melt pool area + increased FO, nominal HS
4	24	30	100	Remelting with ~1.5 x nominal melt pool area + increased FO, decreased HS
5	24	19	200	~1.5 x Nominal melt pool area + nominal HS
6	24	19	100	~1.5 x Nominal melt pool area + decreased HS
7	24	30	200	~1.5 x Nominal melt pool area + increased FO with nominal HS
8	24	30	100	~1.5 x Nominal melt pool area + increased FO with decreased HS
9	24	40	200	~1.5 x Nominal melt pool area + increased FO with nominal HS
10	24	40	100	~1.5 x Nominal melt pool area + increased FO with decreased HS

Table 3.3 Speed function, focus offset, and hatch spacing used in the second parameter optimization build.

Sample number	SF	FO (mA)	HS (µm)	Description
1	12	40	200	A nominal HS of 200 µm was used. Process combinations were chosen based on the melt pool geometry data from the single-bead experiments. Process parameter combinations resulting in balling and lack-of-fusion are excluded.
2	18	30		
3	18	35		
4	18	40		
5	24	25		
7	24	30		
6	24	35		
8	30	19		
9	30	25		
10	30	30		
11	12	40	100	A reduced HS was used to study the effect of increased remelting on the resulting part porosity.
12	18	30		
23	18	35		
25	18	40		
15	24	25		
17	24	30		
16	24	35		
18	30	19		
19	30	25		
20	30	30		
21	24	30	200	Repeatability test for the expected optimal parameter combination.
22	24	30	100	
13	24	30	60	HS was further reduced although these parameters result in lower deposition rates.
24	24	30		
14	30	25		

To compare the porosity in the parts made using the HDH powder and the atomized powder, 20 mm (L) × 20 mm (W) × 10 mm (H) samples were fabricated with the process parameters listed in Table 3.4. The selection of parameters followed the results of the HDH builds and the logic of choosing each parameter set were given in the table. This build stopped at a height of 3.5 mm because of beam column overheating. However, these samples were still

useful for cross-sectioning porosity characterization. Figure 3.3d shows the layout of the as-fabricated samples on the build plate.

Table 3.4 Speed function, focus offset, and hatch spacing used in the build using the atomized powder.

Sample number	SF	FO (mA)	HS (μm)	Description
1	36	19	200	Nominal parameters
2	24	30	200	Optimal parameters from the first HDH optimization build
3	18	30	200	Parameters within the process window of the HDH powder
4	18	40	200	
5	12	40	200	
6	36	19	100	Nominal parameters with reduced HS
7	24	30	100	Optimal parameters from the first HDH optimization build
8	12	40	100	Parameters within the process window of the HDH powder with reduced HS
9	36	19	200	Repeatability study for samples 1 and 2
10	24	30	200	
11	18	19	200	Optimal parameters for the conventional powder
12	18	19	200	

A brittle intermetallic layer formed between the Ti-6Al-4V specimens and the build plate since the plate was 304 stainless steel in the Arcam S12. Thus, sample removal from the build plate was simply completed by hand. The post-processing steps of the as-built specimens include depowdering with pressurized air (80 psi) in the Arcam Powder Recovery System and sectioning using a GF Machining Solutions AC Progress VP3 EDM to reveal the vertical cross-sections.

3.3.2. Fabrication in L-PBF

In this study, two HDH builds were fabricated at Carnegie Mellon University using an EOS M290 L-PBF machine as shown in Figure 3.4. They used room temperature preheat, layer

thickness of 60 µm, Ti-6Al-4V build plate, and argon atmosphere. All as-built specimens were sectioned off from the build plate using a GF Machining Solutions AC Progress VP3 EDM.

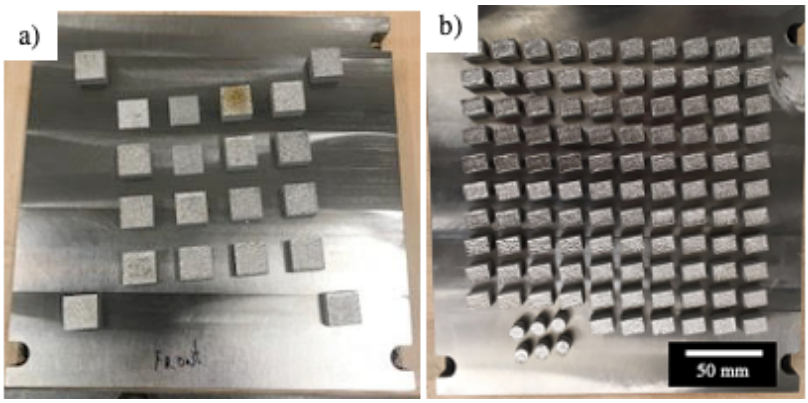

Figure 3.4 Layouts of a) the first build and b) the optimization build using the HDH Ti-6Al-4V powder on an EOS M290 build plate

The first build (Figure 3.4a) was a proof of concept which intended to show that the HDH powder can be properly spread and fused in a L-PBF process. It contained 20 rectangular prisms with dimensions of 20 (L) x 20 (W) x 10 (H) mm^3 where the laser power and laser scan velocity were systematically varied as shown in Table 3.5. Note that the parameter selection started with a commonly used nominal parameter set for Ti-6Al-4V at 60 µm layer thickness which has 280 W laser power, 1200 mm/s laser velocity and 0.14 mm hatch spacing.

Table 3.5 Process parameters used in the first HDH build in an EOS M290 L-PBF process. Note that the nominal parameters are in ***bold****.*

Sample #	Scan speed (mm/s)	Power (W)	Hatch spacing (mm)
1	400	75	0.14
2	800	75	0.14
3	1200	75	0.14
4	400	150	0.14
5	800	150	0.14
6	1200	150	0.14
7	400	225	0.14

8	800	225	0.14
9	1200	225	0.14
10	400	280	0.14
11	800	280	0.14
12	1200	280	0.14
13	400	350	0.14
14	800	350	0.14
15	1200	350	0.14
16	1200	280	0.12
17	1200	280	0.1
20	1200	280	0.08
18	**1200**	**280**	**0.14**
19	**1200**	**280**	**0.14**

Based on the insight learned from the first build, the later build was intended to test the repeatability of the porosity contents and develop the complete process window for the HDH powder. Table 3.6 summarizes the 53 selected power and velocity combinations at three different hatch spacings. Two rectangular prisms with dimensions of 10 (L) x 15 (W) x 10 (H) mm^3 were built at each parameter set resulting in a total of 103 specimens.

Table 3.6 Laser process parameters used in the HDH optimization build

Sample #	Scan speed (mm/s)	Power (W)	Hatch spacing (mm)	Energy density (J/mm^3)	Sample #	Scan speed (mm/s)	Power (W)	Hatch spacing (mm)	Energy density (J/mm^3)
1	400	150	0.12	52.08	28	800	150	0.09	34.72
2	400	225	0.12	78.13	29	800	225	0.09	52.08
3	400	280	0.12	97.22	30	800	280	0.09	64.81
4	400	340	0.12	118.06	31	800	340	0.09	78.70
5	400	370	0.12	128.47	32	800	370	0.09	85.65
6	600	150	0.12	34.72	33	1250	225	0.09	33.33
7	600	225	0.12	52.08	34	1250	280	0.09	41.48
8	600	280	0.12	64.81	35	1250	340	0.09	50.37
9	600	340	0.12	78.70	36	1250	370	0.09	54.81
10	600	370	0.12	85.65	37	1500	225	0.09	27.78
11	800	150	0.12	26.04	38	1500	280	0.09	34.57
12	800	225	0.12	39.06	39	1500	340	0.09	41.98

13	800	280	0.12	48.61	40	1500	370	0.09	45.68
14	800	340	0.12	59.03	41	800	150	0.15	20.83
15	800	370	0.12	64.24	42	800	225	0.15	31.25
16	1000	225	0.12	31.25	43	800	280	0.15	38.89
17	1000	280	0.12	38.89	44	800	340	0.15	47.22
18	1000	340	0.12	47.22	45	800	370	0.15	51.39
19	1000	370	0.12	51.39	46	1250	225	0.15	20.00
20	1250	225	0.12	25.00	47	1250	280	0.15	24.89
21	1250	280	0.12	31.11	48	1250	340	0.15	30.22
22	1250	340	0.12	37.78	49	1250	370	0.15	32.89
23	1250	370	0.12	41.11	50	1500	225	0.15	16.67
24	1500	225	0.12	20.83	51	1500	280	0.15	20.74
25	1500	280	0.12	25.93	52	1500	340	0.15	25.19
26	1500	340	0.12	31.48	53	1500	370	0.15	27.41
27	1500	370	0.12	34.26					

3.3.3. Characterization

Powder characterization in this work mainly focused on powder flow, spreadability, shape, and size analysis. More than 1,000 powder particles were imaged using a FEI Aspex Express SEM to ensure adequate powder statistics. To capture the non-spherical nature of the HDH powder, Feret diameter was measured in addition to equivalent spherical diameter (ESD).

For powder flow, the standard atomized Arcam powder and the HDH Ti-6Al-4V powder were tested in a Freeman FT4 rheometer. The powder flow energy E can be represented as

$$E = F \times d$$

where the resistance F is a combination of torque and force encountered by the blade and d is the blade travel distance. Resistance F is an energy gradient or force (mJ/mm) term indicating the energy consumption for each millimeter of travel distance. The dynamic testing mode was used to characterize both the specific energy (SE) and the basic flowability energy (BSE) which were measured when the rotating test blade was traveling upward (unconfined flow) and traveling

downward (confined flow), respectively. As shown in Figure 3.5, the unconfined flow could approximate the stress zone encountered by the powder flowing out from the hopper; the confined flow could approximate the stress zone between the rake/recoater blade and the start plate. The dynamic test mode used a total of 22 cycles, including 11 conditioning cycles and 11 test cycles, which are designed to assess the robustness of the flowability measurements with the stability index (SI). The SI, SE, and BSE are estimated as follows

$$SI = \frac{E_{d\#7}}{E_{d\#1}}$$

$$SE = \frac{E_{u\#6} + E_{u\#7}}{2m}$$

$$BFE = E_{d\#7}$$

where $E_{u\#}$ and $E_{d\#}$ are the energy consumptions as the blade is traveling upward and downward at a particular testing cycle and m is the mass of the powder sample.

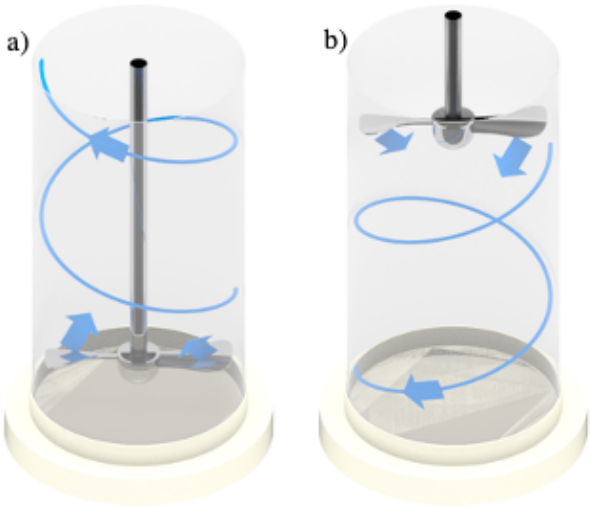

Figure 3.5 Schematics showing that a Freeman FT4 rheometer is measuring a) the specific energy at an unconfined powder flow condition and b) the basic flowability energy at a confined powder flow condition.

A Leica DM750M optical microscope was used to analyze the porosity at the cross-sections of the as-built HDH Ti-6Al-4V specimens. The top and bottom regions of the block were imaged to capture any location-specific variation within a given sample. Figure 3.12 shows examples of micrographs used for porosity analysis. Optical images were analyzed using ImageJ where the pores were segmented from the solid material and quantified by ESD, Feret diameter and porosity percentage. For some specimens fabricated in the optimization build in the L-PBF process, the porosity content was quantified using both the cross-sectioning approach and the Archimedes' principle as per ASTM B962 [113].

3.4. Results & Discussions

3.4.1. HDH Powder Characteristics

The analysis of the powder size and the powder morphology is important for understanding the flowability of the HDH powder and selecting the process conditions for AM fabrication. Figure 3.6 shows the size distributions of 1390 HDH powder particles and 1022 AP&C atomized powder particles. Most of the HDH powder particles are in the size range of 75 – 175 μm in ESD. The size spectrum revealed two distinct clusters of particles, namely the ultra-fine particles (< 20 μm), which composed less than 25 % of the count, and the coarse particles (> 65 μm), which composed more than 50 % of the count. As a comparison, the standard AP&C powder particles are between 40 μm and 120 μm with a size distribution skews positively. The rightward shift of the powder size distributions measured in Feret diameter, which is defined as the longest distance between two points on the circumference, from the one measured in ESD implies the non-spherical nature of the HDH powder, which is also evident in Figure 3.1. By contrast, the better matched size distributions in Feret diameter and ESD of the AP&C powder imply that it has higher sphericity. The ultra-fine particles (< 20 μm) appeared in both powders

might be a result of the detachment of the satellite particles or particle fracture during powder handling which were not removed during the sieving operation. As summarized in Table 3.7, the HDH powders are 1.3 - 1.7 times larger in average size (ESD with a cutoff at 40 μm) compared with the standard Arcam AP&C powder. On the other hand, the major part of the HDH powder (median size D_{50} = 101 μm) is about 2.5 times coarser in average size than the standard EOS Ti-6Al-4V powder (D_{50} = 39 μm) [114] which suggested that a recalibration of the existing process parameters, especially the layer thickness, was needed in order to use the HDH powder in the L-PBF system. In terms of the extreme situation, the HDH powder particle reached 349 μm in dimension while the maximum size of the spherical powder was only 198 μm. Sieving did not eliminate all the large, irregularly shaped particles since an elongated particle can easily pass through a finer sieve. These particles raised a concern at the fabrication because they could affect the powder bed quality by leading to powder bed streaking which in turn impairs the as-built parts. Hence, it is important to take non-sphericity of the HDH powder into consideration when interpreting the flowability, spreadability and printability.

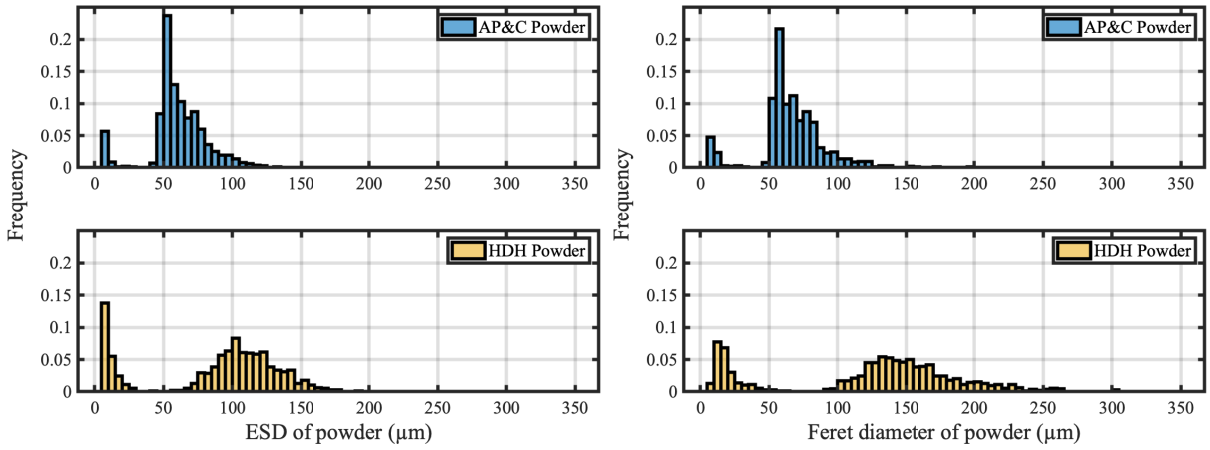

Figure 3.6 Distributions in ESD and Feret diameter of the HDH and AP&C atomized powders.

Table 3.7 Powder size statistics of the HDH and the standard AP&C atomized powders.

	HDH Coarse	AP&C atomized
Avg. ESD (μm)	88 ± 47	60 ± 21
Avg. ESD* (μm)	112 ± 23	65 ± 15
Avg. Feret diameter (μm)	125 ± 68	66 ± 24
Avg. Feret diameter* (μm)	157 ± 38	71 ± 18
Median ESD (μm)	101	58
Median ESD* (μm)	110	60
Median Feret diameter (μm)	138	64
Median Feret diameter* (μm)	150	66
Max. Feret diameter (μm)	349	198

*A minimum cutoff at 40 μm was applied

Flowability of the HDH powder can be significantly different from that of the standard atomized powder as the HDH powder has non-spherical morphology. Any variation in the powder size and morphology can affect the powder flow through the hopper opening and the powder deposition within the build area. Figure 3.7 shows the rheometry measurements of the HDH powder at its used and virgin conditions and the virgin standard atomized powder as a direct comparison. The test results were robust since the stability indices were ~1. The virgin and used condition refer to measurements taken after receiving the powder and after the first post-build sieving process. The used HDH powder flowed slightly easier at the free flow condition compared with the virgin powder and the difference between the flowabilities of the virgin and the used HDH powder is statistically insignificant at the confined flow condition. It can be concluded that the powder storage and recycling process had little impact on the powder flowability. In fact, the HDH powder showed better flowability in the confined flow condition, i.e., lower BFE, compared with that of the atomized powder. The low SE (< 5 mJ/g) is indicative of the free-flowing behavior for both powders, and the atomized powder flowed slightly better than the virgin but not as well as the used HDH powder in the free flow condition. Typically, coarser size promotes flowability since the lower packing reduces the total contact area between particles; but lack of sphericity usually impairs flowability due to surface friction and particle

interlocking [115,116]. In other words, the counteracting effect of the two powder characteristics might result in the comparable flowabilities of the HDH powder and the standard powder.

Although the standard powder and the HDH powder showed very comparable flow properties, the openings of both hoppers in the Arcam S12 were enlarged to allow the free-flowing powder to reach the fetch position of the rake. It is important to note that the measurements from a rheometer are indications of but not equivalent to the actual spreadability of powder in a fabrication setting; instead, the measurement is a good sanity check prior to fabrication.

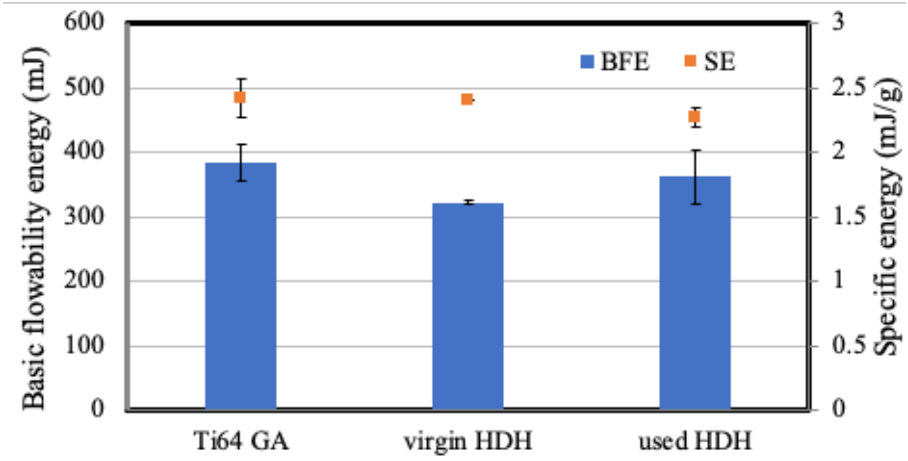

Figure 3.7 Rheometry measurements of the HDH powder and gas atomized powder in the confined flow and free flow conditions.

The HDH Ti-6Al-4V powder was supplied by Reading Alloys (previously affiliated with AMETEK Inc., now a part of Kymera International). This material conforms to ASTM specification number B348 Rev. 08a Grade 5 for chemistry requirements. Table 3.8 shows the elemental analysis results of the powder used in this study.

Table 3.8 Elemental analysis results of the HDH Ti-6Al-4V powder

Element	RAI analysis (wt%)	ASTM spec (wt%)	Method of analysis
Al	6.08	5.5 – 6.75	Inductively Coupled Plasma
V	3.88	3.5 – 4.5	Inductively Coupled Plasma
Fe	0.19	0.40 Max	Inductively Coupled Plasma
C	0.023	0.08 Max	Combustion
H	0.005	0.015 Max	Fusion
N	0.023	0.05 Max	Fusion
O	0.17	0.20 Max	Fusion

3.4.2. Printability in EBAM

As mentioned before, the actual beam travel speed and beam power used by Arcam S12 was unknown, meaning that using modeling or analytical techniques to estimate the melt pool dimensions across the process space was not feasible. The objective of the single-bead scan study was to develop the relationship between the melt pool geometry and the process parameters. Analyzing the melt pool cross-section could identify both the abnormal and the optimal melt pool geometries which provide important insights about the origins of the porosity formation and a valuable guideline for the parameter optimization. Given a large spot size in the EBAM process (on the order of 150 μm), keyhole porosity is rarely observed. Francis [36] did show that keyhole melt pools can be generated in single-bead experiment where the beam power, beam velocity, and focus offset were explicitly specified. However, the beam power and velocity were automatically controlled by the software to avoid excessive energy input based on the given max beam current and speed function index in an actual fabrication setting in an Arcam S12 machine. Therefore, the melt pools were categorized into three types based on their geometry as shown in Figure 3.8 – (i) balling (SF06FO10 & SF24FO19), (ii) wide & deep (SF24FO30), and (iii) narrow & shallow (SF24FO40). In the melt pool (SF24FO19) that exhibits the balling phenomenon, a significant amount of material was transferred above the current layer which created an uneven top surface. The mechanism of balling phenomenon is currently controversial.

Theories attempted to attribute balling to the poor wettability between the solid and liquid, the fluid flow, and the Marangoni convection. Plateau Rayleigh instability [117] coupled with the viscosity, size, and shape of the melt track has been used to explain balling from the surface tension perspective. Balling normally happens at high power and high velocity. Gu *et al*. [118] found that the large balls split to large amount of micrometer-sized balls as the beam power was further increased (> 350 W) in the L-PBF process. With the same energy input (SF), increasing the spot size lowered the energy density within the beam spot which led to a wider melt pool and a more stable top surface, e.g., SF24FO30. Further defocusing led to decreased melt pool width and depth, e.g., SF24FO40.

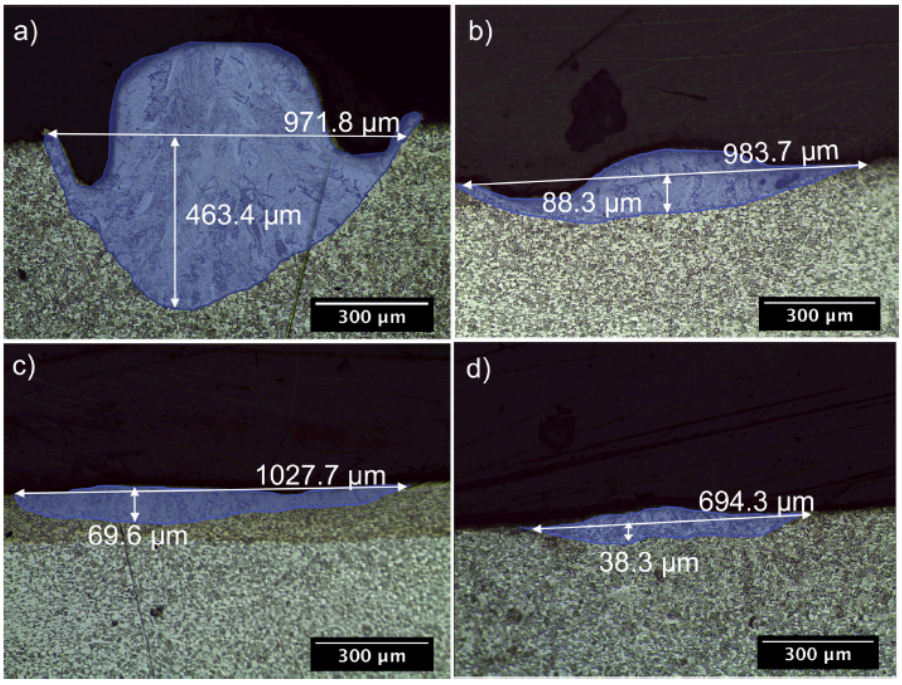

Figure 3.8 Optical micrographs of the melt pool cross-sections from the melt tracks deposited with a) SF 06 & FO 10, b) SF 24 & FO 19, c) SF 24 & FO 30 and d) SF 24 & FO 40, demonstrating widely varying melt pool morphologies.

The melt pool geometry was quantified in three dimensions – depth, width, and height. Melt pool depth controls the amount of remelting, width controls the overlapping with the adjacent melt tracks, and height indicates the stability of the top surface of a melt pool. Compared with melt pools in L-PBF processes, EBAM generates melt pools with much larger width-to-depth ratios. As summarized in Figure 3.9, the melt pool dimensions shrank as the energy density decreased and the spot size remained. Note that a higher SF corresponds to a lower energy density and a higher FO corresponds to a larger spot size. A more focused beam with the same energy input penetrated deeper into the bulk material but potentially led to unstable top surface. At high energy densities, larger spot size led to wider melt pool which was favorable for reducing the instability at the top surface and increasing the overlapping between the adjacent melt tracks. However, a beam with low energy input could not penetrate the powder layer if the spot size was too large, which led to no melting as shown in Figure 3.9. The reference plane in Figure 3.9b indicates a 70 µm melt pool depth which is equivalent to the layer thickness. Melt pool depth < 70 µm implies no remelting of the previous layer for the particular parameters which were avoided in the later optimization studies.

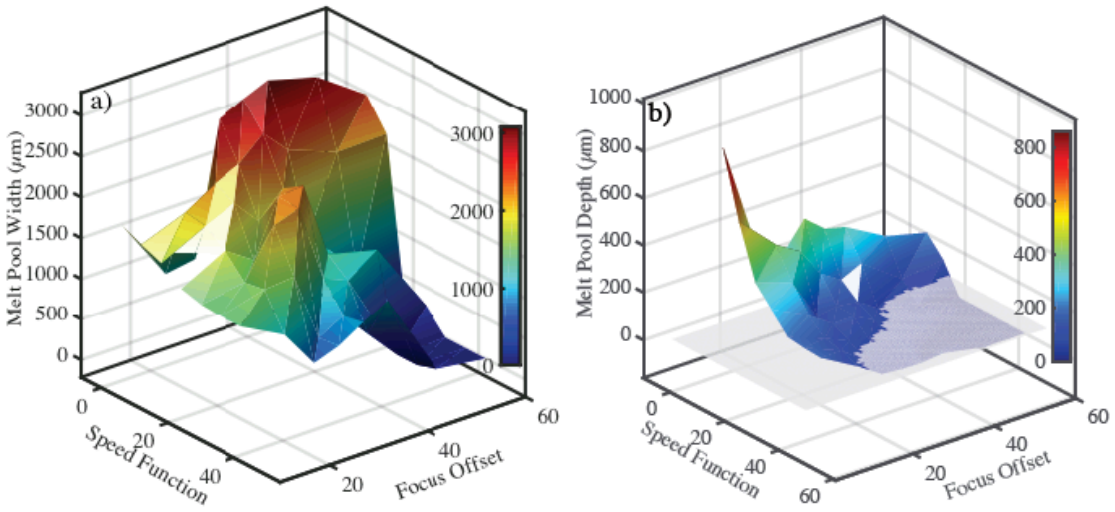

Figure 3.9 Single-bead melt pool a) width and b) depth in the parameter space of speed function and focus offset.

The objective of the benchmarking build, Figure 3.3a, was to inspect the powder spreading across the build plate and to identify the baseline porosity level in the as-built HDH parts fabricated using the nominal parameters available in the Arcam S12 equipment. Figure 3.10 shows the porosity percentage in 17 blocks with their corresponding positions on the build plate. The average porosity varied between 2.50 % and 5.28 % and showed no notable correlation with the build position; nonetheless, it is important to note the variability in porosity for the same process parameters. The percentages match with the results reported by Medina [20], i.e., HDH parts with 97.5 % density fabricated using the Arcam nominal parameters. Further optimization of process parameters was needed to meet the goal of 99.9 % density.

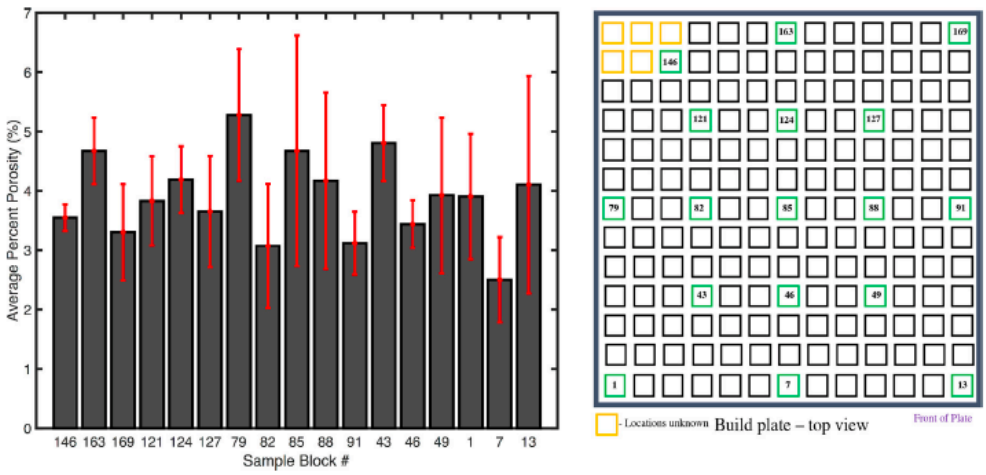

Figure 3.10 Average percent porosity in 17 HDH blocks vary from 2.50 % to 5.28 %. Note that the 17 blocks were spread across the build plate to capture systematic variation of porosity due to difference in location as shown on the schematic of the build plate. Error bars represent the variation of porosity measured from different images.

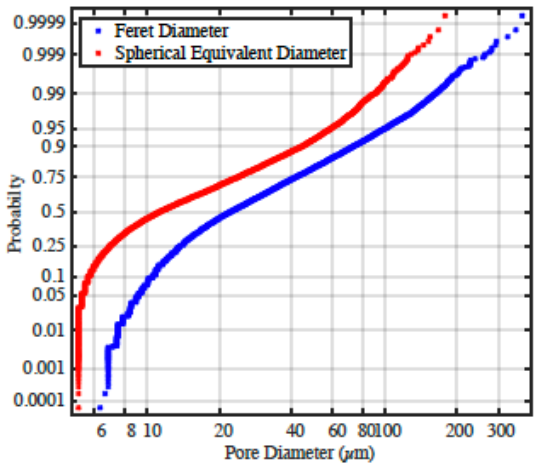

Figure 3.11 Porosity size distribution in the as-built HDH Ti-6Al-4V specimens fabricated using the nominal parameters in the Arcam S12.

Table 3.9 Equivalent spherical diameter and Feret diameter statistics for porosity in the as-built HDH Ti-6Al-4V specimens fabricated using nominal parameters in the Arcam S12.

Measurement metric	Average (μm)	Maximum (μm)
Equivalent spherical diameter	19.0 ± 18.6	178.1
Feret diameter	34.1 ± 32.4	375.4

Table 3.9 summarizes the average and the maximum in ESD and Feret diameter of roughly 9,000 pores analyzed in the porosity benchmarking study. The irregular morphology of the large pores (> 150 μm) shown in Figure 3.12 suggests that the Feret diameter is a better descriptor. As shown in the Figure 3.11, the porosity size distribution in Feret diameter shifted to the larger end with respective to the distribution in ESD. In the EBAM parts built using the standard Ti-6Al-4V powder, the pore size normally ranges from 5 to 160 μm [50]. The irregular morphology of porosity discovered in this study suggests a different origin of the porosity formation besides the conventional mechanisms – powder entrapped gas, lack-of-fusion, and keyhole porosity. Although lack-of-fusion pores are also irregularly shaped and can be rather

large, the deposition conditions used in these tests were chosen to avoid lack-of-fusion porosity. Therefore, these pores were hypothesized as a result of large local packing variations in the HDH powder bed consisting of the irregularly shaped HDH powder as will be demonstrated by using an image-based Monte Carlo packing analysis in the next chapter. This observation also motivated further investigations about this novel porosity formation mechanism caused by the usage of the HDH powder layer in advanced synchrotron-based techniques as will be discussed in Chapter 4.

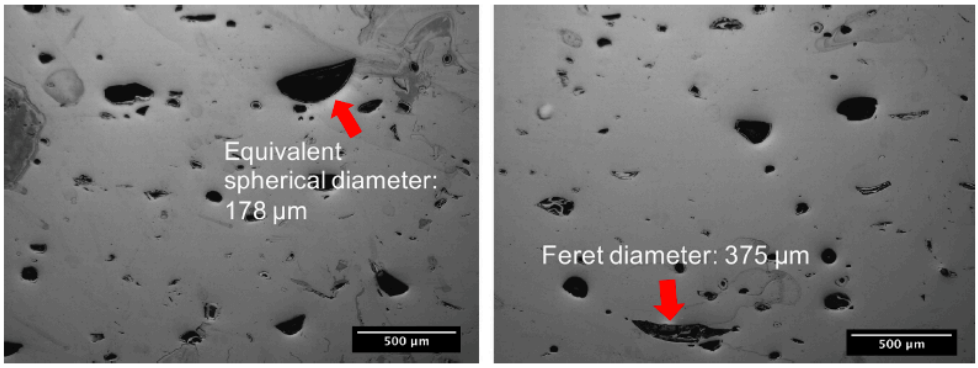

Figure 3.12 Optical micrographs of irregularly shaped porosity in the HDH Ti-6Al-4V specimens fabricated using the nominal parameters in the Arcam S12.

Towards optimization of the process parameters, the goal was to change the melt pool size and use remelting strategy to reduce porosity. The design of experiments (DoE) comprised variations in SF, FO, and HS. Table 3.10 shows the details of the porosity measurements from these samples. Samples #3, #5, and #7 have the same parameters as sample #4, #6, and #8 but with a reduced HS from 200 to 100 µm. The porosity levels were reduced in all three cases with reduced HS implying that increased remelting of the melt tracks is an effective way for porosity mitigation. The porosity in samples fabricated with SF24FO19 (#5 & #6), SF24FO30 (#7 & #8), and SF24FO40 (#3 & #4) decreased and then increased as the spot size was increased through higher FO values. This suggested that defocusing could be effective; however, defocusing and

energy input were related, and the optimal defocusing required a systematic understanding of the effect of SF and FO on the melt pool geometry. Lastly, SF36FO19 (#1 & #2) and SF24FO19 (#5 & #6) resulted in similar porosity contents suggesting that increased energy input alone by just changing SF might not be an effective strategy to reduce porosity. For instance, sample #8 fabricated using SF24FO30 and a reduced HS of 100 µm achieved an optimal density of 99.82 %. This meant a combination of larger melt pool, increased spot size, and reduced HS can result in optimal density. In general, lower porosity levels were observed in samples with remelting. Remelting here refers to remelting the previously deposited layer and also remelting the adjacent melt tracks by decreasing the HS.

Although the average porosity of samples #7, #9, and #10 was > 3 %, most of the cross-sections showed porosity < 0.5 %. The average percent porosity was affected by large pores captured near the top surface as shown in Figure 3.13. Large and interconnected pores were discovered near the top surface in these samples. The origin of these defects was as yet unidentified.

Table 3.10 The resulted porosity and the corresponding process parameters in the first parameter optimization study for the HDH Ti-6Al-4V powder in the Arcam S12 EBAM process.

Sample #	Speed function	Focus offset (mA)	Hatch spacing (µm)	Porosity content
1	36	19	200	2.18 %
2	36	19	100	1.76 %
3	24	30	200	0.57 %
4	24	30	100	0.82 %
5	24	19	200	2.41 %
6	24	19	100	1.57 %
7	24	30	200	3.38 %
8	24	30	100	0.18 %
9	24	40	200	6.05 %
10	24	40	100	4.17 %

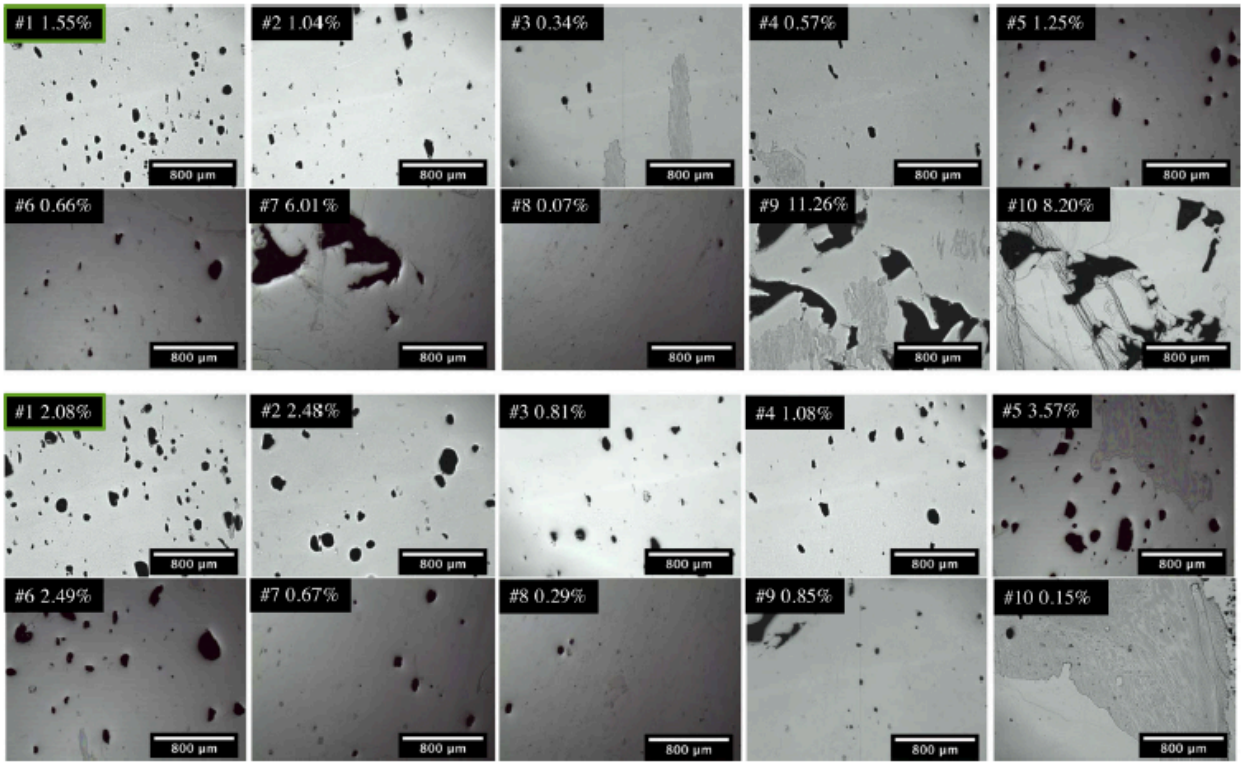

Figure 3.13 Optical micrographs of porosity imaged from the top (top two rows) and the bottom half (bottom two rows) of the cross-sections in the 10 cube HDH Ti-6Al-4V specimens in the first Arcam S12 parameter optimization build. Note that percent porosity of the particular area is shown at the upper left corner.

Following the results obtained from the preliminary study, a second set of optimization experiments was performed. These experiments were based on the powder-added single-bead results for more accurate mapping for the effect of FO. These tests also served the purpose of testing the repeatability of the premise that a systematic increase in melt pool size (smaller values of SF), increase in FO, and decrease in HS can result in dense parts using the HDH powder. Figure 3.14 mapped the porosity measurements in a FO and SF space at three different HS values. Note that the previously reported 0.18 % porosity for SF24FO30HS100 was not repeatable. This could be due to the inherent process variability. Similar variability was also seen

in the benchmarking experiments performed using the nominal parameters. However, the previously observed trend of decreasing porosity with a decrease in SF, an increase in FO, and a decrease in HS appeared to be repeatable. As hatch spacing decreased from the left to the right in Figure 3.14, the porosity content decreased compared with the corresponding samples fabricated with a larger hatch spacing; this implied that decreasing the HS expanded the process window for dense parts to the higher SF and lower FO regions.

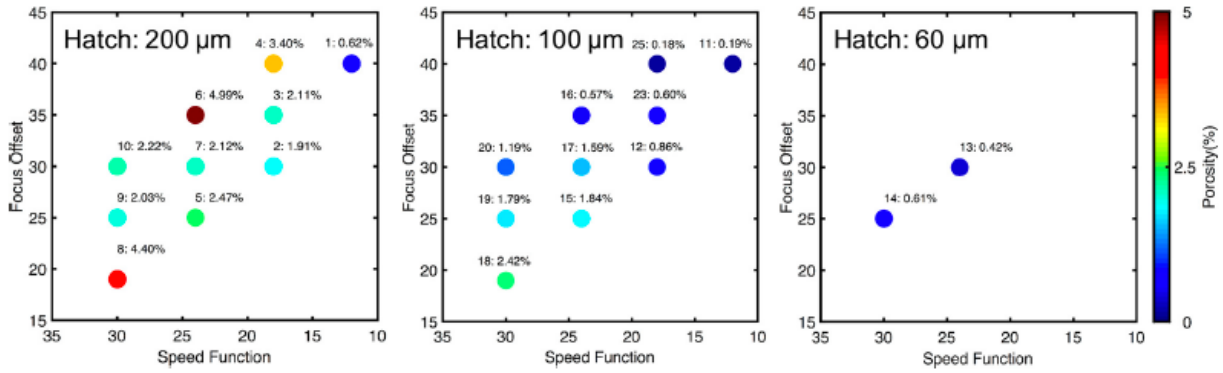

Figure 3.14 Percent porosity as a function of speed function and focus offset for three different hatch spacing values.

Similar to the experiments using the HDH powder, a selected set of SF, FO, and HS were chosen to fabricate solid blocks using the atomized powder. These parameters were chosen based on the HDH experiments and the prior work performed by Cunningham *et al*. [119]. Figure 3.15 maps the porosity measurements in the FO and SF space at two different HS values. The previously observed trend of decreasing porosity with decreased SF, increased FO, and decreased HS were also valid for the atomized powder. Additionally, decreasing the HS expanded the process window for dense parts to the high SF and low FO regions.

This build also demonstrated the presence of variability resulting from various factors such as age of the machine, operator's experience, calibration, parameters used in the adjacent

blocks in the same build, and powder spreading. In this experiment, non-spherical pores were observed in the top regions of the build for samples fabricated using the nominal parameters. This was not reported before in parts fabricated with the nominal parameters. In addition, the percent porosity of the samples built with the nominal parameters varied between 0.28 % and 1.82 %, which further demonstrated the process variability.

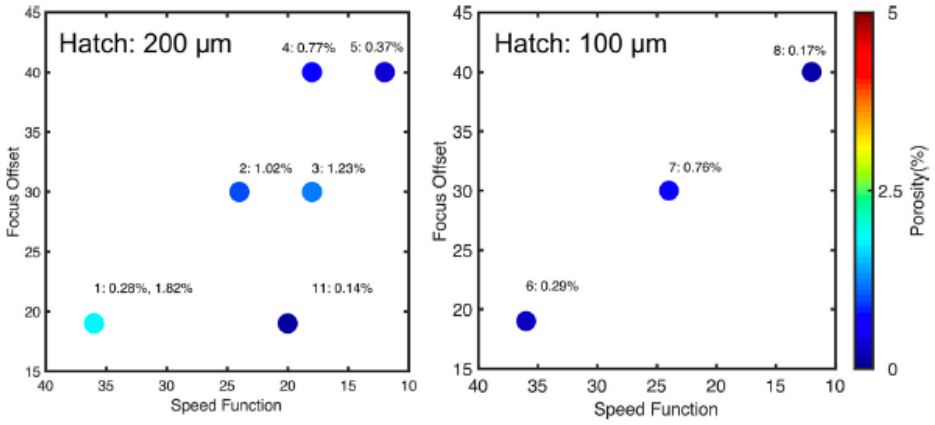

Figure 3.15 Percent porosity as a function of speed function and focus offset for two different hatch spacing values using the standard spherical powder. Compared with Figure 3.14, the process window includes larger values of speed function, thus, higher deposition rates.

Figure 3.16 compares the porosity distributions of the parts fabricated with (i) HDH powder using the optimized parameters (blue and black curves) and the nominal parameters (red curve) and (ii) spherical powder using the nominal parameters (green curve). The red curve represents the porosity distribution in the HDH parts fabricated using the nominal parameters that were originally developed for the spherical powder. By contrast, the black curve represents the porosity distribution in the HDH parts fabricated using the optimized parameters developed in this work. The black curve shifted towards the lower ESD compared with the red curve. Evidently, systematic optimization reduced the porosity levels in the HDH parts to closely match the porosity levels in parts fabricated using the spherical atomized powder (green curve). The

same figure also demonstrated the build-to-build variability with different porosity distribution curves for HDH builds with SF24FO30HS100. Overall, a shift in the porosity distribution is clearly evident with changing process parameters. These results also demonstrated the potential to achieve nominal porosity levels even when using the irregularly shaped HDH powder.

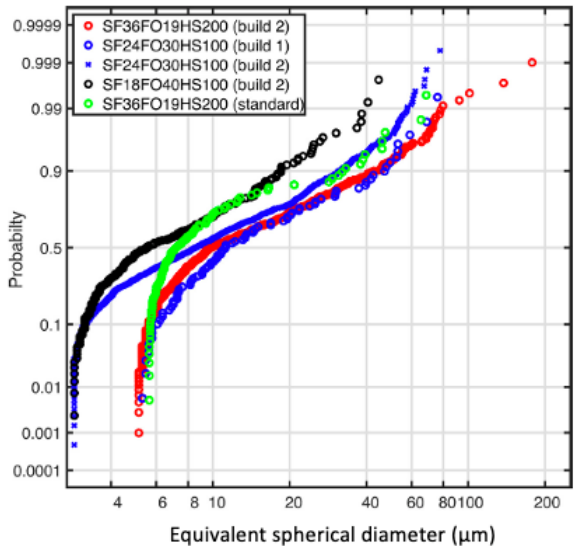

Figure 3.16 A comparison of probability distributions of porosity in parts fabricated with speed function (SF), focus offset (FO), and hatch spacing (HS) combinations in the optimal process window for the HDH powder and the nominal SF, FO, and HS for the spherical powder. Note that standard refers to the build using the spherical powder and build 1 and build 2 refers to the first and the second optimization builds using the HDH powder.

The optimal parameters required a lower beam travel speed to increase the melt pool size, and a smaller hatch spacing to increase the remelting. Hence, a basic build time analysis was performed to quantify the increase in build time caused by the modified process parameters. Figure 3.17 shows a decrease in beam travel speed with decreasing SF. The beam travel speed information was derived from videos captured during the deposition process for samples with different speed functions and a beam current of 17 mA. The captured videos were later analyzed

to estimate the time taken to melt a layer of each block which is referred to as layer time. Figure 3.18 summarizes the layer time at different speed functions and hatch spacings. For instance, based on the optimization performed in the current work, the optimal parameter set for the HDH powder in an Arcam S12 machine is SF18FO40 with a hatch spacing of 100 µm, and the nominal parameter set for the atomized powder is SF36FO19 with a hatch spacing of 200 µm. As per the build time measurements, when fabricating a multilayer block, the machine takes 262.4 s to deposit a 20 x 20 mm^2 layer if using the nominal parameters for the atomized powder but a much longer 936.7 s if using the optimized parameters for the HDH powder. This means that the use of the lower cost powder comes at an expense of the increase in deposition time. This build rate information can support the decision-making process by comparing the competing effects of the fabrication time and powder cost for the use of HDH powder in potential applications. There are other factors that affect the cost such as postprocessing and powder recycling. A comprehensive cost analysis is outside the scope of the current work; although there are opportunities to develop a decision-making tool considering all the aforementioned factors.

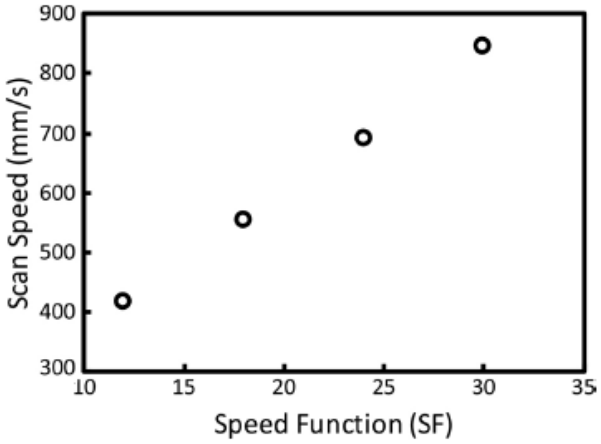

Figure 3.17 Empirical mapping of the relationship between speed function and scan speed at a constant beam current of 17 mA in an Arcam S12 machine.

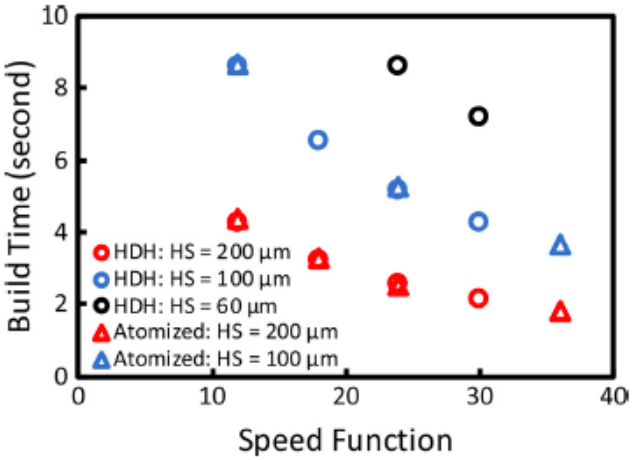

Figure 3.18 Plot illustrates that the change in the deposition time as a function of speed function and hatch spacing significantly impacts the deposition time for different process conditions.

3.4.3. Printability in L-PBF

The HDH powder is much coarser than the standard EOS Ti-6Al-4V powder (D_{50} = 39 ± 3 µm) meaning that the standard layer thickness of 30 µm might be too small. To minimize the chance of powder bed streaking specifically caused by the large powder particles, all builds utilized the 60 µm layer thickness, i.e., 120 µm powder layer thickness. As shown in Figure 3.19, no significant spreading defect on the powder bed was identified through visual inspection.

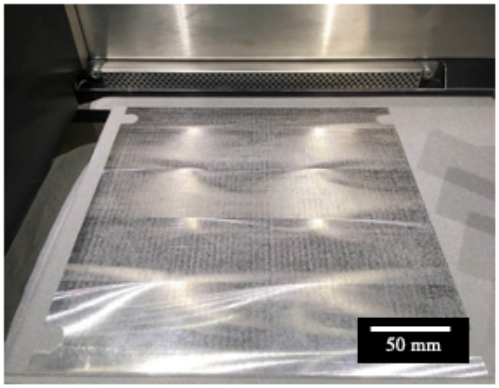

Figure 3.19 Powder bed of the HDH powder with 60 µm layer thickness in an EOS M290 L-PBF machine.

Figure 3.20 maps the porosity content in the as-built HDH parts from the first L-PBF build in the laser power and velocity space. The results successfully revealed the approximate range for the process window, the keyhole boundary, and the lack-of-fusion boundary. To limit the level of porosity to below 1 %, a minimum power of 225 W and a minimum velocity of approximately 800 mm/s were required to provide sufficient penetration into the thicker powder layer, while simultaneously maintaining a stable melt pool thereby limiting the formation of keyhole porosity. Samples #5 and #9 are classic examples of lack-of-fusion since the porosity contents rose from ~ 1 % to > 7 % as the input energy decreased. Samples #1, #2, #3, and #6 represent more extreme cases of lack-of-fusion. At such low power levels, the laser failed to fully penetrate the powder layer resulting in powder agglomerates instead of a solid block after fusion. The extreme lack-of-fusion was unseen in the fabrication using the standard powder but was reasonable since the HDH builds doubled the nominal layer thickness making full laser penetration much more difficult.

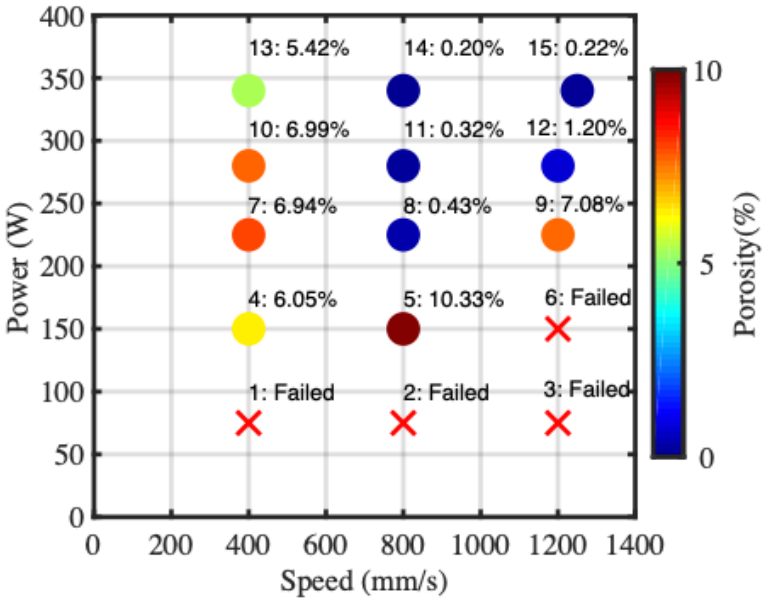

Figure 3.20 Porosity contents of the as-built parts from the first L-PBF HDH build measured using cross-sectioning method.

Figure 3.21 summarizes the porosity contents in the as-built parts from the optimization build in the HDH powder measured using the Archimedes' principle. These porosity maps further refined the location of the process window (porosity < 1 %) and showed good agreement with the preliminary porosity measurements from the cross-sections in Figure 3.20. Comparing the porosity maps at different hatch spacings, the lack-of-fusion boundaries can be found to shift towards the higher power levels; this agrees with the lack-of-fusion criterion developed by Tang *et al*. [40]. But even at 150 μm hatch spacing, a reasonable size of process window can be realized.

Based on the measurements from the Archimedes' method, Figure 3.21, the optimal parameter sets locate between 1000 and 1250 mm/s and between 300 and 400 W with energy density around 39 to 65 J/mm^3 depending on the selected hatch spacing. The maps also revealed the potential transition from the process window to the balling regime by showing consistently increasing porosity contents at higher velocity levels, i.e., from 1250 to 1500 mm/s. On the other hand, the maximum laser power of 370 W produced parts with low porosity content over a wide range of scan velocities up to 1250 mm/s. That said, if higher laser powers were available, the actual process window might extend to higher velocities, which would increase the productivity of the process. Our process window for the HDH powder can already achieve a similar build rate with little sacrifice of part quality, when comparing with builds using the standard Ti-6Al-4V powder in L-PBF [120].

Surprisingly, the optimal parameter range for the HDH powder is similar to the nominal parameter for the standard Ti-6Al-4V powder at 60 μm layer thickness meaning that the HDH parts with low defect concentration can be built in L-PBF process without sacrificing build rate. This is important for the ultimate goal of using the HDH powder which is to lower the total

fabrication cost by reducing the feedstock cost. Unlike the situation in the EBAM process as discussed in section §3.4.2., since the build rate was not sacrificed by replacing the powder, the cost reduction was maximized. It is worth pointing out again that the major fraction of the HDH powder (D_{50} = 101 µm) used in this study is about 2.5 times coarser in average size than the standard spherical EOS Ti-6Al-4V powder (D_{50} = 39 µm). This successful attempt demonstrated that the HDH powder is a cost-efficient alternative to the standard spherical powder in L-PBF process for many applications even when the layer thickness is approximately the same dimension as the powder D_{50}. In regard to the use of the non-spherical HDH powders in L-PBF:

a. For parts that will be HIPed after the additive process, as most aerospace parts are, the reported residual porosity is of little or no consequence.

b. For parts that will be used as-is, without the benefit of HIP after the additive part has been built, a finer powder size distribution (with better packing efficiency) of the HDH powder should be considered.

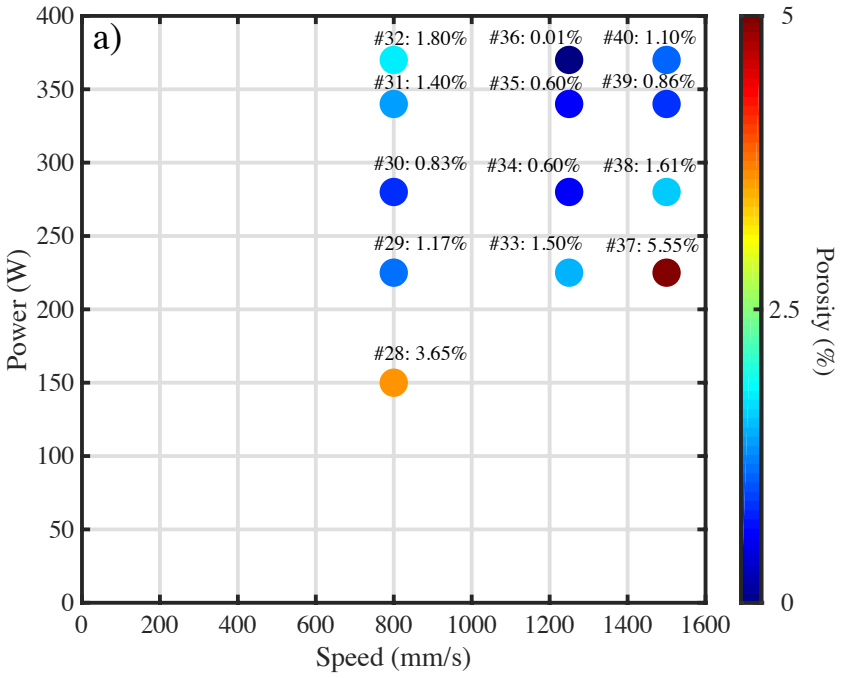

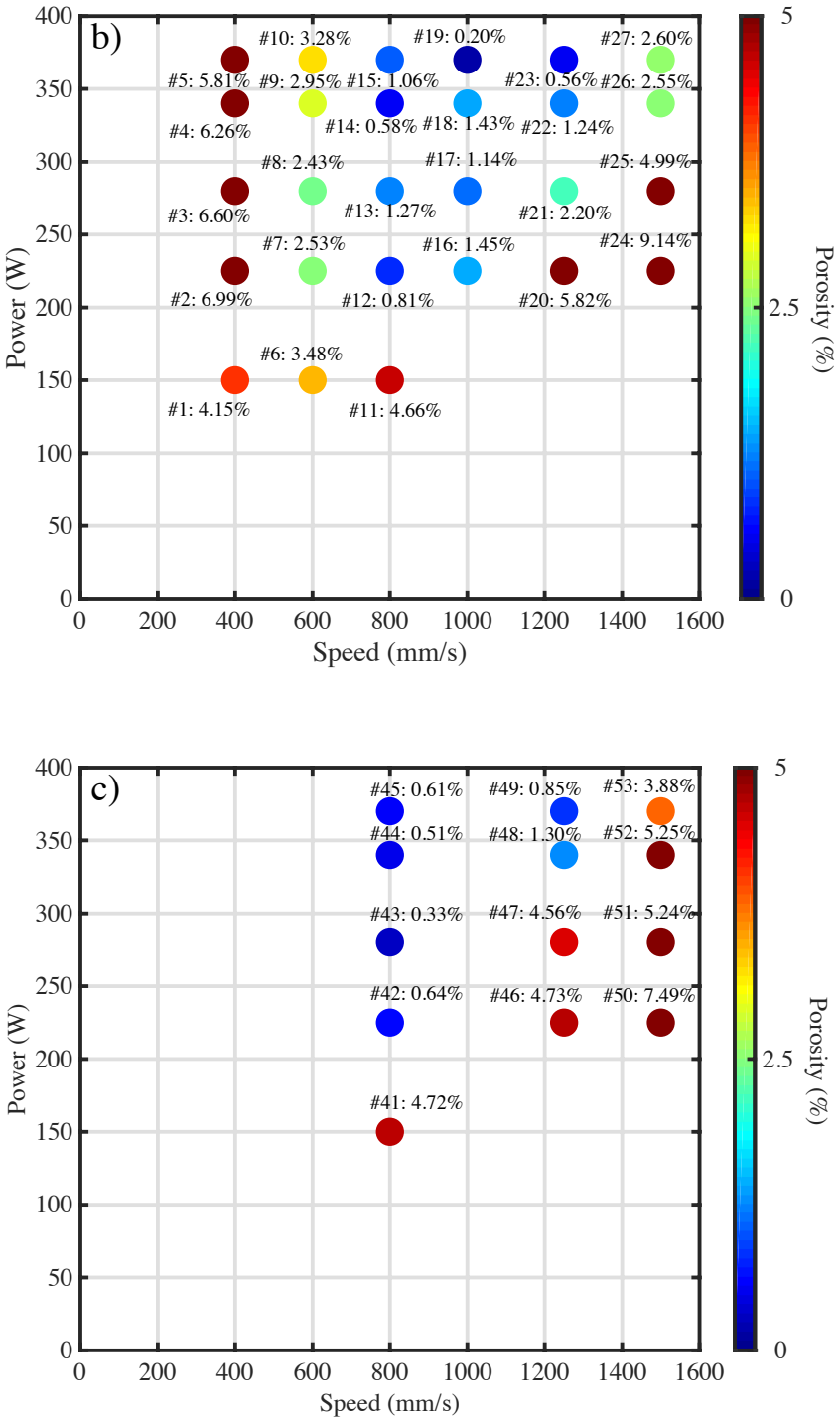

Figure 3.21 Porosity contents of the as-built parts from the L-PBF optimization builds using the HDH powder at a) 90 µm, b) 120 µm, and c)150 µm hatch spacing measured using the Archimedes' method.

3.5. Validate Density Measurements of The As-built L-PBF Components

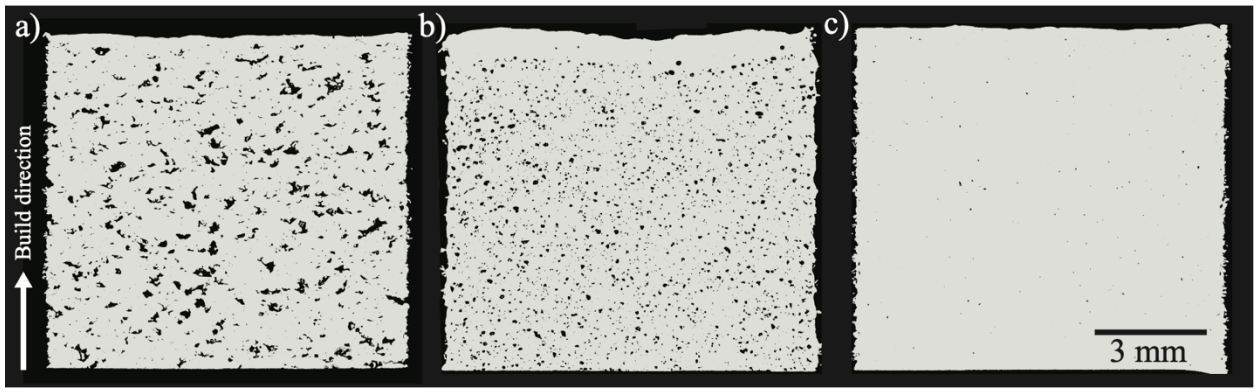

Figure 3.22 Examples of cross-section stitched by multiple optical micrographs showing the porosity resulting from the a) lack-of-fusion (1250 mm/s and 225 W), b) keyhole (400 mm/s and 370 W), and c) optimized (1000 mm/s and 370 W) parameters.

Figure 3.23 mapped the porosity contents (hatch spacing of 120 µm) of the as-built HDH parts, measured using the Archimedes' principle, as well as the cross-sectioning approaches (see examples in Figure 3.22) in a P-V space. The measurements from the two methods displayed reasonable agreement despite the fact that the Archimedes' principle measurement would account for more (closed) porosity than the cross-sectioning approach in the stable melting regime. This difference could be attributed to the fact that the cross-sectioning method only examined a slice of the 3D volume. Conversely, in the case of the presence of the surface-connected open pores such as lack-of-fusion, the cross-sectioning approach recorded higher porosity content because these open pores were omitted from the volume measurement and treated as the external surface by the Archimedes' method. Regardless of the techniques, the results revealed a process window that yielded a density over 99 % for the HDH powder (in the L-PBF process). In addition to this, a keyhole transition boundary, and a lack-of-fusion transition boundary were also identified. The parameter set of 370 W, 1000 mm/s, and 120 µm hatch

spacing resulted in the minimum porosity of 0.10 % and 0.19 %, as given by the cross-sectioning method, and the Archimedes' method, respectively.

The recent work of Zhao *et al*. [61] identified the boundaries of keyhole porosity formation in laser melting Ti-6Al-4V as labeled in Figure 3.23. While the formation of keyhole pores is predominately caused by keyhole instability and acoustic wave pinching mechanism [61,121], the boundaries became less sensitive to the scan velocity at higher laser powers. The mismatch between the keyhole boundaries in the bare plate and the powder-added setup suggested that the deposition of spherical powder expanded the keyhole porosity regime to higher scan velocities for a constant power; however, the expansion seems insufficient to explain some porosity results in this study. For instance, a substantial increase of porosity content appeared at parameters with scan velocity of 600 mm/s which is a value that should locate in the stable melting regime according to the reported boundaries. This implies that the powder could affect the actual fabrication in a non-trivial manner especially when using non-spherical powder. The underestimated role of the non-spherical powder motivated the study of the laser-metal interaction in ultra-fine spatial and temporal scale by using DXR where the process settings were kept consistent except the powder type (see discussion in section §4.4.4. below).

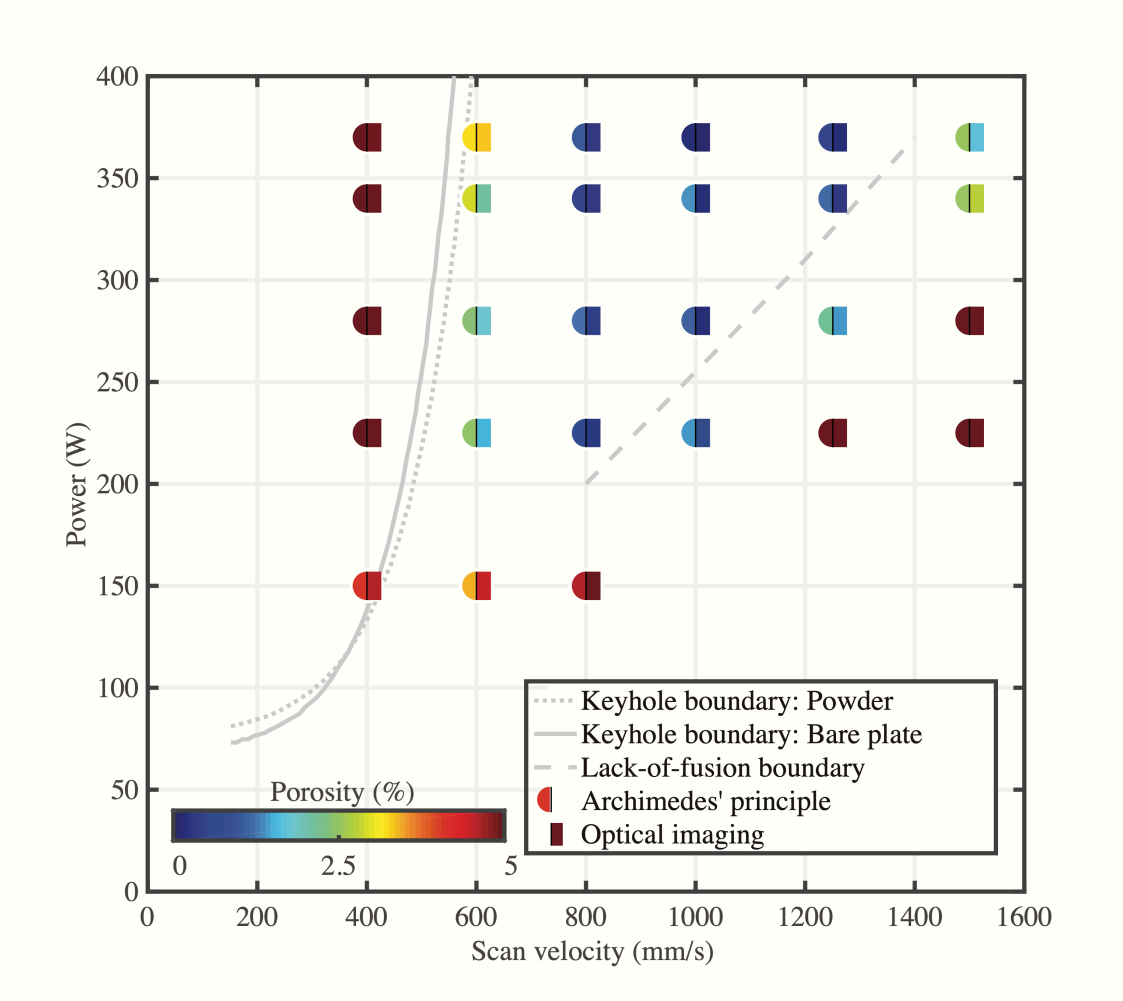

Figure 3.23 Porosity map of the as-built HDH Ti-6Al-4V parts from the L-PBF build at a hatch spacing of 120 µm measured using the Archimedes' principle and the cross-sectioning approaches. Note that the lack-of-fusion boundary was a prediction estimated based on the criterion developed by Tang et al. [40] *and the two keyhole boundaries were adopted from the publication of Zhao et al.* [61]. *The values of the density measurements can be found in Table 3.11.*

Table 3.11 Process parameters and part densities of the L-PBF parts fabricated using the HDH powder and hatch spacing of 120 µm. Note that the specimen with the highest density is

*highlighted in **bold**. Sample used for μXCT studies are identified with additional labels, L#1 – L#4.*

Sample #	Scan velocity (mm/s)	Power (W)	Hatch spacing (mm)	Density measured using Archimedes' principle (%)	Density measured using optical imaging (%)
#1	400	150	0.12	95.85	95.35
#2	400	225	0.12	93.01	93.98
#3	400	280	0.12	93.40	92.60
#4 (L#2)	400	340	0.12	93.74	93.27
#5	400	370	0.12	94.19	95.03
#6	600	150	0.12	96.52	95.47
#7	600	225	0.12	97.47	98.42
#8	600	280	0.12	97.57	98.14
#9	600	340	0.12	97.05	97.84
#10	600	370	0.12	96.72	96.61
#11 (L#1)	800	150	0.12	95.34	90.42
#12 (L#3)	800	225	0.12	99.20	99.66
#13	800	280	0.12	98.73	99.56
#14	800	340	0.12	99.42	99.62
#15	800	370	0.12	98.94	99.62
#16	1000	225	0.12	98.55	99.25
#17	1000	280	0.12	98.86	99.84
#18	1000	340	0.12	98.57	99.83
#19	**1000**	**370**	**0.12**	**99.80**	**99.90**
#20	1250	225	0.12	94.18	92.63
#21	1250	280	0.12	97.80	98.55
#22 (L#4)	1250	340	0.12	98.76	99.63
#23	1250	370	0.12	99.44	99.80
#24	1500	225	0.12	90.86	84.50
#25	1500	280	0.12	95.01	94.65
#26	1500	340	0.12	97.45	97.19
#27	1500	370	0.12	97.41	98.28

3.6. Conclusions & Hypothesis Revisited

This chapter is mainly focused on showing that the HDH powder can be successfully used in the EBAM and L-PBF process albeit its large powder size and irregular morphology. Through process parameter optimization, both processes were able to produce HDH parts with comparable levels of porosity to builds using standard spherical powders.

Hypothesis 3.1. has proven to be partially true. The optimal part density for EBAM HDH as-built parts is 99.82 % which is slightly lower than the goal of 99.9 %. The porosity benchmarking study has demonstrated the inherent variability of the EBAM machine which is significantly larger than the 0.08 % difference between the optimum and the goal. Additionally, the results based on the EBAM build using the standard powder reported a density of 99.83 % at the corresponding parameter set. This finding further supports *hypothesis 3.1*. However, based on the preliminary μXCT results in the upcoming section §4.4.1., the optimized parameter sets only resulted in around 98 % density in the EBAM as-built HDH parts. The following task is to eliminate the possibility of making mistakes during data analysis but meantime it is important to recognize the variabilities came from the measurement techniques. The current target of 99.9 % density is somewhat arbitrary. A more reasonable porosity threshold can be determined according to the porosity level which can result in comparable mechanical properties as the standard Ti-6Al-4V AM parts.

Hypothesis 3.2. has proven to be partially true for similar reasons as *hypothesis 3.1*. Using the HDH powder resulted in optimal densities of 99.80 % and 99.90 % in the L-PBF builds measured by the cross-sectioning method and the Archimedes' approach, respectively. Since the optimal specimens are basically fully dense, the actual difference in densities may just be a second order effect compared with the variability introduced by the machine and during the

porosity measurement. The variability was evident by the variation of porosity contents for parameters in the process window.

4. Investigation of Pore Formation in HDH Ti-6Al-4V AM Builds

The chapter was adapted from the publication of Wu *et al*., Study of Printability and Porosity Formation in Laser Powder Bed Fusion Built Hydride-Dehydride (HDH) Ti-6Al-4V published in Additive Manufacturing (2021).

4.1. Introduction

The previous chapter has demonstrated the printability of the irregularly shaped HDH powders in both the EBAM and L-PBF processes. Despite the optimization effort, limited laser/electron beam parameters showed promise of delivering parts with > 99 % density when using the HDH powders compared with when using the standard spherical powders. The µXCT analysis in this chapter suggested that the parameter optimization was less effective to reduce the pores with diameter < 50 µm which constitute a large portion of the porosity population in the as-built parts. These pores are unlike any standard types of pores resulted from the common mechanisms, e.g., lack-of-fusion and keyholing, since their corresponding process parameters have been optimized. Additionally, the HDH powders also shifted the stable-to-unstable keyhole boundary towards the lower energy density as shown in section §3.5. The boundary shift suggested that the laser-powder interaction was different in a HDH powder bed to impact the pore formation at high energy density regime.

This chapter aims to i) quantify the in-part porosity and show how process parameter optimization affects the in-part porosity content in 3D, ii) visualize and understand the pore formation related to the characteristics of the HDH powder by using *in-situ* and *ex-situ* synchrotron-based x-ray techniques, and iii) propose pore formation mechanisms based on the unique HDH powder characteristics to explain the formation of the residual pores (< 50 µm) and the shift of the keyhole boundary.

4.2. Hypothesis

Hypothesis 4.1. The low packing density spots (< 35 %) in the HDH Ti-6Al-4V powder bed are responsible for the formation of pores with diameter < 50 µm in the as-built AM parts.

Hypothesis 4.2. HDH powder particle is responsible for the formation of pores by promoting unstable melt pool/keyhole fluctuation.

4.3. Methods

µXCT was performed at the 2-BM beamline of the APS at ANL. A monochromatic beam with 0.5 s exposure or a pink beam with 0.024 s exposure illuminated the HDH solid specimens fabricated in the EBAM and L-PBF processes. See other µXCT settings and the details about the reconstruction and analysis process in section §2.2.1.

From the EBAM and L-PBF builds shown in Chapter 3, this study selected as-built specimens in various parameter sets, from baseline to optimal, to show the spatial distribution and morphology of the in-part porosity. Table 4.1 and Table 4.2 list the build parameters of the as-built specimens characterized using µXCT. In addition to the as-built materials, a sample of the HDH powder was prepared by packing in a Kapton tube with 1 mm inner diameter.

Table 4.1 Process parameters of the EBAM as-built HDH specimens used in the µXCT characterization.

Sample #	Speed function	Focus offset (mA)	Hatch spacing (µm)	Exposure (s)
EB#1	36	19	200	0.5
EB#2	18	35	200	0.004
EB#3	18	35	100	0.5
EB#4	12	40	100	0.004

Table 4.2 Process parameters of the L-PBF as-built HDH specimens used in the µXCT characterization.

Sample #	Power (W)	Velocity (mm/s)	Hatch spacing (μm)	Exposure (s)
L#1	150	800	120	0.5
L#2	340	400	120	0.5
L#3	225	800	120	0.5
L#4	340	1250	120	0.5
L#5	340	1250	80	0.5

Powder added single-bead melting experiments were performed at the 32-ID-B beamline of the APS at ANL and monitored using the high-speed x-ray imaging approach to study the formation of the HDH powder related porosity. The detailed DXR setup was given in section §2.2.3. Experiments in a wide range of power and velocity combinations were conducted.

4.4. Results & Discussions

4.4.1. X-Ray Microtomography

Figure 4.1 reveals the spatial distribution of porosity in the as-built EBAM parts with various parameter sets, Table 4.1. Based on the μXCT measurements, the overall porosity concentrations in EB#1, EB#2, EB#3, and EB#4 are 80.87 %, 98.53 %, 97.63 %, and 97.84 %, respectively. Compared with the nominal case EB#1, the optimized parameters reduced the porosity by more than 18 %. However, the overall percentages calculated based on the μXCT data were much higher than those measured using the cross-sectioning method reported in Figure 3.14. Especially for the unoptimized case (EB#1), it is about 4 to 8 times higher. The porosity results are heavily dependent on the measurement technique. That said, *hypothesis 3.1* is only supported by the results from the cross-sectioning method but not by μXCT. Other potential causes of this mismatch include different volumes of sampling in the two techniques and bias of sampling location.

In the optimized cases (EB#2, EB#3, and EB#4), all the pores are smaller than 60 μm. The frequency of pores decreased with increasing pore diameter, but the bigger pores still

contributed more to the total volume of porosity. By contrast, the nominal case (EB#1) appeared to be more porous in terms of both number and volume densities across the whole size spectrum. The residual pores are the particular focus of the future work in this chapter and believed to be induced by formation mechanism related to the characteristics of the HDH powder. Packing analysis motivated by this observation will be discussed in section §4.4.2.

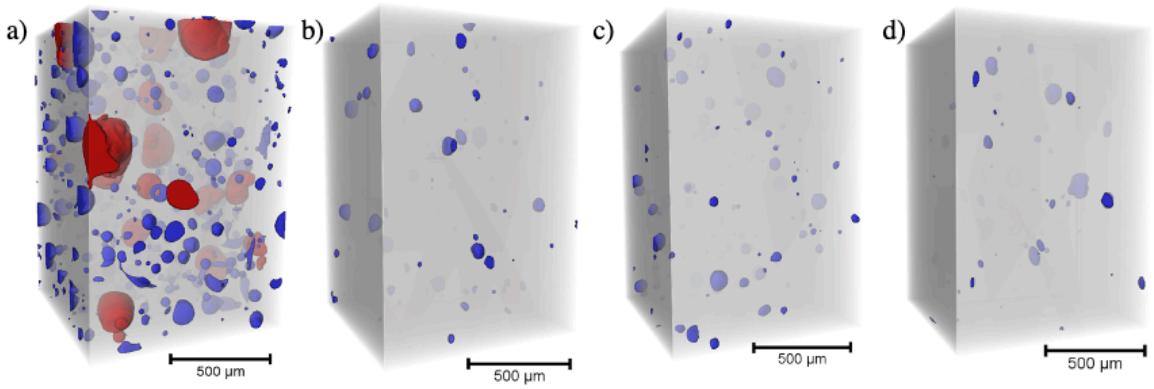

Figure 4.1 µXCT reconstructions of the EBAM specimens fabricated using the HDH powder with parameters of a) SF36FO19HS200, b) SF18FO35HS200, c) SF18FO35HS100, and d) SF12FO40HS100. Note that the larger pores (ESD > 60 µm) were highlighted in red and the smaller pores (ESD < 60 µm) were highlighted in blue.

Figure 4.2 shows the spatial distribution of porosity in the as-built parts with various parameter sets, Table 4.2. Based on the µXCT measurements, the overall porosity densities in the parts are 92.56 %, 96.78 %, 99.38 %, 99.73 %, and 99.83 %, see Figure 4.2a-e. L#3, L#4, and L#5 are the three specimens fabricated using the parameters in the process window. In these specimens, the pores were predominately small (< 50 µm) as shown by the number density in Figure 4.3a. The medium-sized pores (50 – 120 µm) appeared less frequently and they were speculated to be the result of the inherent variability of the machine. However, their volume fractions were on the same order of magnitude as the smaller pores suggesting that these pores

were equally concerning, if not more, for any defect sensitive applications. Within the process window, the porosity can be further reduced by using parameters of higher power, higher speed, and smaller hatch spacing. An important finding was that optimizing parameters within the process window showed limited effect on the number and volume densities of the medium-sized pores (50 – 120 μm). This supports the speculation that the medium-sized pores were originated from machine variability. Although the optimization strategy successfully reduced the population of the smaller pores (< 50 μm), significant amount of them remained in the as-built specimens and held the specimens back from reaching > 99.9 % density even with the optimal parameter sets like L#4 and L#5. Moreover, the options of parameters that can deliver HDH parts with > 99.5 % density are limited compared with the availability of parameters for the standard spherical powders. The optimal range of energy density for the HDH powders is from 39 J/mm^3 to 65 J/mm^3. The Monte Carlo packing analysis in section §4.4.2 aims to reveal and explain the correlation between the unique powder packing characteristics of the HDH powders and the formation of these residual pores.

The laser at 800 mm/s and 150 W produced insufficient energy which induced irregularly shaped lack-of-fusion pores with recognizable pattern, i.e., interconnected and align between scan paths. As shown in Figure 4.3, the density of the smaller pores in L#1 remained at a similar level as L#3, L#4, and L#5 and the density of the larger pores increased significantly due to the energy deficit. Figure 4.3 shows that pores ranging from 50 to 120 μm dominated the population and volume in sample L#2 and they can even be identified from Figure 4.2b. Although keyhole pores were expected as L#2 used a high-power and low-velocity parameter set, 400 mm/s and 350 W, the dramatic increase of porosity content between 50 and 120 μm was still intriguing. This finding and the shift of keyhole boundary discussed in section §3.5 motivated the study in

section §4.4.4. of using the *in-situ* x-ray technique to understand how the usage of the HDH powder affected the stability of the keyhole/melt pool and induced pore formation.

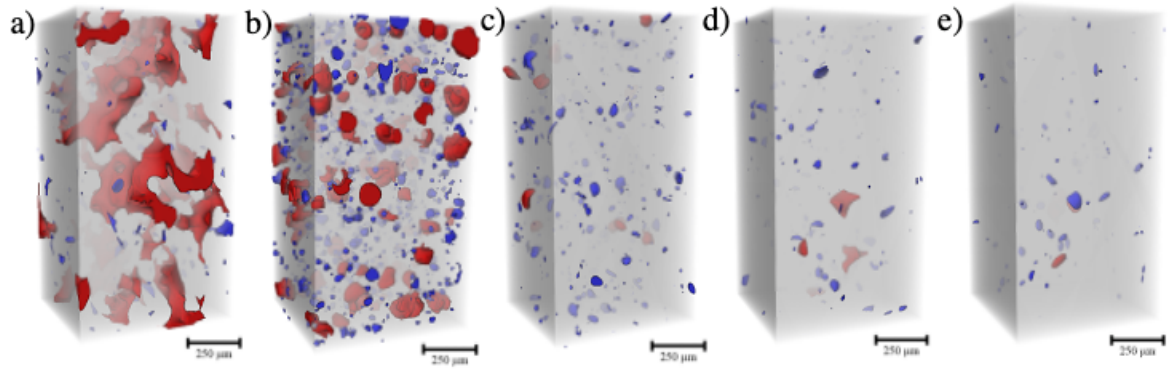

Figure 4.2 µXCT reconstructions of the L-PBF specimens fabricated using the HDH powder with parameters of a) 800 mm/s & 150 W (HS: 120 µm), b) 400 mm/s & 340 W (HS: 120 µm), c) 800 mm/s & 225 W (HS: 120 µm), d) 1250 mm/s & 340 W (HS: 120 µm), and e) 1250 mm/s & 340 W (HS: 80 µm). Note that the larger pores (ESD > 50 µm) were highlighted in red and the smaller pores (ESD < 50 µm) were highlighted in blue.

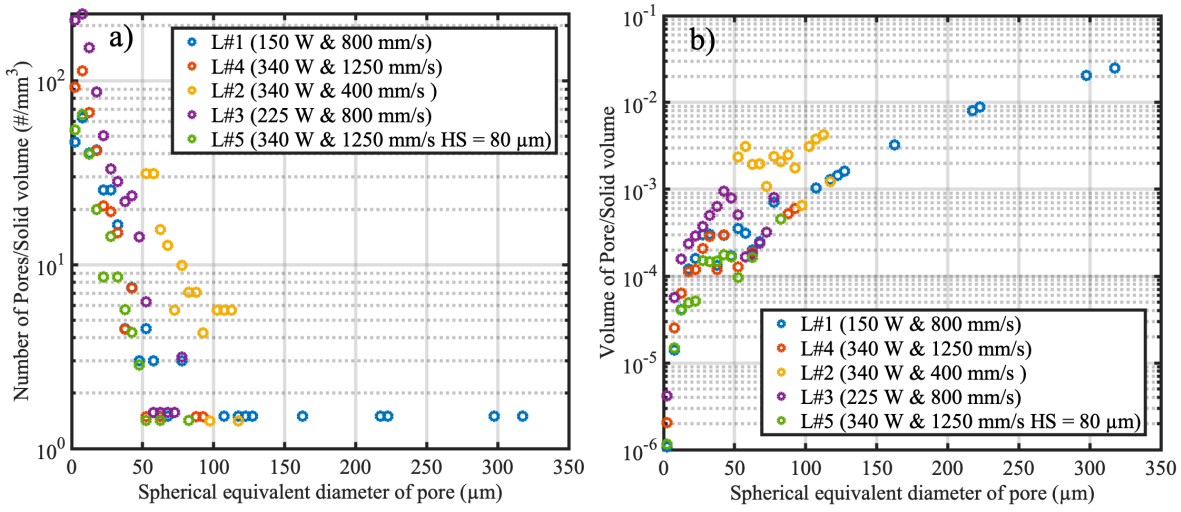

Figure 4.3 a) Number density and b) volume density of porosity in the as-built L-PBF parts fabricated using the HDH powder. Note that the bin size is 5 µm meaning that each data point summarized all pores with diameter of ± 2.5 µm within the bin center.

4.4.2. HDH Powder Packing

The Monte Carlo image-based analysis used the μXCT images of the Ti-6Al-4V powders manufactured from 9 different processes as input, see Table 4.3. The spherical powders from PREP, HDH plus plasma spheroidization (P-S), and GA have different size distributions and morphologies compared with the HDH powder. They were used in the analysis to demonstrate how the powder characteristics affect the packing. The input images were 2D slices from a 3D reconstruction of powder where image stripes with thickness of 120 μm were extracted as shown by Figure 4.4a. Each stripe was then stacked on top of a 240 μm thick dark image, which is equivalent to four 60 μm solidified layers if the shrinkage is assumed to be 50 % in an L-PBF process as the typical average powder bed packing is around 50 % - 65 % as shown in Table 4.3. Scime [122] demonstrated that the powder layer thickness at steady state was not equivalent to the solid layer thickness in powder bed AM process but instead followed a converging rule determined by both the solid layer thickness and powder packing fraction. In Figure 4.4b, the black pixels represent the solid material, i.e., substrate and powder, and the white pixels represent the empty volume, i.e., air pockets between particles. This powder bed image was intended to replicate a L-PBF powder bed consisting of a 120 μm thick powder layer on top of fully dense solidified layers. As shown in Figure 4.4c, the radii of the semi-circular cross-section of the melt pool varied from 39 to 420 μm. Figure 4.4d shows the area on which the packing fraction was calculated; it is the overlapping area between the powder bed image and the semi-circular melt pool. For each melt pool size, the Monte Carlo analysis iterated the packing calculation on 661 powder bed images to capture sufficient data. A proper sampling frequency balances the need for an accurate representation of the 3D volume and the computational cost. Accordingly, we studied how the local packing distribution varied with the sampling frequency.

The selected frequency was such that the distance between the adjacent images was ≈10 µm, i.e., significantly smaller than the average particle size. That said, the 2D sampling approach should reflect the packing statistics of the 3D volume albeit the reduced sample size.

Figure 4.4 Schematics of the Monte Carlo analysis' four-step setup including a) image segmentation from a 2D slice of the µXCT reconstruction of the HDH Ti-6Al-4V powder, overlaying c) a melt pool image on b) a powder bed image, and d) extracting powder bed within the melt pool region.

Table 4.3 Powder statistics of the nine Ti-6Al-4V powders used in the Monte Carlo analysis

Sample #	Production process	Materials	D_{10} (µm)	D_{50} (µm)	D_{90} (µm)	Average packing
P#1	HDH	Ti-6Al-4V	4*	101	175	53.9%
P#2	GA	Ti-6Al-4V	20	34	50	58.0%
P#3	PREP	Ti-6Al-4V	50	78	105	64.7%
P#4	HDH + P-S	Ti-6Al-4V	35	62	90	62.8%
P#5	GA	Ti-6Al-4V	23	32	46	53.0%
P#6	GA	Ti-6Al-4V	25	41	61	54.2%
P#7	GA	Ti-6Al-4V	28	48	73	56.2%
P#8	GA	Ti-6Al-4V	17	29	44	55.1%
P#9	GA	Ti-6Al-4V	33	48	73	65.6%

*Large population of fine particles (< 10 µm) caused difficulties for the measurement

The objective of the Monte Carlo packing analysis was to use a statistical method to demonstrate the connection between porosity formation and the packing of the HDH powder bed. The HDH powder was expected to have looser packing due to its larger particle size and irregular morphology. This has been shown to influence the packing density and other powder characteristics such as flowability in literatures [22,120]; however, studies often treated packing

density as a bulk property but overlooked the local variation in particulate scale which could be important because porosity formation is rather a localized event. In fact, in the geomechanics community, researchers [123,124] have noticed that the local void ratio could affect the compaction and water flow behaviors in the porous granular media and developed algorithms to quantify the local void ratio.

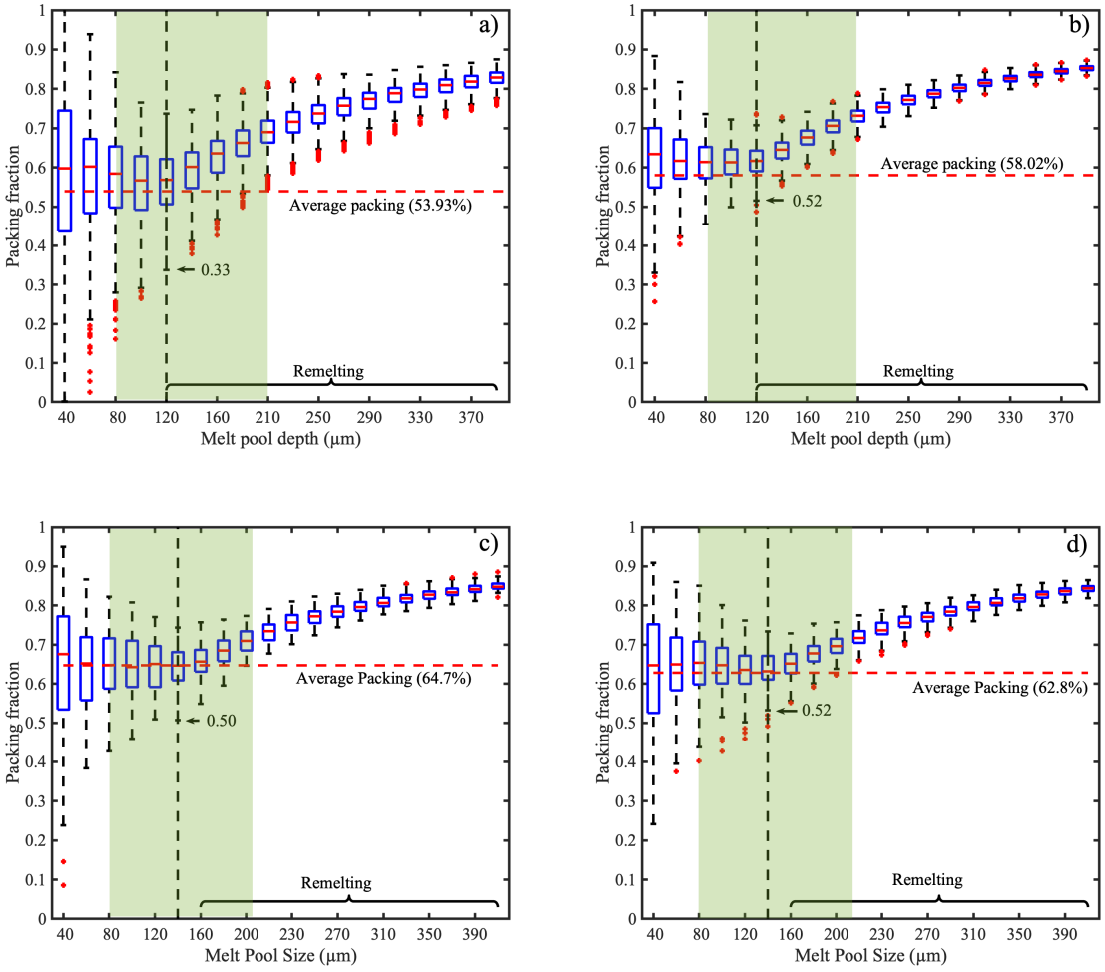

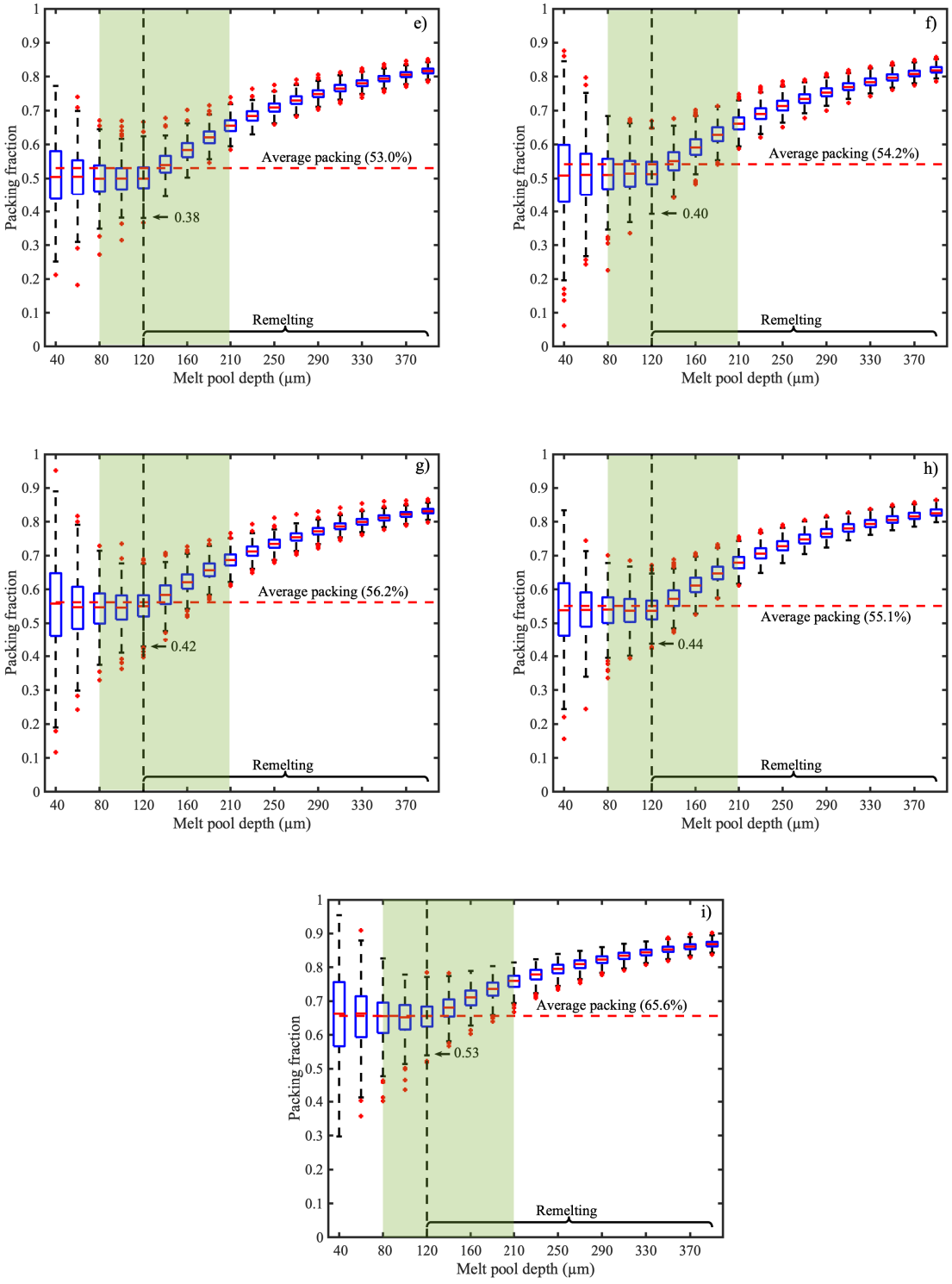

Figure 4.5 The packing fractions at different melt pool sizes for the a) HDH (P#1), b) standard EOS GA (P#2), c) PREP (P#3), d) HDH+P-S (P#4), and e) – i) GA (P#5 – P#9) Ti-6Al-4V

powder samples calculated by the Monte Carlo packing analysis. Note that each box extended to the 25th and 75th percentiles and the whiskers extended to the minimum and maximum excluding the outliners which were labeled in red. The green area represented the common size range of melt pools used in L-PBF.

For each melt pool depth given in Figure 4.5, the analysis accumulated 661 local packing calculations which were summarized in a boxplot series showing the median, the 25th and 75th percentiles, and the minimum and maximum without considering the outliers. As expected, the GA powder (P#2) showed a higher average packing density when compared to the HDH powder, with values of 58.02 % and 53.93 % respectively. Note that the average packing densities were evaluated using all the 2D cross-sections of the 3D μXCT volume as noted above. This difference in average packing is also reflected in the higher median packing fraction at every melt pool depth for the spherical powder case. More importantly, the HDH powder packed less homogeneously as illustrated by the larger spread between the maximum and minimum values for all melt pool depths. The variation of packing fraction significantly increased as the melt pool size decreased, especially when melt pool size was too shallow (< 120 μm) to remelt the previous layer. For melt pool depth < 60 μm, complete vacancy was frequently observed in the HDH powder bed whereas a minimum around 35 % packing was maintained in the GA powder bed. This suggested that the packing fraction was sensitive to local conditions, e.g., a large particle or large air pocket in the powder layer, when a melt pool depth was shallow. Increasing the sampling area by using a deeper melt pool can effectively mitigate this problem. The variation was further reduced, and the median packing fraction was further improved with larger melt pools that penetrated the powder bed and remelt the previous solidified layers (assumed to be 100 % dense in this analysis). With the common melt pool depths used in L-PBF as

highlighted in Figure 4.5, the GA powder maintained a minimum packing around 50 %; yet, the HDH powder bed possessed many low-packing density spots of 20 % - 40 % packing.

Besides the standard EOS GA powder, the packing of the HDH powder bed was compared with the additional seven Ti-6Al-4V powders manufactured by various atomization processes and with different particle size distributions as shown in Table 4.3. Among all powders, the average packing density of the HDH powder appeared near the lower end of the spectrum. The medians of the local packing fractions at every melt pool depth correlated with the average packing in all cases; however, the variations of the local packing fractions were not. For example, the PREP powder (P#3) has better average packing over the standard EOS powder (P#2) but the variations and the minima of the local packing fractions were clearly worse than its standard GA counterpart. Furthermore, the irregular powder morphology could impair the ability of average packing density to quantifying the packing quality of a powder bed. As shown in Figure 4.5, the average packing densities were similar among the HDH powder and the two GA powders (P#5 and P#6); yet, the HDH powder bed showed the highest population of low packing density spots especially when the melt pool size was small. In fact, of the seven powders shown in Figure 4.5, complete vacancy was not observed except in the HDH powder bed regardless of the melt pool depth. That said, both powder size distribution and powder morphology are important factors controlling the local packing characteristics. Larger variation implies that the beam is more susceptible to scan regions with extremely low packing density (< 35 %) during the fabrication. This suggests that the HDH powder bed has a larger concentration of low packing density spots than the others do, providing sites for the formation of pores and depressions on the top surface of the melt track. Additional discussions about the proposed porosity formation mechanism can be found in the following section.

Porosity formation may not be completely explained by this packing analysis since it does not take account dynamic effects during packing and uses a somewhat over-simplistic semi-circular melt pool geometry. Additionally, a μXCT powder specimen might not perfectly replicate the packing condition in an actual powder bed, even though the powder handling procedure was kept consistent across all powder samples. Nevertheless, the analysis provides a perspective of variability of local packing as opposed to average packing and quantifies the connection between the porosity formation and the actual packing of the HDH powder. The packing analysis also presents a potential countermeasure to the formation of large pores. In agreement with the findings of the melt pool geometry study, the analysis shows that larger melt pool area can lead to lower porosity.

To further test the hypothesis, a comparison between the concentration of low packing spots and the concentration of large pores needs to be carried out. If possible, comparing porosity size and morphology in parts fabricated in spherical powders is helpful to identify the critical low packing percentage which leads to the formation of pores.

4.4.3. Packing Variation Induced Pore Formation

It follows that, when using the HDH powder in a L-PBF process, the laser beam is more susceptible to scan regions with low-packing spots. Although it is not clear if air pockets can be directly transformed into porosity during laser melting, we speculate that they provide sites for porosity formation in an indirect way. If all the particles are assumed to be fully melted and deposited on the original locations without redistribution of molten metal, regions with lower packing are more likely to result in depressions on the top surface of a melt track due to lack of materials. As shown by the schematics in Figure 4.6, the materials highlighted in orange are the previous deposition where the height was calculated based on the local packing fractions of the

previous powder layer in Figure 4.6a. Figure 4.6b shows that a depressed site caused by a large air pocket at the previous powder layer forms a locally thick powder layer which could block the full laser penetration and remelting, and consequently lead to an unfused region in the as-built part.

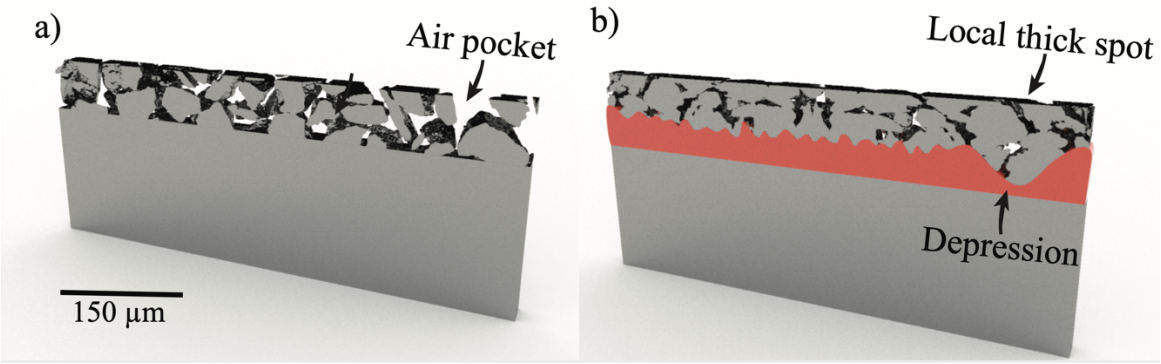

Figure 4.6 Schematics of a proposed porosity formation mechanism caused by local packing variation in a HDH powder bed where b) is the succeeding layer of a). Note that the materials highlighted in orange was solidified from the powder layer in a).

Evidence of the depressed sites was found from the top surface topology of the DXR single-bead melt tracks as shown in Figure 4.8 where the GA powder bed resulted in a more even distribution of deposited materials compared with the HDH powder bed. Features like deep valley and partially fused powder particles can be observed near the centerline the HDH melt track and they caused a higher R_z value (411.4 µm) over its GA counterpart (R_z = 122.9 µm). And this is not an exception; as shown in Figure 4.7, extreme R_z values were often observed from the HDH single-bead melt tracks produced using various laser process parameters. By contrast, the R_z values of the GA single-bead melt tracks maintained between 98 µm and 173 µm.

The proposed mechanism is akin to lack-of-fusion as both result in unfused voids. However, lack-of-fusion pores often display consistent and unique pattern which aligns with the

laser scan paths while the packing variation induced pores tend to be scattered spatially and smaller in volume as shown in Figure 4.2d. In fact, the observation in the study from Sinclair *et al*. [125] supports this mechanism by showing that the topology of a melt track affects the thickness of the subsequently deposited powder layers. The HDH powder bed also magnified the impacts from local thick spots since a larger layer thickness was already being used to accommodate the larger particle size. According to the Monte Carlo analysis, larger melt pool size can be effective to reduce the unfused spots by a) lowering packing variation and b) penetrating a thicker powder layer. However, the larger melt pool size is often not feasible because of the formation of keyholes at higher power densities.

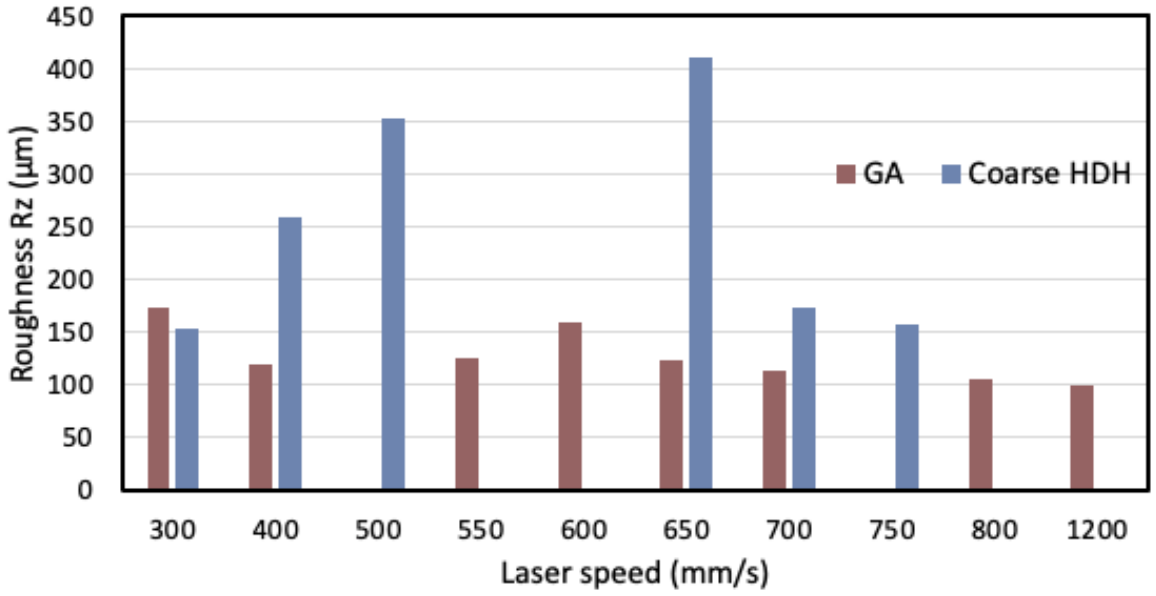

Figure 4.7 Top surface roughness measurements of the DXR single-bead melt tracks in the two different powders. Note that the laser power used in these experiments was 350 W.

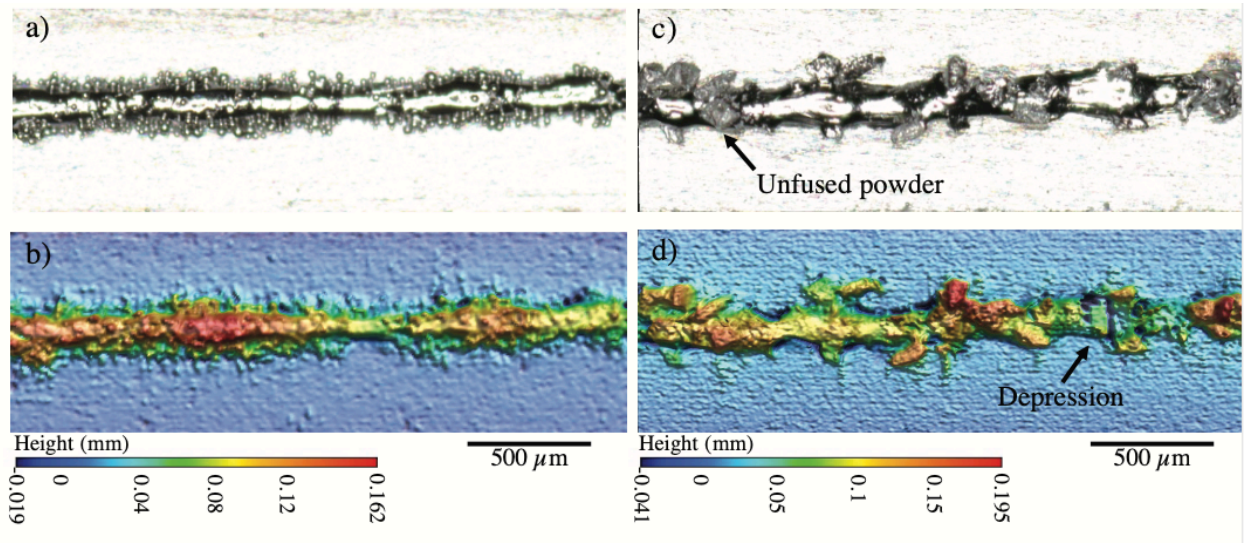

Figure 4.8 The top surface roughness (shown in the optical images and height maps) of the single-bead melt tracks corresponding to the DXR experiments using the a) & b) GA powder bed and c) & d) coarse HDH powder bed with a laser power of 350 W and speed of 650 mm/s.

4.4.4. Visualize Pore Formation Using DXR

Figure 4.9 shows the x-ray imaging snapshots captured in the laser scanning DXR experiments using the HDH powder, shown in a) and b), and the spherical GA powder, shown in c). Different x-ray absorptions generate contrast as the keyhole and entrapped pores appear to be brighter than the surrounding substrate and powder particles since they are composed of the thinner metal vapor and argon gas. As shown in Figure 2.3, the viewing direction of Figure 4.9a-c was parallel to the x-ray direction while the laser was directly above the keyhole and scanned from the left to right of the images.

To identify the stable-to-unstable keyhole transition boundary, a series of DXR experiments were performed at a laser power of 350 W and various laser scanning velocities. According to the keyhole boundaries in Figure 3.23, the combination of 350 W and 650 mm/s is within the stable melting regime; yet severe keyhole porosity was observed in Figure 4.9b. The

mismatch implies that the HDH powder behaved differently compared with the spherical GA powder and the bare substrate during laser melting. The HDH experiment experienced four complete cycles of keyhole porosity formation leaving four clusters of keyhole pores in the substrate as highlighted in Figure 4.9b. Figure 4.9a shows two of the cycles which started with the collapse of a deep keyhole followed by the ejection and entrapment of a keyhole pore, and finished with the keyhole depth recovery process. In fact, between 2.92 ms and 3.12 ms, one keyhole pore in the second pore cluster formed immediately after another. After releasing a pore, a keyhole experienced a dramatic shrinkage in depth which required longer time to recover compared with the regular keyhole fluctuation. Figure 4.9d labeled the starts of each periodic melt pool depth variation related to the formation of each cluster where the shallowest melt pool corresponds to the pore releasing event and the deepest melt pool indicates a full recovery. Such a long wavelength in the recovery process can be detected from the frequency spectrum in Figure 4.9e. The peak between 1042 Hz and 1389 Hz, which only occurred in the HDH experiment, is linked to the four complete porosity formation and keyhole recovery cycles as the separations between the pore clusters are about a few hundred micrometers. In the experiment using the GA spherical powder, a smaller number of pore clusters formed. After the formation of the first pore, the keyhole entered a steady state between 2.24 ms and 4.08 ms even when the second pore cluster formed at 3 ms. Additionally, the keyhole fluctuation in the HDH experiment was more violent as the standard deviation of its depth profile is 27.71 μm over the 19.04 μm measured in the GA powder experiment. That said, the severity of keyhole fluctuation influenced the transition of keyhole from the stable to unstable regime.

As discussed in the recent publications [61,126], laser shadowing occurs when a powder particle or a spatter blocks the direct light path to the substrate and leads to local cooldown and

melt pool shrinkage. Depending on the laser spot size and power, the melt pool depth showed different responses to the shadowing effect, but the strongest influence was associated with the larger particles. This implies that the laser shadowing is magnified in a HDH powder bed because of the larger powder size. Additionally, as suggested by the large packing variations from the Monte Carlo analysis, a HDH powder bed has lower number density of particles compared with a standard GA powder bed. Thus, the laser is more likely to impinge directly on the substrate after an ejected particle travels away from the laser path. As a result, the keyhole drills deeper causing the more violent keyhole fluctuation and the more severe porosity formation observed in the DXR experiment.

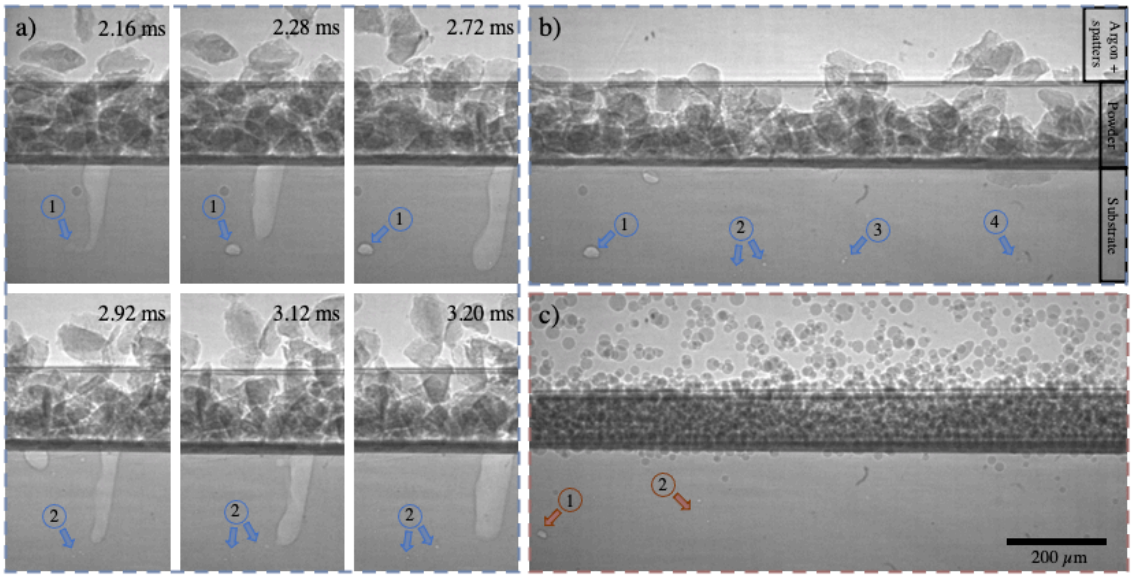

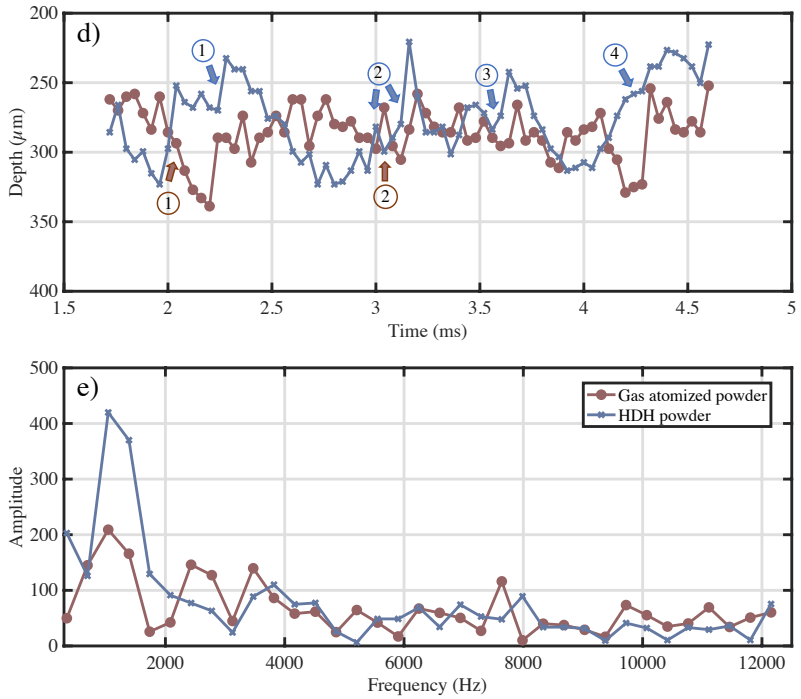

Figure 4.9 DXR frames collected in the powder added single-bead Ti-6Al-4V experiments at a laser power of 350 W and scan velocity of 650 mm/s showing a) two complete cycles of keyhole porosity formation when using the HDH powder and the porosity condition after laser scanning when using b) the HDH powder and c) the standard EOS GA powder. The keyhole depth profiles, and the corresponding Fourier transform spectrum are shown in d) and e). Note that the timestamp in a) is the time since the laser was initiated.

Figure 4.10 shows another single-bead experiment which was set up with a much more dispersed powder layer for the purpose of better capturing the interaction between the keyhole and a single HDH powder particle. The parameter set, 360 W and 800 mm/s, is in the process window for the HDH powder and produced a smaller melt pool with a shallower vapor cavity. The DXR video shows that a single HDH powder particle fell into the cavity and caused a pore to form near the top surface. At 4.02 ms, a HDH particle entered near the rear wall of the vapor cavity and initiated the formation of a protrusion by blocking the direct laser path. The upward

Marangoni flow extended the protrusion which later engulfed the back end of the cavity and induced the formation of a single pore at 4.06 ms. This pore quickly escaped from the melt pool and this could explain why low porosity content was observed in the as-built sample at this parameter set. However, this observation presented another evidence for the powder induced keyhole interruption due to laser shadowing.

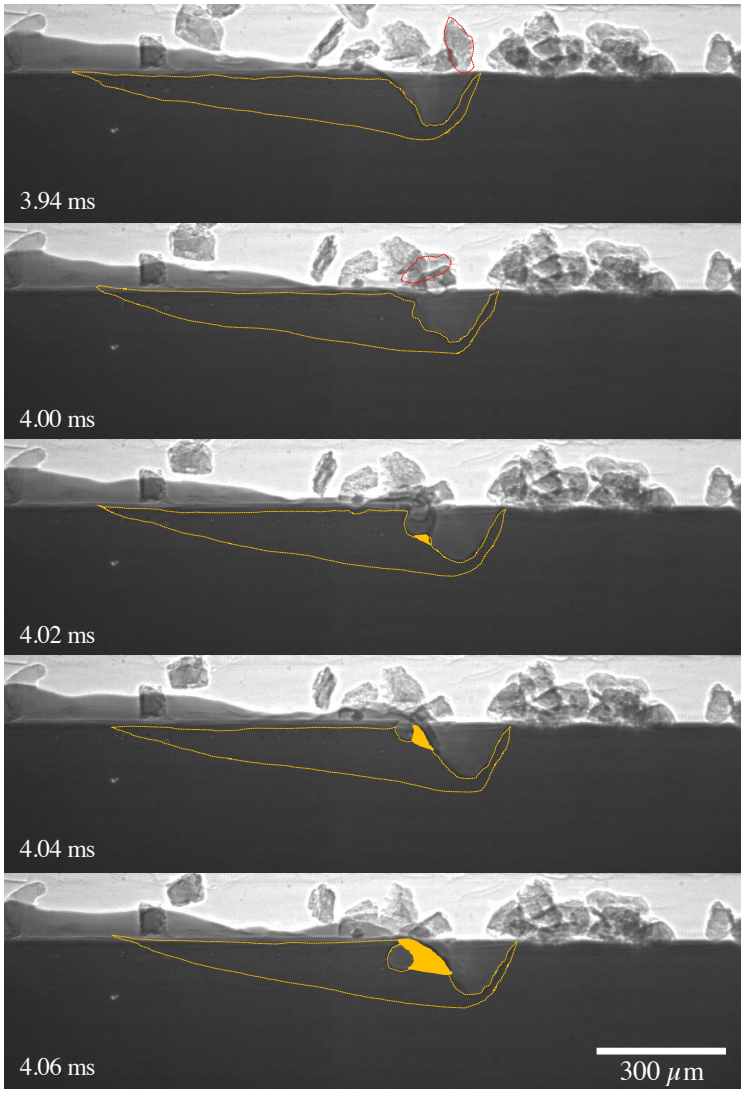

Figure 4.10 Individual frames from a DXR video showing the porosity formation sequence due to laser shadowing in the HDH powder added single-bead experiment using 360 W laser power

and 800 mm/s laser velocity. Note that the melt pool is highlighted in the yellow dash line, the powder particle is highlighted in the red dash line, and the protrusion is filled with yellow.

We agree that the DXR experiments do not perfectly represent the melting condition that occurs in a L-PBF system (or the EOS M290 in particular). In addition to the laser parameters, the DXR experiments involved in no scanning strategy, no remelting, and different boundary and powder spreading conditions. Nevertheless, the DXR experiments provide information about the unit process of melting, so the conclusions drawn from the DXR studies remain valid since none of them was based on the direct comparison between the DXR experiments and the actual fabrication. This study only intends to demonstrate that different melting/keyholing behaviors occurred in the different powder beds, i.e., non-spherical powder and spherical powder, within the DXR experiments where the laser parameters and layer thickness were kept consistent.

4.5. Conclusions & Hypothesis Revisited

The previous chapter demonstrated the printability of the HDH powder and the ability to mitigate porosity problem in the as-built part through parameter optimization. This chapter mainly focus on the unanswered question about the porosity formation mechanism. The μXCT results assisted the visualization of the possible HDH powder caused pores in 3D. Moreover, the DXR videos provided evidence of their formation and insight about the mechanism. A Monte Carlo powder packing analysis provided a different perspective to understand powder packing, i.e., local packing instead of average packing, and emphasized the role of local packing played in porosity formation events. In a spherical powder bed, it is reasonable to use average packing and local packing interchangeably since the spatial distribution of the spherical powder is often more homogenous; however, the results suggested that the importance of local packing should not be overlooked in a HDH powder bed due to the larger local packing variation which can potentially

impair the part quality. By combining all the findings, two porosity formation mechanisms related to the non-spherical HDH powder were proposed as follows:

a. The coarser particle size and the lower number density of the HDH powder causes more severe fluctuation of laser energy absorption which destabilizes the melt pool/keyhole and induces porosity when the laser energy input is in the keyholing regime.
b. The low-packing spots in the HDH powder bed tend to form depressions on the top surface of a melt track due to lack of materials in melting. The depressed sites increase the thickness locally as the subsequent powder layer is deposited. They can impede the full laser penetration and lead to unfused voids akin to lack-of-fusion. The abundance of the low-packing spots proven by the Monte Carlo analysis and the already thicker powder layer, which is required to accommodate the large particle size, make the HDH powder bed more susceptible to this porosity formation mechanism.

Hypothesis 4.1. is supported by the results from the Monte Carlo image analysis as the HDH powder sample was the only one among all nine powders that showed a large population of low packing density spots. Potential modification will likely to be redefining the threshold for low packing fraction, i.e., 35 %. The modification can be made based on the comparison between the concentration and spatial distribution of the low packing density spots and those of the large pores in the as-built parts.

Hypothesis 4.2. is supported by the single-bead DXR experiments. At the same process condition, the keyhole fluctuation was significantly stronger with a HDH powder bed compared with a powder bed of spherical powder or a no powder specimen. Evidence of keyhole interruption caused by the HDH particles was presented in this chapter.

5. Printability of 17-4 PH Powders with High Porosity Contents in L-PBF

The chapter was adapted from the publication of D. Basu and Z. Wu *et al*., Entrapped Gas and Process Parameter-Induced Porosity Formation in Additively Manufactured 17-4 PH Stainless Steel published in Journal of Materials Engineering and Performance (2021).

5.1. Introduction

As discussed in section §1.4.2., 17-4 PH stainless steel is a standard L-PBF alloy, of which many aspects, e.g., printability and microstructure, have been well-studied. Hu *et al*. [127] and Gu *et al*. [93] have shown how porosity in 17-4 PH as-built parts varied as a function of energy density; however, this trend was not as informative as the process map, especially the P-V process map, in terms of providing guideline to select the optimal process parameters for minimizing defect concentration. Furthermore, no literature has shown how powder porosity systematically affects the final in-part porosity concentration in 17-4 PH steel. The chapter aims to identify the process windows for the 17-4 PH stainless steel powders with various levels of powder porosity content and to understand how entrapped gas porosity in powder affects the final in-part porosity by adapting the process map approach and utilizing the standard metallographic techniques.

The contents in Chapter 5 and Chapter 6 are closely related but have different foci, i.e., Chapter 5 discusses the printability of the 17-4 PH powders with high levels of powder porosity while Chapter 6 focuses on understanding the formation mechanism of powder entrapped gas induced porosity. At the time that the fabrication tasks were performed, the information derived from the synchrotron-based techniques were unknown, e.g., powder porosity concentration.

Since this information is helpful for the readers to understand the contents presented in Chapter 5, it will be partially shown in the current chapter while more details can be found in Chapter 6.

5.2. Hypothesis

Hypothesis 5.1. The as-built 17-4 PH parts can achieve 99.9% density at the optimal parameters even using the most porous powder available.

5.3. Methods

This study used four batches of 17-4 PH stainless steel powder with levels of entrapped gas that were intentionally varied, through powder production process modifications, to levels well exceeding typical gas-atomized powder. Note that lots Ar-1, Ar-2, and Ar-3 are argon atomized powder and lot N_2-1 is nitrogen atomized powder but using tailored raw material selection to keep the content of austenite stabilizing nitrogen to levels acceptable for argon atomized powder. As will be discussed in section §6.4.1., the powder porosity concentration follows the order of N_2-1 (0.006%) < Ar-1 (0.010%) < Ar-2 (0.067%) < Ar-3 (0.145%).

The four batches of powder were then used to additively manufacture solid specimens in an EOS M290 L-PBF process. To study the effects of powder gas entrapment and fabrication environment, four builds in the four different powders were manufactured in an argon environment while an additional build in N_2-1 powder was manufactured in a nitrogen environment using a nominal layer thickness of 40 μm. Each build contained 25 rectangular prisms with dimension of 15 (L) x 10 (W) x 10 (H) mm^3 where the laser power, laser scan velocity, and hatch spacing were systematically varied as shown in Table 5.1. Note that the parameter selection started with a commonly used baseline parameter set for 17-4 PH stainless steel which is 195 W and 750 mm/s.

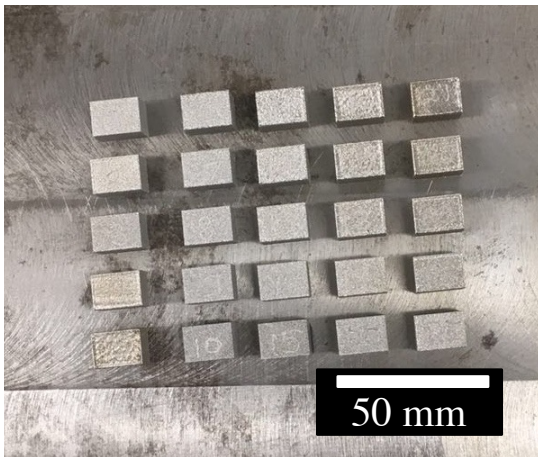

Figure 5.1 An example of fused 17-4 PH stainless steel specimens on an EOS M290 build plate after de-powdering. Note that sample location, spacing, and orientation were identical for all five builds.

Table 5.1 Process parameters used to build the specimens in the 17-4PH stainless steel powders.

Sample #	Scan velocity (mm/s)	Power (W)	Hatch spacing (μm)
6	1200	350	120
7	1200	300	120
8	1200	250	120
9	1200	200	120
10	1200	150	120
11	1000	350	120
12	1000	300	120
13	1000	250	120
14	1000	200	120
15	1000	150	120
16	800	350	120
17	800	300	120
18	800	250	120
19	750	195	120
20	800	150	120
21	600	350	120
22	600	300	120
23	600	250	120
24	600	200	120
25	600	150	120

The rectangular prisms were first cut along the build direction to show the 15 (L) x 10 (H) mm^2 cross-section using a wire EDM, and sequentially polished to remove the EDMed surface using silicon carbide papers, diamond paste, and colloidal silica. Cross-sectional images were then captured on a Leica DM750M optical microscope. These images were then fed into Fiji to perform segmentation, shape measurement, and size quantification on the porosity.

SEM helped to visualize the morphology of the powder particles, which were loosely deposited on an adhesive carbon tape attached to a SEM sample stub. High pressure air was blown to remove the excessive powder and minimize powder overlapping. Powder size was quantified using synchrotron-based µXCT and light scattering per ASTM B822 on a Microtrac S3500 in SRA150 mode.

5.4. Results & Discussions

5.4.1. 17-4 PH Stainless Steel Powders

As shown in Figure 5.2, most powder particles have spherical morphology while some of them have some minor satellites attached. A few irregularly shaped powder particles from incomplete atomization, typical of gas atomization and benign at these trace levels were also observed.

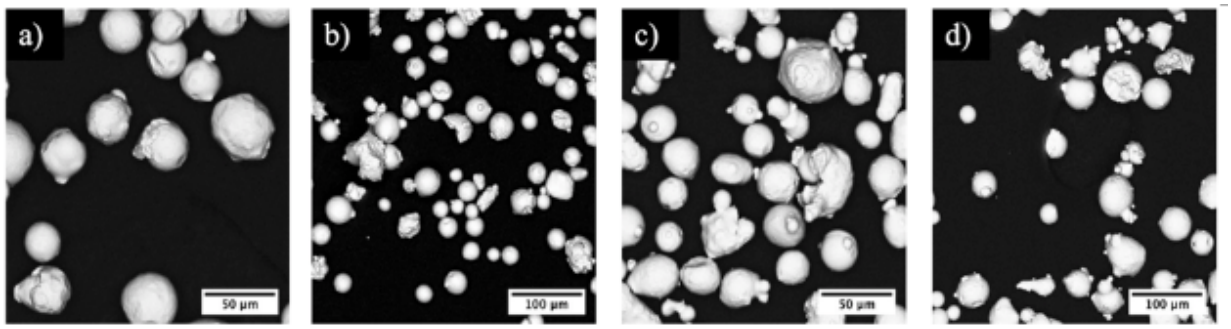

Figure 5.2 SEM micrographs of the a) N_2-1, b) Ar-1, c) Ar-2 and d) Ar-3 gas atomized 17-4 PH stainless steel powders.

Figure 5.3 shows the volume-weighted powder size distributions of the four 17-4 PH stainless steel powders from the μXCT and light scattering measurements. The analysis of the μXCT data used 8,252 (0.89 mg) N_2-1 particles, 7,609 (0.6 mg) Ar-1 particles, 3,096 (0.21 mg) Ar-2 particles, and 4,603 (0.43 mg) Ar-3 particles. By contrast, the light scattering method used a 3 to 4 orders of magnitude larger sample size. The four powders have similar size distributions with the majority of particles falling within the 20 – 40 μm range. As a comparison, the particle size distributions measured by laser diffraction are shown superimposed on the μXCT measurements in Figure 5.3. The D_{50}s and the relative/comparative order of size matched reasonably well between the measurements from the two techniques although the agreement was less good in the tails. The possible sources of error include limited resolution and sampling size in the μXCT, poorer sampling statistics in the tails, and breakdown of sphericity assumption with larger sizes in the laser diffraction data, i.e., highly non-spherical particle agglomerates being counted in the analysis.

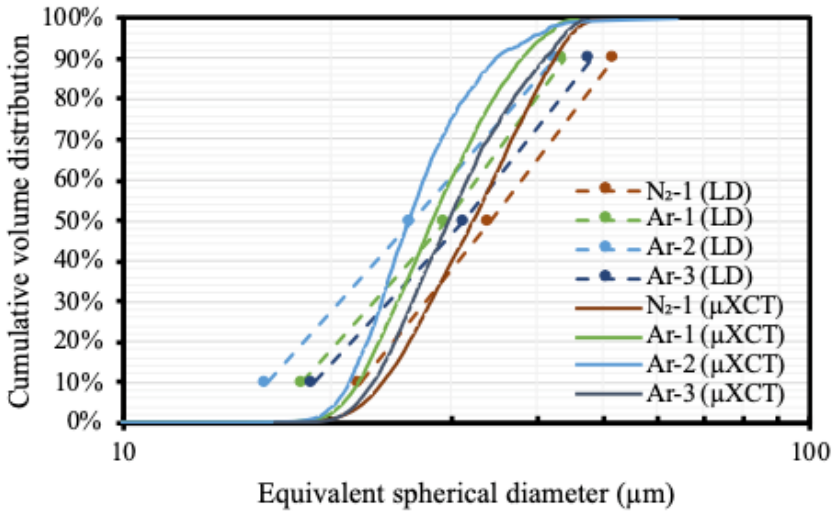

Figure 5.3 Volume-weighted powder size cumulative distributions of the four gas-atomized 17-4 PH stainless steel powders, N_2-1 (D_{50} = 32.4 μm), Ar-1 (D_{50} = 28.2 μm), Ar-2 (D_{50} = 26.0 μm), and Ar-3 (D_{50} = 29.8 μm), from the powder μXCT analysis. Note that a shape

threshold (anisotropy < 0.25) was applied to eliminate the non-spherical powder clusters that failed to be segmented by the 3D watershed algorithm in Avizo. As a comparison, particle size distributions for N_2-1 (D_{50} = 34.3 µm), Ar-1 (D_{50} = 29.6 µm), Ar-2 (D_{50} = 26.4 µm), and Ar-3 (D_{50} = 31.4 µm) measured by laser diffraction (LD) were each shown as three points connected by a dashed line.

5.4.2. Process Maps of L-PBF 17-4 PH Steel

The argon atomized powders were fused in an argon environment, and the nitrogen atomized powder was fused in both an argon environment and a nitrogen environment. As mentioned in section §5.3., the porosity of the rectangular prisms fabricated in the five builds was quantified by analyzing the metallographic cross-sections.

Figure 5.4 summarizes the porosity concentration at each laser scan power and velocity combination for all five builds at the nominal hatch spacing of 120 µm in P-V porosity maps. The porosity maps did not reveal the boundary between the keyhole regime and the process window since no significant increase on porosity was seen along with the increasing energy density, i.e., high power and low velocity parameters. On the other hand, the boundary between the process window and the lack-of-fusion zone can be easily identified from each map. Some parameters on the boundary yielded slightly higher porosity population than others. The usage of different powders could potentially shift the boundary's location and the corresponding porosity values. Additionally, depending on the powder selection, laser velocity up to 1200 mm/s can potentially be applied to accelerate the fabrication process. Of course, the balling phenomenon may be concerning if a high-power and high-velocity parameter set is used.

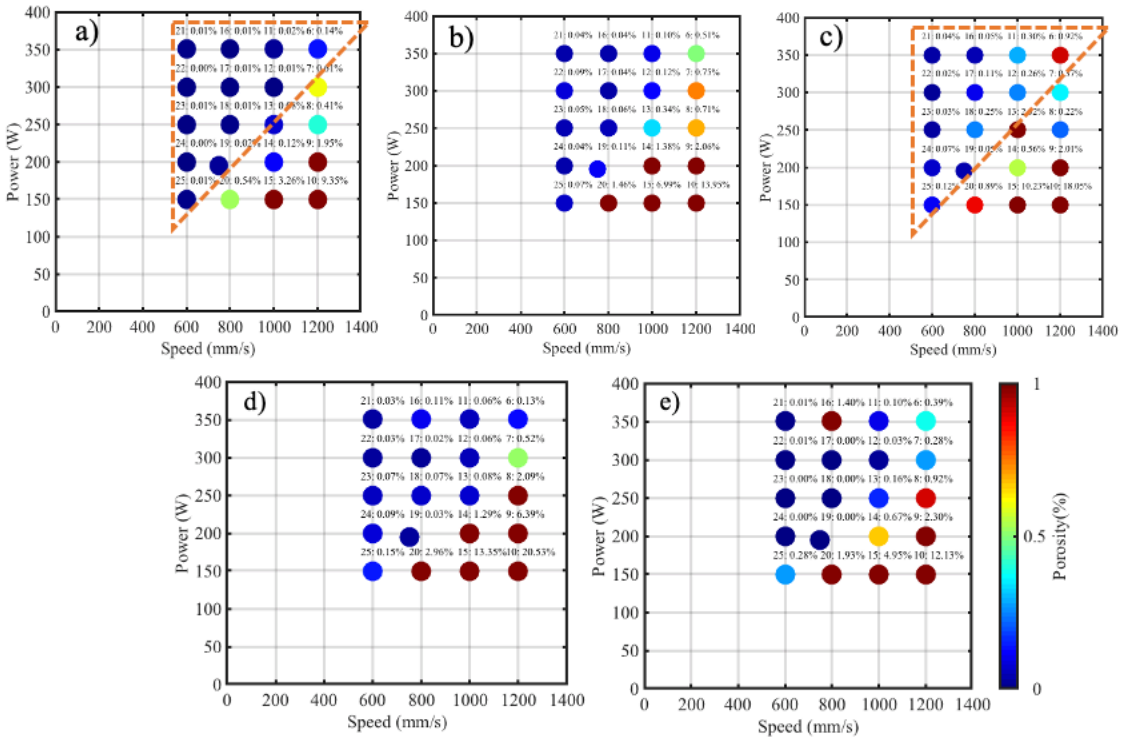

Figure 5.4 P-V porosity maps of the L-PBF 17-4 PH steel parts using a) – c) Ar-1, Ar-2, and Ar-3 atomized powder built in an argon environment, d) N_2-1 atomized powder built in an argon environment, and e) N_2-1 atomized powder built in a nitrogen environment.

Although the process windows for all five cases were similar, a general trend of the porosity values could be observed for parameters within the window among different powders. The parts from build using the more porous powders, e.g., Ar-3, have significantly higher porosity concentration compared with the parts from the build using the less porous powders, e.g., Ar-1 and N_2-1, in the highlighted P-V space of the porosity map. This trend implies that the effects from the powder porosity on the in-part porosity content is nontrivial. On the other hand, different parameters showed different sensitivities to powder entrapped gas induced porosity. To show how the sensitivity varies, Figure 5.5 shows the difference of the porosity value between

the Ar-1 and Ar-3 builds for each P-V combination within the process window against the energy density, which is also known as the volumetric power input [40].

$$Energy\ density = \frac{P}{VHL}$$

where P is the laser power, V is the laser velocity and H is the hatch spacing, and L is the layer thickness. The highlighted region in Figure 5.5 corresponds to the highlighted P-V space in the porosity maps, Figure 5.4. In this region of relatively lower energy densities, the parameters showed higher sensitivity to the powder porosity. Lower energy density means smaller melt pool size and less remelting which are unfavorable for the escape of pores since these characteristics limit the time that pores can travel in liquid metal. By contrast, the parameters at higher energy densities showed low sensitivity to the powder entrapped gas induced porosity.

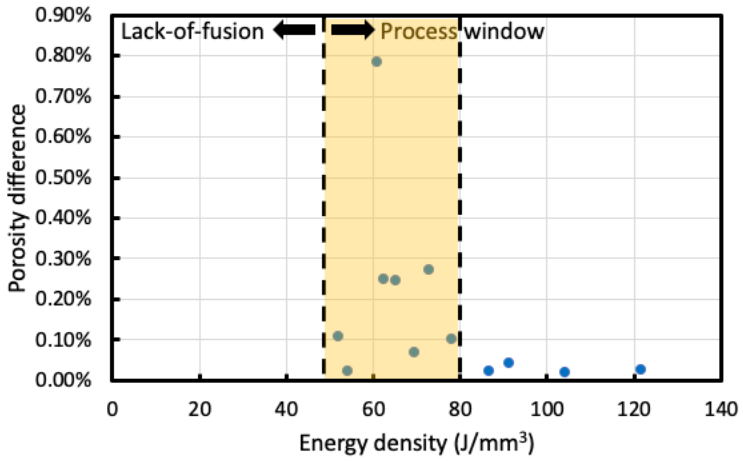

Figure 5.5 The difference of porosity values at each power-velocity combination within the process window between the Ar-1 and Ar-3 builds.

On the other hand, the porosity difference did not follow a strict trend as a function of energy density; instead, it showed higher variability, i.e., varied from 0.02 % to 0.78 %, in the highlighted region. To explain the variability, Figure 5.6 incorporated various sized markers to

represent the porosity difference and the melt pool shape into the analysis by adding another dimension, the aspect ratio of the melt pool derived from the Rosenthal analytical equation [97]:

$$\frac{L}{W} = \sqrt{\frac{\epsilon e Q V}{32\pi k \alpha (T_{melt} - T_{preheat})}}$$

where L is melt-pool length, W is melt-pool width, ϵ is laser absorptivity, Q is laser power, V is laser velocity, k is thermal conductivity, α is thermal diffusivity, T_{melt} is the melting temperature of the alloy, and $T_{preheat}$ is the preheat temperature of the built plate. At the lower energy densities, the parameters showed higher sensitivity to the powder porosity as the ratio increased. This implies that the shape of melt pool played a critical role in the escape of pores and a deeper and shorter melt pool promoted the escape under the premise of constant melt pool volume.

This observation motivated the author to use μXCT and DXR to visualize the porosity, particularly targeting those inherited from the powder entrapped gas in Chapter 6 and couple with the sensitivity analysis to understand the porosity formation mechanism and the effects from melt pool shape.

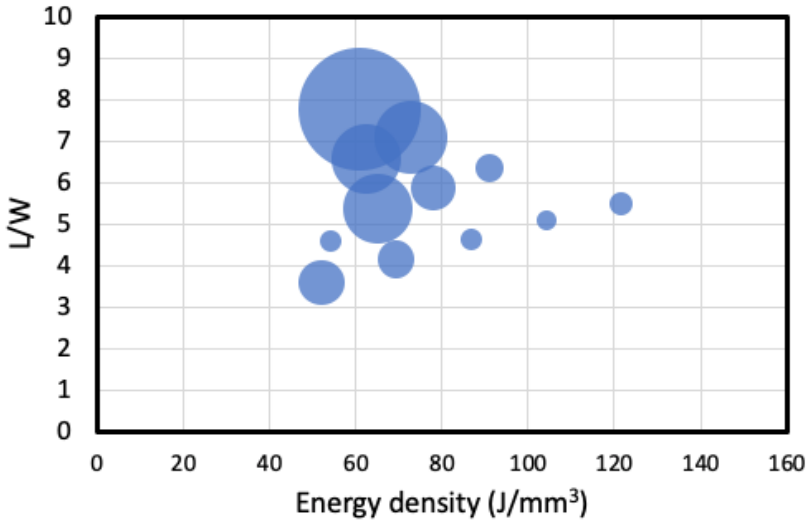

Figure 5.6 The difference in porosity values at each power-velocity combination within the process window between the Ar-1 and Ar-3 builds plotted against the melt-pool shape and the corresponding energy density.

5.5. Conclusions & Hypothesis Revisited

The chapter has developed the process window for fabricating 17-4 PH stainless steel in a L-PBF process. The maps revealed an observable trend and correlation between the powder porosity and the resulted in-part porosity. Different parameters, more specifically the resulted melt pool geometry, showed different sensitivities to powder entrapped gas induced porosity. This provides insights about how to mitigate the porosity problem in the future fabrication. *Hypothesis 5.1.* has been proven to be true. Even with 0.145 % porosity in the Ar-3 powder, the optimal range of parameters can result in < 0.01 % porosity.

6. Investigation of Powder Entrapped Gas Induced Porosity Formation

The chapter was adapted from the publication of Z. Wu and D. Basu *et al*., Study of Powder Gas Entrapment and Its Effects on Porosity in 17-4 PH Stainless Steel Parts Fabricated in Laser Powder Bed Fusion published in JOM (2020).

6.1. Introduction

The process maps of the 17-4 PH stainless steel in the previous chapter suggested that sufficient powder porosity has significant impact on the final in-part porosity by showing higher porosity concentrations for the power-velocity combinations within the process windows of the powders with higher porosity content. This chapter aims to quantitatively understand how the powder porosity evolve during/after laser melting.

As discussed in section §1.3.2., studies reported to use synchrotron-based μXCT to visualize powder entrapped gas related porosity in 3D and use DXR to *in-situ* monitor the metal-laser interaction and porosity formation. This chapter utilized DXR videos to understand the transfer process, i.e., from powder to bulk, and the coalescence process, i.e., from one liquid spatter to another, of the entrapped gas porosity during laser melting, and μXCT on the 17-4 PH steel powders and the L-PBF built 17-4 PH steel components with selected process parameters to quantify the size distribution, spatial distribution, and morphology of porosity. Furthermore, knowing the formation mechanism of the in-part porosity through *ex-situ* characterization methods has always been challenging, this chapter presents a novel way to better segment the powder entrapped gas induced porosity from others by using the shape descriptors derived from the μXCT analysis.

Building on the previous study [43], the current work uses a different alloy system, 17-4 PH stainless steel, and focuses on investigating entrapped gas porosity formation by intentionally

varying and increasing the population of entrapped gas in powder and controlling the particle size distribution to minimize its effect on porosity formation. The results from this work provide insights about the impact of the powder entrapped gas induced porosity and its formation.

6.2. Hypothesis

Hypothesis 6.1. The powder entrapped gas induced porosity can be better separated from the porosity caused by other mechanisms through shape analysis.

Hypothesis 6.2. Only the powder porosity entered the melt pool at the circulation domain will eventually be entrapped.

6.3. Methods

µXCT was performed at the 2-BM beamline of the APS at ANL. A pink beam illuminated the specimens with 0.024 s exposure. As an alternative to the monochromatic beam, the pink beam operated with a tunable grazing incident mirror instead of a monochromator to offer a broader x-ray bandwidth, i.e., higher flux; this enabled a faster data acquisition rate when the material has significant absorption due to the higher atomic number like the 17-4 PH stainless steel. Other µXCT settings and the details about the reconstruction and analysis process were given in section §2.2.1.

From each of the five builds shown in Chapter 5, this study selected the as-built specimen with the baseline parameter set, 750 mm/s laser scan speed, 195 W laser power and 120 µm hatch spacing, to demonstrate the effects solely from the powder feedstock. Table 6.1 lists the build parameters and the corresponding build environment of the as-built specimens characterized using µXCT. In addition to the as-built materials, samples were prepared of all powder feedstock lots. Samples from the 17-4 PH powders were packed in Kapton tubes with 1 mm inner diameter.

Table 6.1 The process parameters of the as-built specimens used in the μXCT characterization.

Powder Lot	Build environment	Speed (mm/s)	Power (W)	Hatch spacing (μm)	Layer thickness (μm)
N_2-1	N_2	750	195	120	40
N_2-1	Ar				
Ar-1	Ar				
Ar-2	Ar				
Ar-3	Ar				

Powder added single-bead melting experiments were performed at the 32-ID-B beamline of the APS at ANL and monitored using the high-speed x-ray imaging approach to study the transfer and coalescence phenomenon of the powder porosity. The detailed DXR setup was given in §2.2.3. Table 6.2 lists the parameter sets of samples where the two phenomena occurred during/after laser melting.

Table 6.2 The process parameters of the samples where the transference and coalescence phenomenon of the powder porosity occurred in the DXR experiments.

Powder Lot	Build environment	Speed (mm/s)	Power (W)
Ar-1	Ar	400	370
Ar-2	Ar		

6.4. Results & Discussions

6.4.1. Powder Porosity in the 17-4 PH Steel Powders

As mentioned before, powders used in this study have intentionally varied powder production parameters to introduce extreme variation in entrapped gas populations (beyond levels typically seen in gas-atomized powder for AM). Figure 6.1 shows that it is easy to observe qualitatively that powder Ar-2 and Ar-3 have much higher entrapped gas content compared with

Ar-1 and N_2-1. If only counting the more spherical (anisotropy < 0.6) pores, the relative densities of Ar-1, Ar-2, Ar-3, and N_2-1 powders are 99.990 %, 99.933 %, 99.855 %, and 99.994 %, respectively. The number density and the volume density of the powder entrapped gas pores follow the same increasing order of N_2-1 < Ar-1 < Ar-2 < Ar-3 in most of the size bins, see Figure 6.2. The volume density can better represent the size distribution of entrapped gas, Figure 6.2b, because it weighed more on the entrapped gas pores with larger volume which, if transferred to the final part, would be potentially more deleterious to the mechanical properties. A minimum diameter threshold of 4 µm on pore size was applied to all the datasets to avoid artifacts from the reconstruction since the smaller features approach the resolution (0.69 µm/pixel); this can explain the low porosity density seen in the first interval of Figure 6.2.

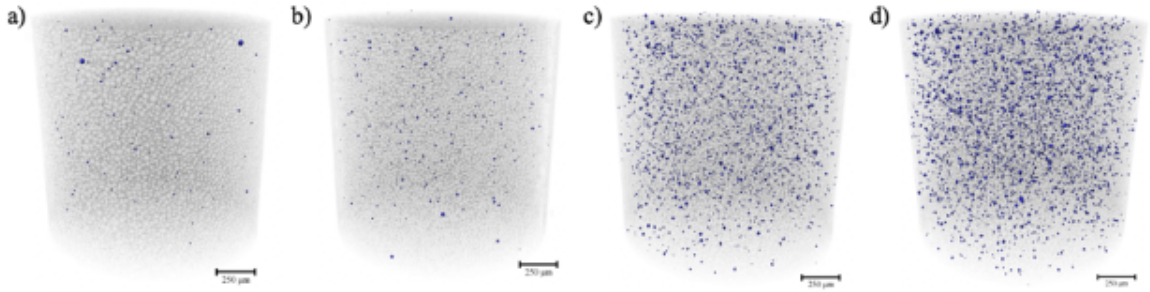

Figure 6.1 µXCT reconstructions of the gas-atomized 17-4 PH stainless steel powders, a) N_2-1, b) Ar-1, c) Ar-2, and d) Ar-3, with the entrapped gas pores highlighted in blue. Note that a shape threshold (anisotropy < 0.6) was applied to eliminate the artifacts from the µXCT reconstructions.

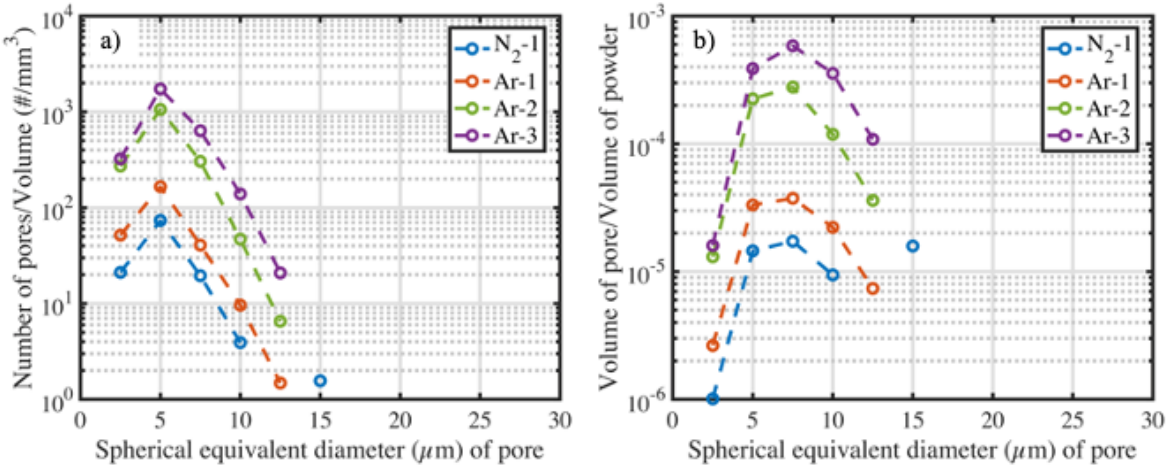

Figure 6.2 For pores of anisotropy < 0.6, a) number density (total number of pores of a given spherical equivalent diameter bin / total powder sample volume) and b) volume density (total volume of all pores of a given spherical equivalent diameter bin / total powder sample volume) of the powder porosity was calculated from the four reconstructed µXCT datasets.

6.4.2. Segment Entrapped Gas Induced Porosity using Shape Descriptors

Porosity in the as-built parts resulted from various mechanisms even if the building conditions have been optimized. With that said, distinguishing the pores inherited from powder feedstock from the pores introduced by other mechanisms can be challenging. A reasonable approach to separate pores by the formation mechanism is to examine the pore morphology, specifically anisotropy, which was described in section §2.2.2.

A previous study [43] used an arbitrary cut-off anisotropy value to perform the separation task. Strictly controlling powder size and build conditions ensured that the as-built porosity was a function of the build environment and entrapped gas population. As such, comparing multiple anisotropy distributions could inform the selection of this threshold. Figure 6.3a summarizes the anisotropy distributions of the in-part porosity corresponding to the five as-built specimens fabricated using the baseline parameters in Table 6.1 and Figure 6.3b provides a magnified view

for the three cases with relatively lower counts of in-part porosity. The fundamental assumption of utilizing a shape descriptor to identify the entrapped gas porosity is that the more spherical in-part pores were likely to have been inherited from powder entrapped gas porosity as a result of surface tension in liquid state while the irregularly shaped pores were more likely to have originated from fabrication, e.g., local lack-of-fusion and end-of-track porosity. This implies that the anisotropy distributions in the five different cases with the same process parameters should converge, i.e., no statistical significance, near the upper tail regardless the population of the entrapped gas porosity in the powders, and the difference in the low anisotropy intervals should be predominantly caused by powder entrapped gas. Since the true formation mechanism of each pore was unknown and many mechanisms could also result in spherical porosity, it is important to acknowledge that using a single cut-off value of anisotropy will certainly misclassify some pores, i.e., more porosity introduced by other mechanisms will be involved in the analysis if a larger cut-off value is selected.

As shown by Figure 6.1, N_2-1 has the lowest population of entrapped gas among the four powders making such porosity in the as-built part improbable. Due to the high solubility in 17-4 PH stainless steel [42], building N_2-1 in a nitrogen environment potentially further reduced the spherical porosity compared with building in argon, see Figure 6.3b. A significant drop in the anisotropy distribution of N_2-1 in nitrogen suggests that a cut-off value between 0.5 and 0.6 is reasonable. The slightly higher powder entrapped gas in Ar-1 resulted in a bimodal distribution, Figure 6.3b, where the intersection of the two peaks suggests a similar range for the threshold selection. Figure 6.3a incorporated the distributions of Ar-2 and Ar-3 with much higher porosity count due to the higher powder entrapped gas contents. It is much easier to observe the

aforementioned convergence at the high anisotropy intervals (anisotropy > 0.7) where most of the pores are considered to be induced by other mechanisms during fabrication.

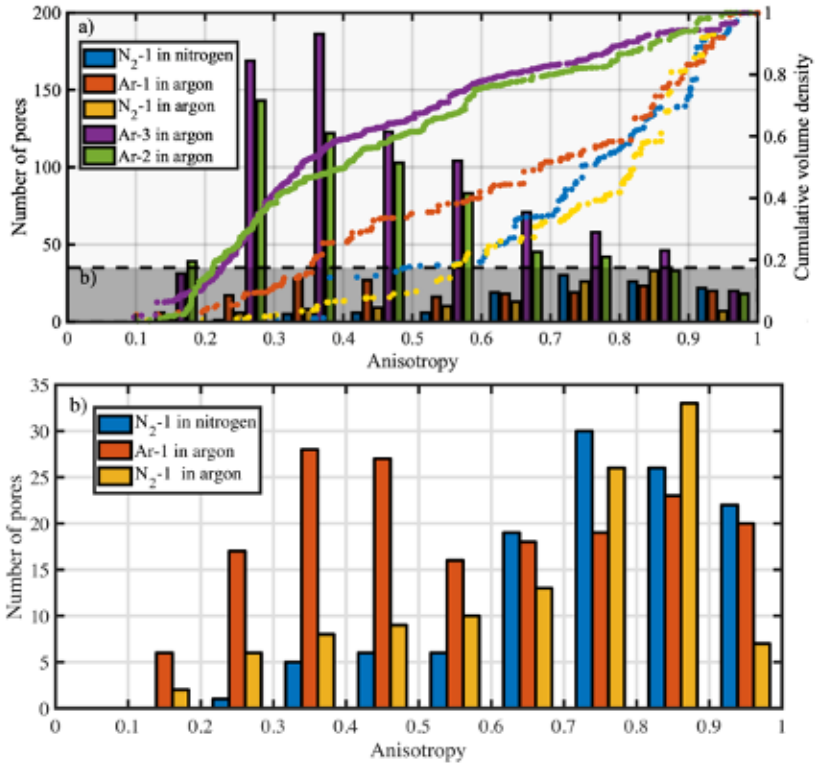

Figure 6.3 Distributions of the calculated anisotropy of pores in the as-built parts from the four 17-4 PH stainless steel powders using the baseline parameters, Table 6.1, in a nitrogen or an argon environment. Note that b) is a magnified view of a) highlighting the distributions with relatively lower pore counts. The histogram in a) represents the number of pores (left y axis) while the curve in a) represents the cumulative volume density (right y axis) normalized by the total porosity volume in the corresponding as-built specimen.

Figure 6.4a shows the cumulative volume distribution of the porosity normalized by the solid volume of the as-built part. At an anisotropy value of 0.38, the N_2-1 printed in nitrogen curve has a spike which is contributed by a pore with diameter of 45 µm. This pore is not likely induced by powder entrapped gas since its diameter is larger than 99 % of the powder particles.

The modified N_2-1 in nitrogen curve in Figure 6.4a represents the distribution after removing the single outlier pore. Because of the low powder entrapped gas in N_2-1, it is reasonable to assume that the porosity in the as-built N_2-1 parts was primarily from fabrication. Thus, the modified N_2-1 in nitrogen curve, Figure 6.4a, was subtracted from each distribution to deconvolute the in-part porosity content contributed from the build environment (N_2-1 in argon) and from the increasing powder entrapped gas content in Figure 6.4b. After subtraction, a deflection point at an anisotropy value of 0.6 appeared on each curve where the difference in each case continued to increase until 0.6 and became statistically insignificant after 0.6. The slight decrease in Figure 6.4b of > 0.7 anisotropy pore volumes, relative to N_2-1 in nitrogen and N_2-1 in argon, suggests that some of the < 0.7 anisotropy pores are due to the interactions of the entrapped gas pores combining with the processing related porosity to form the less anisotropic process related porosity.

In summary, a cut-off value between 0.5 and 0.7 is reasonable; this study uses anisotropy < 0.6 to separate the entrapped gas induced porosity from the processing related porosity. The morphology threshold was applied to the powder entrapped gas analysis and the later analysis on in-part defects to ensure the comparison is unbiased. It is important to acknowledge that selecting 0.6 as the threshold for entrapped gas in powder is somewhat arbitrary, since L-PBF and atomization may have very different porosity formation conditions, e.g., pressures, shear flow, cooling rates and surface tension effects. Since the primary goal of applying a threshold on the data of entrapped gas in powder is to minimize the artifacts from the segmentation process, while maintaining the consistency of the in-part porosity analysis, the threshold's effect on quantitative powder porosity measurements is of secondary importance. However, sensitivity analysis was performed to ensure that the qualitative relationships, i.e., entrapped gas content

and powder size, between powder lots were unaffected by this threshold selection for the powder samples.

In terms of the overall porosity, the two N_2-1 cases in Figure 6.4a show no significant difference even though the nitrogen building environment was expected to exhibit a reduced frequency of processing defect due to the higher solubility, relative to argon, of nitrogen in 17-4 PH stainless steel. Similarly, using Ar-1 with a moderate powder entrapped gas content resulted in indistinguishable in-part porosity levels from the nitrogen atomized powder builds. This suggests that, compared with the variability from fabrication and characterization, powder entrapped gas porosity is a secondary effect unless an atypically high level of powder entrapped gas is introduced as with Ar-2 and Ar-3. The cumulative volume densities in Figure 6.3a show that the in-part porosity induced by powder entrapped gas could vary from 0.2 to 0.8, which dominates the overall porosity volume, if the cut-off anisotropy is 0.6. That said, powder entrapped gas has minor effects on the total in-part porosity if its content in powder is < 0.01 % but can be detrimental if its population is not well-controlled in powder.

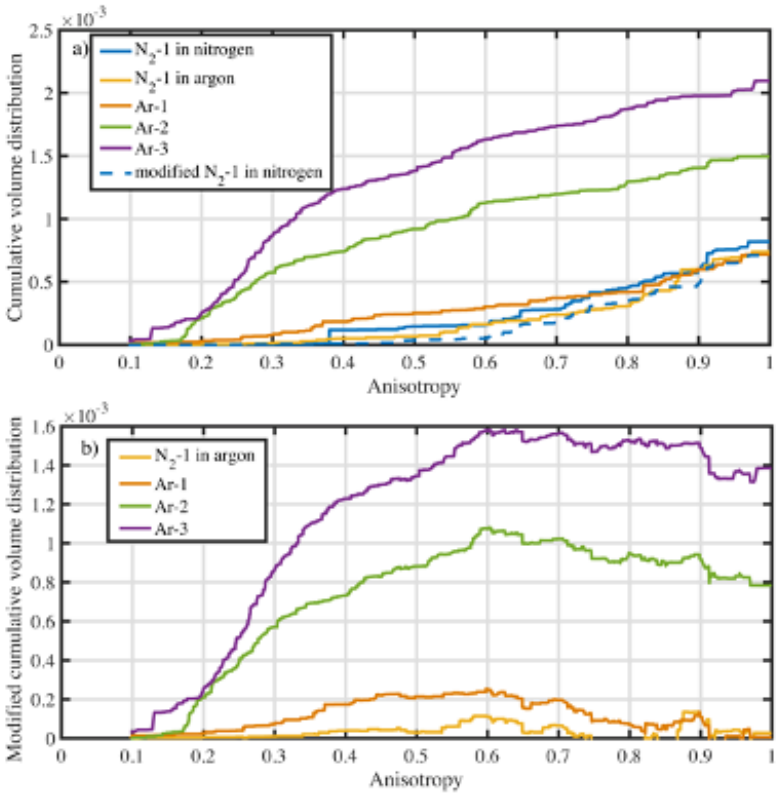

Figure 6.4 Cumulative porosity volume distributions normalized by the total volume of the corresponding as-built specimens in Figure 6.5. Note that b) shows the modified cumulative volume distributions as the modified N_2-1 in nitrogen curve in a) was subtracted from each curve in b) across the whole anisotropy range to highlight the deflection point.

6.4.3. Entrapped Gas Induced Porosity in the L-PBF 17-4 PH Steel Parts

Figure 6.5 reveals the spatial distribution of the porosity in the as-built specimens using the baseline parameter set from all five fabrication tasks, see Table 6.1. The overall part densities of the as-built components, Figure 6.5a-e, are 99.92 %, 99.93 %, 99.93 %, 99.85 %, and 99.79 %, respectively. Considering that the bulk mechanical properties are less sensitive to the smaller defects, a minimum diameter threshold of 4 µm on pore size was applied to the datasets to avoid the artifacts from the reconstruction and data acquisition. The fact that the powder particles falling in the range between 15 and 40 µm dominated the population makes the

clustering of entrapped gas induced porosity around 5 – 10 µm in size distribution expected due to the upper size limit set by the powder size. The 3D reconstructed µXCT data gives an impression of high porosity concentration; yet, all the specimens shown in Figure 6.5 have at least 99.79 % solid fraction. Dramatically different number densities of the entrapped gas porosity (anisotropy < 0.6) between fabrication tasks are shown in Figure 6.6 following the same relative order as the entrapped gas porosity in the powders shown in Figure 6.2, N_2-1 (N_2) ≈ N_2-1 (Ar) < Ar-1 (Ar) < Ar-2 (Ar) < Ar-3 (Ar). This observance indicates a strong correlation between the population of the entrapped gas in the powders and the resulted porosity in the as-built parts. A decrease in the number and volume density of the entrapped gas in the powders, Figure 6.2, to the distribution of the spherical porosity in the as-built parts, Figure 6.6, suggests that the entrapped gas in the powders was not fully transferred into the as-built parts. The transfer rate is difficult to quantify since it varies across pore size; for example, a larger pore is more likely to be a process induced defect which mistakenly increases the transfer fraction estimation at the larger end of the distribution. Based on the populations of the entrapped gas porosity between 5 and 15 µm of the Ar-2 and Ar-3 cases in Figure 6.2 and Figure 6.6, the average transfer rate is around 30%. Lastly, N_2-1 in argon displays higher number and volume density over N_2-1 in nitrogen for most pore sizes, Figure 6.6, the well-known high solubility of N_2 in stainless steel may be responsible for this phenomenon by dissolving the entrapped N_2 into the matrix.

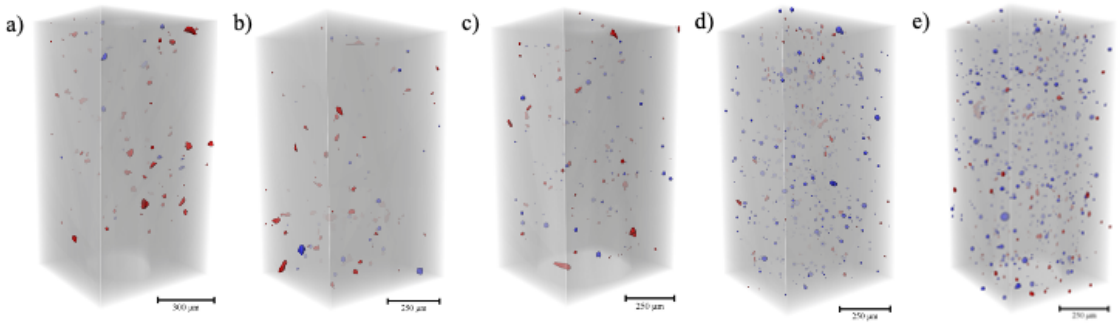

Figure 6.5 µXCT reconstructions of the AM specimens fabricated using the baseline parameters (750 mm/s, 195 W, 120 µm hatch spacing) from a) N_2-1 in a nitrogen building environment, and b) N_2-1, c) Ar-1, d) Ar-2, and e) Ar-3 in an argon building environment. Note that the more spherical pores (anisotropy < 0.6) are highlighted in blue, and the irregularly shaped pores (anisotropy > 0.6) are highlighted in red.

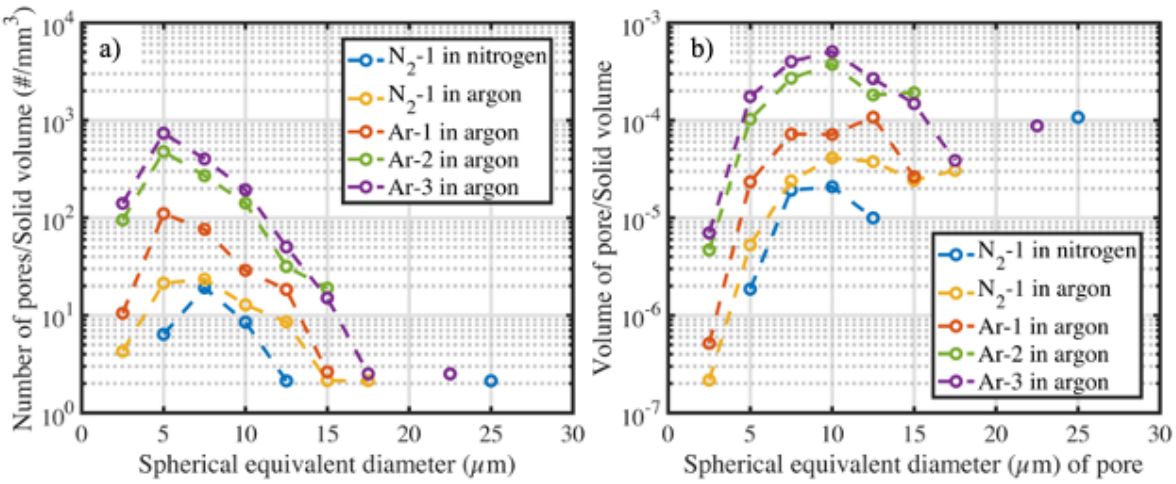

Figure 6.6 a) Number and b) volume density of porosity (anisotropy < 0.6) in the as-built parts fabricated in five different tasks using the baseline parameter set – 750 mm/s, 195 W and 120 µm hatch spacing.

6.4.4. Visualize Porosity Formation using DXR

Although the µXCT porosity results showed a strong correlation between the populations of the entrapped gas in the powders and the spherical porosity in the as-built parts, the porosity formation mechanism is more clearly established if the actual porosity transfer process is directly observed. Thanks to the high temporal and spatial resolution offered by DXR, the evolution of the in-part spherical porosity can be traced back to the entrapped gas in powder. Figure 6.7 shows an example of the porosity transfer that occurred within a 500 µs time span. The two

traced particles fell into the melt pool and transferred their entrapped gas pores into the base plate 460 μs after the laser scanned over them and this moment is labeled as t_0, Figure 6.7a. Whether the powder entrapped gas pore survived into the as-built part depended on the initial entry location with respect to the melt pool; one pore was entrapped by the solidification front while the other escaped with a much longer traveling path before leaving the liquid near the vapor cavity. The two different porosity evolutions match with the pore elimination mechanism proposed by Hojjatzadeh *et al*. [65]. They divided a melt pool into three domains where the laser interaction domain near the vapor cavity is dominated by the thermocapillary force promoting the escape of porosity. The fluid flow induced drag force controls the circulation domain near the tail of the melt pool suppressing the escape. That being said, the entry location strongly affects whether a powder entrapped gas pore can escape from the melt pool. During laser scanning, many powder particles were wetted into the melt pool with a short time delay, as shown in Figure 6.7, instead of being directly melted by the laser. As a result, the entrapped gas porosity enters the gentler circulation domain where is hypothesized that most of the powder entrapped gas pores get successfully inherited.

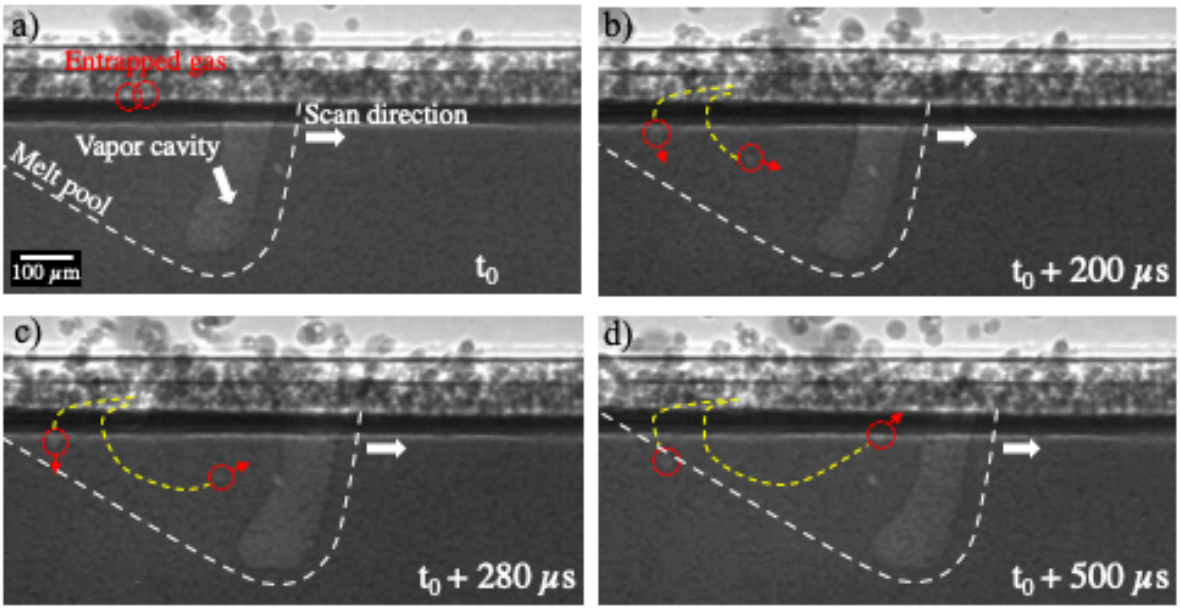

Figure 6.7 Individual frames from a DXR video that show the transference process of two entrapped gas pores from the powder particles into the base plate in an experiment using 370 W laser power and 400 mm/s laser speed. Note that the traced pores are highlighted by red circles and the traced paths are highlighted with yellow dashed lines.

Figure 6.8 shows an example of how powder porosity transfers from one particle to another. This phenomenon exists in AM fabrication and partially demonstrates what can happen in the atomization process. After being melted by the laser, the larger liquid droplet in Figure 6.8 wobbled through several cycles but quickly stabilized as a sphere due to surface tension. Meanwhile, a smaller liquid droplet with an entrapped gas pore spattered by the laser impinged on the larger droplet and merged with it. It is more difficult for pores to escape from a liquid droplet in comparison to a melt pool because of the absence of thermal gradient induced thermocapillary force and fluid flow induce drag force. As a result, the powder entrapped gas was not eliminated during the coalescence process but instead redistributed to different locations on the build plate along with the spatter.

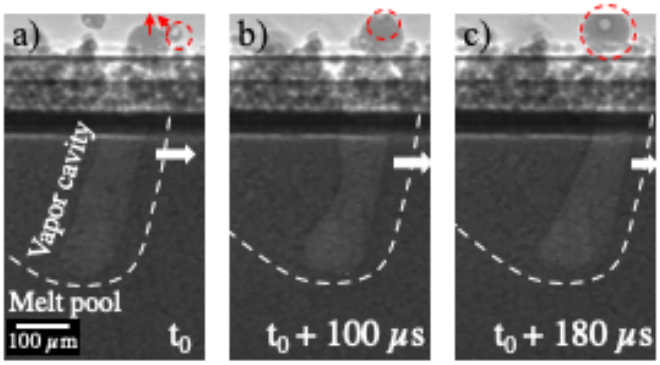

Figure 6.8 Frames from a DXR video show the coalescence process of an entrapped gas pore from one liquid droplet to another in an experiment using 370 W laser power and 400 mm/s laser speed. The traced pores are highlighted by red circles.

6.5. Conclusions & Hypothesis Revisited

This study utilized synchrotron-based μXCT and DXR to investigate the transfer of powder entrapped gas porosity by using the 17-4 PH stainless steel powders with a controlled size distribution and various populations of entrapped gas porosity and the corresponding as-built L-PBF parts. The main findings are as follows:

1. While the low entrapped gas content powder showed no net part porosity increase, the results showed a strong correlation between porosity in powder and in the corresponding as-built parts when utilizing powder with entrapped gas contents well above the level typical of gas atomized powder. This suggests it is an insignificant porosity type in L-PBF processes for typical gas atomized powders but that at some, to-be-established threshold (between Ar-1 and Ar-2) it becomes significant.
2. With intentionally introduced powder entrapped gas, the entrapped gas porosity can dominate (80 % of the total) the porosity volume density in the as-built parts.
3. The transferred fraction of the entrapped gas porosity from powder to as-built part is about 30 %.
4. Based on the analysis of pore size and shape, an anisotropy factor of 0.6 is a reasonable threshold value to separate the porosity induced by entrapped gas (≤ 0.6) from the process induced defects (> 0.6). *Hypothesis 6.1*. is supported by this finding. In the shape analysis, the results revealed the unique signature left by the formation mechanism on the resulted pores' morphology enabling the better separation of the entrapped gas induced porosity.

5. Examples of the transfer of pores, i.e., from powder to bulk, and coalescence process, i.e., from one semi-solid powder particle to another, of entrapped gas during laser melting were directly observed using DXR.
6. DXR documented powder entrapped gas, introduced into the circulation domain near the tail of a melt pool, and being unable to escape from the melt pool. This evidence supports *hypothesis 6.2*. that this domain is as a major region where entrapped gas porosity is inherited.

7. Fatigue of L-PBF HDH Ti-6Al-4V

The fatigue testing was performed at the Thermal Processing Technology Center at Illinois Institute of Technology by Professor Amir Mostafaei and Mohammadreza Asherloo. The author is grateful for the collaboration and the information sharing which signify an important contribution to this thesis document and the completion of the story about the process-microstructure-property relationship of the HDH AM components.

7.1. Introduction

Metal fatigue has been a persistent headache for the engineering world, and it occurs along with cyclic loading. Unlike immediate failure, the origin of metal fatigue is often hidden from non-destructive test procedures and the consequence is often catastrophic. Metal fatigue caused the disasters of the first commercial jet airliner, Comet, which permanently changed the window design in the modern aircraft.

From the materials perspective, fatigue life is strongly influenced by 1) internal defects, 2) surface roughness, 3) microstructure, and 4) residual stress. AM process parameters, post-processing heat treatments and surface treatments can result in a wide range of fatigue measurements by altering the four conditions that a testing coupon possesses. As shown by Pegues *et al*. [128], even the different dimensions of fatigue testing coupons could result in variations in fatigue property due to the different surface areas and the populations of the internal defects.

Metal fatigue involves in three stages, 1) fatigue crack initiation, 2) crack propagation, and 3) final rupture due to overload. Among the three stages, crack initiation takes significantly longer time compared with the others; this makes monitoring fatigue failure extra difficult. Thus, unlike those tests with high strain rate, fatigue is more sensitive to the larger outliners of

internal/surface defects, which exceed the critical flaw size, and their corresponding spatial distribution. The primary focus of this chapter is to evaluate the role of internal defects in fatigue crack initiation in the L-PBF built HDH components through careful comparison of fatigue lives and examination of fracture surfaces.

7.2. Hypothesis

Hypothesis 7.1. The fatigue life of the L-PBF as-built HDH Ti-6Al-4V parts is comparable (> 90 %) to the performance of the standard AM/wrought Ti-6Al-4V parts.

Hypothesis 7.2. After HIPing, the fatigue life of the L-PBF HDH Ti-6Al-4V parts can match (100 %) the performance of the standard AM/wrought Ti-6Al-4V parts.

7.3. Methods

The round fatigue specimens were built in the EOS M290 L-PBF process using an optimal process parameter set which was laser velocity of 1250 mm/s, laser power of 340 W and hatch spacing of 90 µm. The fatigue coupons (without pre-crack) shared the same dimensions (Figure 7.1) as the design reported by Pegues *et al*. [128] for the purpose of consistency. As shown in Figure 7.1, supporting fins were incorporated in line with the powder spreading direction to prevent sample distortion due to potential impacts with the recoater blade. Prior to sample removal from the build plate using a wire EDM, stress relief treatment was performed at 650 °C for 3 hours in an argon filled furnace. The fatigue testing was performed using a MTS 880 load frame at frequency of 30 Hz and R of -1.

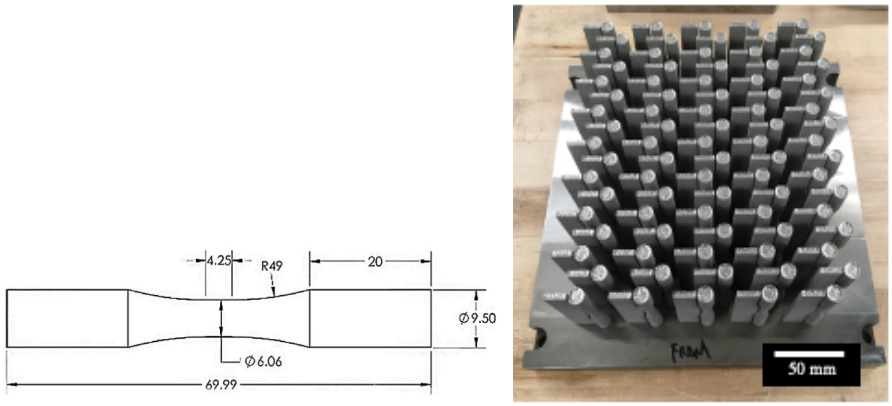

Figure 7.1 A schematic showing the dimensions of the HDH fatigue coupons adapted from Pegues et al. [128] *and an image of the as-built fatigue coupons on the build plate. Note that the dimensions of schematic are in millimeters.*

Upon failure, fracture surfaces were analyzed using a TESCAN MIRA3 FEG SEM. The surface roughness of the fatigue specimens was characterized using a Keyence VR-5200 white light scanner with 40x magnification at high resolution mode which offered measurement accuracy of ±2.5 µm in height and ±2 µm in width. Profile correction was applied during data post-processing to remove the curvature of the round fatigue specimens.

7.4. Results & Discussions

7.4.1. Fatigue Life after Stress Relief

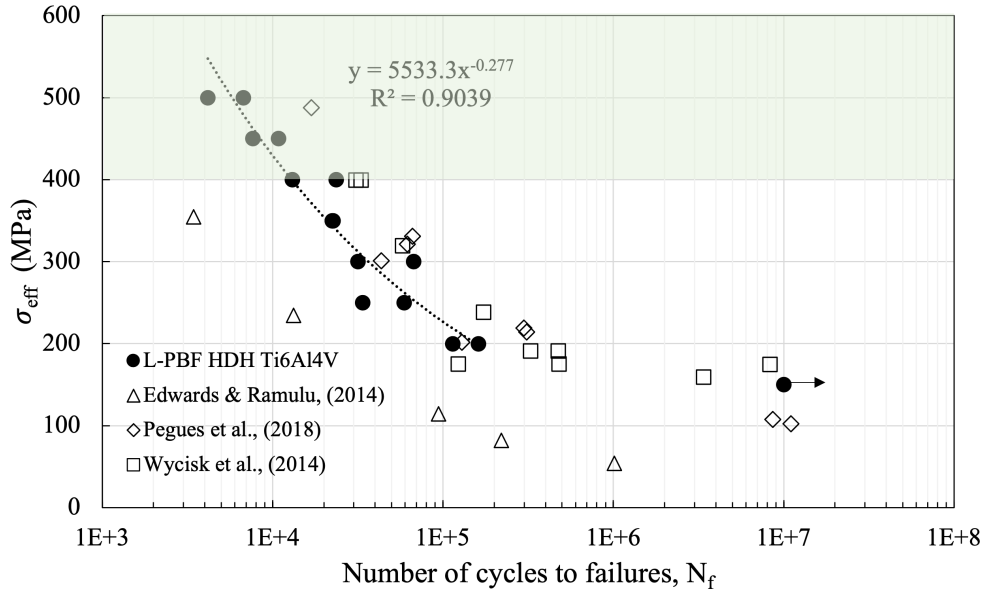

Figure 7.2 A Wöhler diagram comparing the uniaxial fatigue performance of the L-PBF built HDH TI-6Al-4V with other additively built Ti-6Al-4V from the literature [128–130] *at various stress levels. Note that the green area highlights the common stress levels for the endurance limits of wrought/cast Ti-6Al-4V* [131].

The Wöhler diagram in Figure 7.2 shows the S-N curve of the L-PBF built Ti-6Al-4V tested at stress levels from 150 MPa to 500 MPa with 50 MPa increments. Despite being the workhorse alloy and the abundance of Ti-6Al-4V fatigue data in the literature, fatigue results tested at similar sample conditions and testing conditions were limited to ensure a more straightforward comparison between the fatigue results obtained in tests with different R values. The maximum applied stress σ_{max} was normalized as the effective stress σ_{eff} as follows

$$\sigma_{eff} = \sigma_{max}\left(\frac{1-R}{2}\right)^{0.28}$$

where the exponent value 0.28 was validated by data from MMPDS-05 [131] for traditionally processed Ti-6Al-4V testing with R from -0.5 to 0.5.

The references used for the comparison were all L-PBF built Ti-6Al-4V with an as-built surface condition; however, the as-built surface roughness could depend on the laser parameters, especially the contour parameters, which were not reported in many of the studies. Edwards & Ramulu [129] tested their specimen at the as-built condition without stress relief treatment. Wycisk *et al*. [130] and Pegues *et al*. [128] stress relieved their specimens at 650 °C for 3 hours and 700 °C for 1 hour, respectively.

The scattering of results at various stress levels was relatively small as the best fit line showed reasonable logarithmic dependence of the cycles-to-failure on the applied cyclic stress. This suggests that the L-PBF process can fabricate components using the non-spherical powder with a consistent quality. The endurance limit of the HDH coupons appeared to be around 150 MPa or better as the fatigue specimen showed no sign of rupture after 10^7 loading cycles. The limit fell between the ones reported by Wycisk *et al*. [130] and Pegues *et al*. [128]. Despite showing comparable endurance limit as the standard AM counterparts, the cast/wrought Ti-6Al-4V components can withstand much higher stress levels by a significant margin. As highlighted by the green area in Figure 7.2, the endurance limits of the traditionally manufactured Ti-6Al-4V components are usually above 400 MPa. Hot working promotes defect reduction and dynamic recrystallization. With proper heat treatments, the cast/wrought Ti-6Al-4V can develop a fine globular α + β microstructure, which is much closer to equilibrium and has superior ductility compared with microstructures consisting of primarily α’ martensite. Finer α laths can also result in better resistance to localization of plastic slip and in turn mitigate crack initiation.

At higher stress levels, the HDH Ti-6Al-4V again displayed similar fatigue performance as the stress relieved standard AM Ti-6Al-4V reported by Wycisk *et al*. [130] and Pegues *et al*. [128]. Interestingly, the standard Ti-6Al-4V in the study of Edwards & Ramulu [129] was significantly weaker. The deviation could be a result of the influences from the different residual stress and porosity levels combined. We noticed that they used laser parameters with energy density above 110 J/mm^3 which would have resulted in the formation of keyhole porosity. Additionally, specimens without stress relief treatment could accumulate tension near the surfaces where fatigue cracks could initiate more easily.

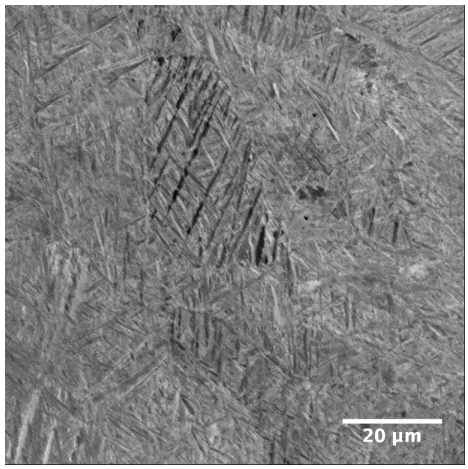

Figure 7.3 SEM image of the L-PBF built HDH Ti-6Al-4V after stress relief heat treatment.

The stress relief heat treatment at 650 °C for 3 hours seems to reduce the residual stress while preserving the martensitic microstructure as the HDH fatigue coupons displayed fine needle like α’ laths in Figure 7.3. Similar microstructure has been reported in the studies used for comparison.

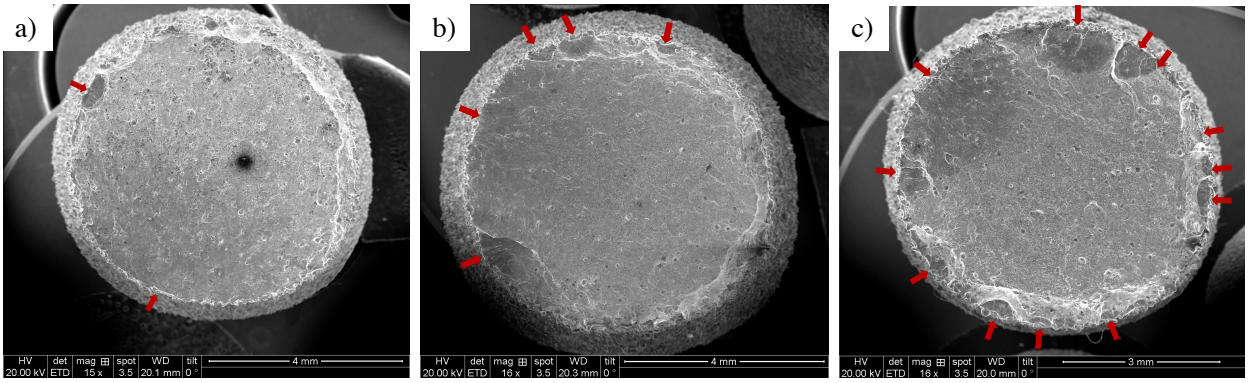

Figure 7.4 Fracture surfaces of the L-PBF built HDH Ti-6Al-4V fatigue coupons (after stress relief treatment) tested at a) 200 MPa, b) 300 MPa, and c) 400 MPa. Note that the red arrows highlighted the crack initiation sites.

Figure 7.4 shows the crack initiation zone, the crack propagation zone, and the final-stage overload zone on the fracture surfaces of the HDH Ti-6Al-4V coupons. On the fracture surfaces, the slightly darker areas are the indications of fatigue crack initiation and propagation. The red arrows highlighted the crack initiation sites. All cracks were initiated from surface defects despite many counts of pores found near/away from the surface. From left to right in Figure 7.4, the number of cracks initiated increased with the increasing nominal stress from 200 MPa to 400 MPa. This is a classical textbook example of larger applied stress increasing the number of initiation points [132].

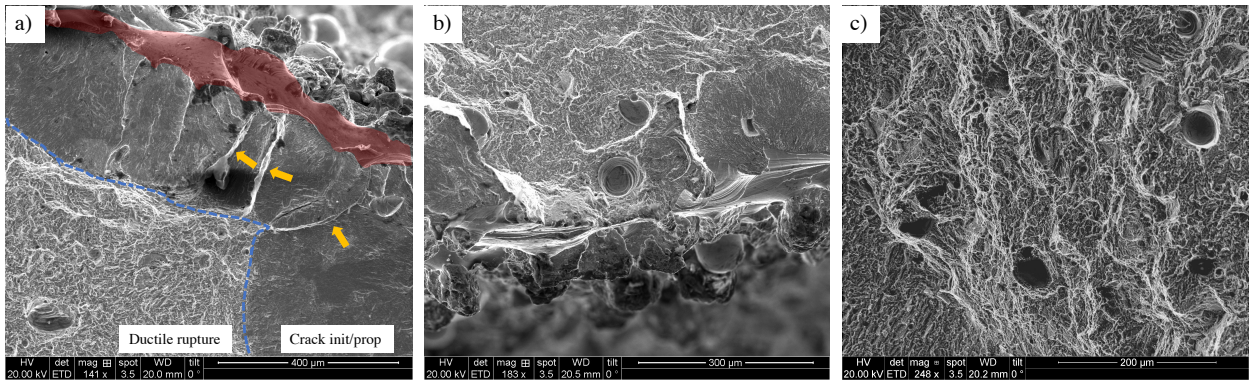

Figure 7.5 Examples of a) multiple fatigue cracks initiated from surface defects, b) near-surface pores, and c) internal pores within the overload rupture zone from the facture surfaces of the stress relieved L-PBF built HDH Ti-6Al-4V fatigue coupons.

From all the characterized facture surfaces, no pore was observed to contribute to the fatigue crack initiation. Figure 7.5c shows that most pores were surrounded by ductile fracture dimples within the rupture overload zone. Even from some pores located near the rough surface, as shown in Figure 7.5b, no evidence of crack initiation was found. The spherical pores were easy to identify as their internal walls preserved the as-melted surface texture. The pores are small (< 50 μm) which match with the μXCT measurements discussed in the previous chapter.

In contrast to the internal pores, surface defects were the culprit for crack initiation. Figure 7.5a shows that multiple cracks initiated from surface defects. The ratchet lines highlighted by the yellow arrows indicate the interactions between cracks initiated at different crystallographic planes. Since these cracks were not responsible for the final rupture of the specimen, a ductile fracture zone with dimple pattern quickly emerged at a few hundred micrometers away from the sample surface when the rupture occurred. The crack-initiated surface features were the deep valleys as highlighted by the red area. Kantzos *et al*. [133] suggested that the deep surface valleys and the near-surface pores are stress concentration sites; by contrast, the partially melted particles are often not load-bearing features but only contribute to the surface roughness. Above the surface valleys, many partially melted particles could be found, and they showed no direct contact with the outer edge of the fracture surface. The R_z value of the fatigue coupons is 431 μm which is similar to the roughness measurements from the HDH single-track top surfaces but significantly higher than the standard AM counterparts. Although the large R_z value may not reflect the likelihood of encountering crack-initiated surface

defects due to the presence of the partially melted particles, it is reasonable to argue that the as-built surface needs to be machined in order to further improve the fatigue performance of the HDH components [31].

7.4.2. Fatigue Life in the HIPed Condition

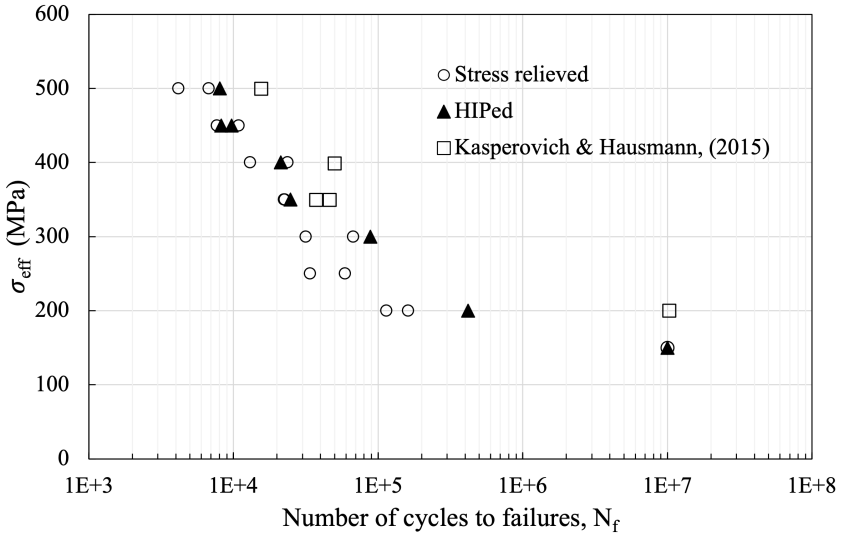

Figure 7.6 A Wöhler diagram comparing the uniaxial fatigue performance of the L-PBF built HDH TI-6Al-4V with the results reported by Kasperovich & Hausmann [134] *at various stress levels.*

To understand the role of internal porosity in crack initiation, a few HDH fatigue coupons were HIPed at 899 °C ± 14 °C and 1034 bar ± 34 bar for 2 hours. The results in this section remain incomplete and preliminary; the objective is to investigate if the crack initiation defects can be mitigated after HIPing treatment by comparing with the fatigue performance at the stress relieved condition. The microstructure of the HIPed HDH coupons is believed to be altered to fine lamellar α + β according to the study of Kasperovich & Hausmann [134] where the same HIPing conditions were applied. As shown by the S-N curves in Figure 7.6, the fatigue performances of the HDH coupons at the stress relieved and the HIPed conditions are similar.

Comparing with the results from Kasperovich & Hausmann [134], the improvement from the HIPing treatment also seems to be limited. That said, the importance of the internal pores was of secondary for fatigue crack initiation. Further investigations of fractography and microstructure need to be carried out in order to better understand how different factors influence the fatigue performance of the HDH coupons.

7.5. Conclusions & Hypothesis Revisited

This chapter shows that the fatigue performance of the L-PBF built HDH Ti-6Al-4V coupons is comparable to the standard AM counterparts in the stress relieved and the HIPed conditions. It further demonstrates that the effort directed at mitigating porosity in the as-built HDH components was able to control the defect size and population to the extent that limited impact on fatigue crack initiation was found.

Hypothesis 7.1. and *7.2.* were partially supported as the fatigue performance of the HDH components was comparable to the standard AM counterparts. On the other hand, the comparison against the wrought Ti-6Al-4V was not supported. The endurance limits of the wrought materials are often 3 to 4 times higher than 150 MPa. The rougher surface may be the major causal factor, as shown by the results in this chapter, for the weaker fatigue performance of the HDH components. Thus, testing coupons with a machined surface is strongly indicated for future work. Additionally, microstructure optimization can also be performed through post-processing heat treatment to further improve the coupons' resistance to fatigue crack initiation.

8. Conclusions

A wider adoption of AM requires better control of in-part defects and further reduction of fabrication cost. This study tackles both challenges by showing the successful applications of two non-standard powder feedstocks, i.e., the non-spherical HDH Ti-6Al-4V powder and the highly porous 17-4 PH stainless steel powder, in powder-based AM processes after parameter optimization. The process maps for these two materials were developed. The fatigue testing and the following characterization further demonstrated that the defect population was well-controlled by showing comparable performance as the standard AM components.

This is one of the pioneering efforts of using the synchrotron-based *in-situ* x-ray imaging technique to reveal the powder induced porosity formation process during laser melting. By coupling the imaging technique with the x-ray tomography and powder packing analysis tool, three powder induced porosity formation mechanisms were proposed. Melt pool dynamics, powder packing characteristics, and powder-laser interactions are believed to be key factors affecting the porosity formation.

9. Future Work

The proposed future work mainly focuses on two directions: i) further optimize part quality by developing a HDH powder batch with a better powder size distribution through powder mixing, and ii) evaluate the mechanical properties of the L-PBF built HDH Ti-6Al-4V with different post-processing heat treatments and surface conditions.

9.1. Optimization of Powder Size Distribution

As shown in the powder packing analysis, the HDH powder bed possessed a large population of low packing density spots which were not observed in the spherical counterparts. These spots could be the culprits for the formation of pores. Introducing finer HDH particles into the batch could potentially reduce the population of these spots which in turn reduce the related porosity formation. In fact, one ongoing collaboration with Professor Amir Mostafaei's group is to repeat the current study on a HDH powder batch with a much finer powder size distribution.

9.2. Mechanical Testing of L-PBF HDH Ti-6Al-4V Parts

Although the L-PBF built HDH Ti-6Al-4V showed comparable fatigue performance as the standard AM counterparts, it was still significantly weaker than the wrought/cast Ti-6Al-4V. The ongoing future work is to test the HDH coupons subjected to post-processing heat treatments and surface treatments so that the microstructure is optimized, and the surface defects are minimized. At this optimal sample condition, the residual porosity can be evaluated against the critical level for fatigue crack initiation.

References

[1] W.E. Frazier, Metal additive manufacturing: A review, J. Mater. Eng. Perform. 23 (2014) 1917–1928. https://doi.org/10.1007/s11665-014-0958-z.

[2] C.S. Lefky, B. Zucker, D. Wright, A.R. Nassar, T.W. Simpson, O.J. Hildreth, Dissolvable supports in powder bed fusion-printed stainless steel, 3D Print. Addit. Manuf. 4 (2017) 3–11. https://doi.org/10.1089/3dp.2016.0043.

[3] H.K. Rafi, N. V. Karthik, H. Gong, T.L. Starr, B.E. Stucker, Microstructures and mechanical properties of Ti6Al4V parts fabricated by selective laser melting and electron beam melting, J. Mater. Eng. Perform. 22 (2013) 3872–3883. https://doi.org/10.1007/s11665-013-0658-0.

[4] P. Sun, Z.Z. Fang, Y. Zhang, Y. Xia, Review of the methods for production of spherical Ti and Ti alloy powder, JOM. 69 (2017) 1853–1860. https://doi.org/10.1007/s11837-017-2513-5.

[5] D. Manfredi, F. Calignano, M. Krishnan, R. Canali, E. Ambrosio, E. Atzeni, From powders to dense metal parts: characterization of a commercial AlSiMg alloy processed through direct metal laser sintering, Materials (Basel). 6 (2013) 856–869. https://doi.org/10.3390/ma6030856.

[6] M. Sigl, S. Lutzmann, M.F. Zaeh, Transient physical effects in electron beam sintering, in: Int. Solid Free. Fabr. Symp., 2006: pp. 464–477.

[7] M. Kahnert, S. Lutzmann, M.F. Zaeh, Layer formations in electron beam sintering, in: Int. Solid Free. Fabr. Symp., 2017: pp. 88–99.

[8] X. Gong, T. Anderson, K. Chou, Review on powder-based electron beam additive manufacturing Technology, Manuf. Rev. 1 (2014). https://doi.org/10.1051/mfreview/2014001.

[9] C.G. McCracken, D.P. Barbis, R.C. Deeter, Powder characterisation: key titanium powder characteristics manufactured using the hydride-dehydride (HDH) process, in: Eur. PM Conf. Proc., The European Powder Metallurgy Association, 2010.

[10] O.D. Neikov, N.A. Yefimov, S.S. Naboychenko, Handbook of non-ferrous metal powders: technologies and applications, Elsevier, 2008.

[11] A. Heidloff, J. Rieken, I. Anderson, D. Byrd, Advancements in Ti alloy powder production by close-coupled gas atomization, Off. Sci. Tech. Inf. Tech. Reports. (2011). https://www.osti.gov/biblio/1024634 (accessed August 9, 2020).

[12] A.J. Heidloff, J.R. Rieken, I.E. Anderson, D. Byrd, J. Sears, M. Glynn, R.M. Ward, Advanced gas atomization processing for Ti and Ti alloy powder manufacturing, JOM. 62 (2010) 35–41. https://doi.org/10.1007/s11837-010-0075-x.

[13] S. Pleier, W. Goy, B. Schaub, M. Hohmann, M. Mede, R. Schumann, EIGA – an innovative production method for metal powder from reactive and refractory alloys, in: Adv. Powder Metall. Part. Mater., 2004.

[14] P. Loewenstein, Specialty powders by the rotating electrode process, Prog. Powder Metall. (1981) 9–21.

[15] M.I. Boulos, New frontiers in thermal plasmas from space to nanomaterials, Nucl. Eng. Technol. 44 (2012) 1–8. https://doi.org/10.5516/NET.77.2012.001.

[16] Y. Seki, S. Okamoto, H. Takigawa, N. Kawai, Effect of atomization variables on powder characteristics in the high-pressured water atomization process, Met. Powder Rep. 45 (1990) 38–40. https://doi.org/10.1016/S0026-0657(10)80014-1.

[17] D.P. Barbis, R.M. Gasior, G.P. Walker, J.A. Capone, T.S. Schaeffer, Titanium powders from the hydride-dehydride process, in: Titan. Powder Metall. Sci. Technol. Appl., Elsevier Inc., 2015: pp. 101–116. https://doi.org/10.1016/B978-0-12-800054-0.00007-1.
[18] F.H. Froes, O.N. Senkov, J.I. Qazi, Hydrogen as a temporary alloying element in titanium alloys: thermohydrogen processing, Int. Mater. Rev. 49 (2004) 227–245. https://doi.org/10.1179/095066004225010550.
[19] C.F. Yolton, Method for producing titanium particles, 1989.
[20] F. Medina, Reducing metal alloy powder costs for use in powder bed fusion additive manufacturing: improving the economics for production, 2013. https://scholarworks.utep.edu/open_etd/1678 (accessed August 9, 2020).
[21] V. Duz, A. Klevtsov, V. Sukhoplyuyev, Production of titanium powder, in: P. Samal, J. Newkirk (Eds.), Powder Metall., ASM International, 2015. https://doi.org/10.31399/asm.hb.v07.a0006078 (accessed August 9, 2020).
[22] J. Guzmán, R. de M. Nobre, E.R. Nunes, D.L. Bayerlein, R.B. Falcão, E. Sallica-Leva, J.B.F. Neto, H.R. Oliveira, V.L. Chastinet, F.J.G.L. Landgraf, Laser powder bed fusion parameters to produce high-density Ti-53%Nb alloy using irregularly shaped powder from hydride-dehydride (HDH) process, J. Mater. Res. Technol. (2020). https://doi.org/10.1016/j.jmrt.2020.12.084.
[23] O. Kanou, N. Fukada, S. Takenaka, The Use of HDH titanium alloypPowder for additive manufacturing application, J. Japan Soc. Powder Powder Metall. 64 (2017) 295–299. https://doi.org/10.2497/jjspm.64.295.
[24] W. Xu, S. Xiao, X. Lu, G. Chen, C. Liu, X. Qu, Fabrication of commercial pure Ti by selective laser melting using hydride-dehydride titanium powders treated by ball milling, J. Mater. Sci. Technol. 35 (2019) 322–327. https://doi.org/10.1016/j.jmst.2018.09.058.
[25] X. Yang, Z. Zhang, W. Gu, B. Wang, Y. Fan, Q. Miao, S. Zhao, B. Xie, Fabrication of ultra-low-cost pure Ti by selective laser melting using the mixed powders of hydride-dehydride titanium powders treated by ball milling and spherical powders, Powder Metall. (2020) 1–8. https://doi.org/10.1080/00325899.2020.1847848.
[26] R. Li, Y. Shi, Z. Wang, L. Wang, J. Liu, W. Jiang, Densification behavior of gas and water atomized 316L stainless steel powder during selective laser melting, Appl. Surf. Sci. 256 (2010) 4350–4356. https://doi.org/10.1016/j.apsusc.2010.02.030.
[27] A. Rogalsky, I. Rishmawi, L. Brock, M. Vlasea, Low cost irregular feed stock for laser powder bed fusion, J. Manuf. Process. 35 (2018) 446–456. https://doi.org/10.1016/j.jmapro.2018.08.032.
[28] B. Fullenwider, P. Kiani, J.M. Schoenung, K. Ma, Two-stage ball milling of recycled machining chips to create an alternative feedstock powder for metal additive manufacturing, Powder Technol. 342 (2019) 562–571. https://doi.org/10.1016/j.powtec.2018.10.023.
[29] P. Promoppatum, S.C. Yao, P.C. Pistorius, A.D. Rollett, P.J. Coutts, F. Lia, R. Martukanitz, Numerical modeling and experimental validation of thermal history and microstructure for additive manufacturing of an Inconel 718 product, Prog. Addit. Manuf. 3 (2018) 15–32. https://doi.org/10.1007/s40964-018-0039-1.
[30] P. Li, D.H. Warner, A. Fatemi, N. Phan, Critical assessment of the fatigue performance of additively manufactured Ti-6Al-4V and perspective for future research, Int. J. Fatigue. 85 (2016) 130–143. https://doi.org/10.1016/j.ijfatigue.2015.12.003.
[31] J.J. Lewandowski, M. Seifi, Metal additive manufacturing: a review of mechanical

properties, Annu. Rev. Mater. Res. 46 (2016) 151–186. https://doi.org/10.1146/annurev-matsci-070115-032024.
[32] R. Cunningham, C. Zhao, N. Parab, C. Kantzos, J. Pauza, K. Fezzaa, T. Sun, A.D. Rollett, Keyhole threshold and morphology in laser melting revealed by ultrahigh-speed x-ray imaging, Science (80-.). 363 (2019) 849–852. https://doi.org/10.1126/science.aav4687.
[33] C. Panwisawas, B. Perumal, R.M. Ward, N. Turner, R.P. Turner, J.W. Brooks, H.C. Basoalto, Keyhole formation and thermal fluid flow-induced porosity during laser fusion welding in titanium alloys: Experimental and modelling, Acta Mater. 126 (2017) 251–263. https://doi.org/10.1016/j.actamat.2016.12.062.
[34] W.E. King, H.D. Barth, V.M. Castillo, G.F. Gallegos, J.W. Gibbs, D.E. Hahn, C. Kamath, A.M. Rubenchik, Observation of keyhole-mode laser melting in laser powder-bed fusion additive manufacturing, J. Mater. Process. Technol. 214 (2014) 2915–2925. https://doi.org/10.1016/j.jmatprotec.2014.06.005.
[35] S.P. Narra, Melt pool geometry and microstructure control across alloys in metal based additive manufacturing processes, Carnegie Mellon University, 2017. https://doi.org/https://doi.org/10.1184/R1/6720569.v1.
[36] Z. Francis, The effects of laser and electron beam spot size in additive manufacturing processes, Carnegie Mellon University, 2017. https://doi.org/https://doi.org/10.1184/R1/6723563.v1.
[37] N.T. Aboulkhair, N.M. Everitt, I. Ashcroft, C. Tuck, Reducing porosity in AlSi10Mg parts processed by selective laser melting, Addit. Manuf. 1 (2014) 77–86. https://doi.org/10.1016/j.addma.2014.08.001.
[38] G. Kasperovich, J. Haubrich, J. Gussone, G. Requena, Correlation between porosity and processing parameters in TiAl6V4 produced by selective laser melting, Mater. Des. 105 (2016) 160–170. https://doi.org/10.1016/j.matdes.2016.05.070.
[39] J. Stef, A. Poulon-Quintin, A. Redjaimia, J. Ghanbaja, O. Ferry, M. De Sousa, M. Gouné, Mechanism of porosity formation and influence on mechanical properties in selective laser melting of Ti-6Al-4V parts, Mater. Des. 156 (2018) 480–493. https://doi.org/10.1016/j.matdes.2018.06.049.
[40] M. Tang, P.C. Pistorius, J.L. Beuth, Prediction of lack-of-fusion porosity for powder bed fusion, Addit. Manuf. 14 (2017) 39–48. https://doi.org/https://doi.org/10.1016/j.addma.2016.12.001.
[41] M. Naveed Ahsan, A.J. Pinkerton, R.J. Moat, J. Shackleton, A comparative study of laser direct metal deposition characteristics using gas and plasma-atomized Ti-6Al-4V powders, Mater. Sci. Eng. A. 528 (2011) 7648–7657. https://doi.org/10.1016/j.msea.2011.06.074.
[42] G.M. Janowski, F.S. Biancaniello, S.D. Ridder, Beneficial Effects of Nitrogen Atomization on an Austenitic Stainless Steel, Metall. Trans. A. 23 (1992) 3263–3272.
[43] R. Cunningham, A. Nicolas, J. Madsen, E. Fodran, E. Anagnostou, M.D. Sangid, A.D. Rollett, Analyzing the effects of powder and post-processing on porosity and properties of electron beam melted Ti-6Al-4V, Mater. Res. Lett. 5 (2017) 516–525. https://doi.org/10.1080/21663831.2017.1340911.
[44] W. Tan, Y.C. Shin, Multi-scale modeling of solidification and microstructure development in laser keyhole welding process for austenitic stainless steel, Comput. Mater. Sci. 98 (2015) 446–458. https://doi.org/10.1016/j.commatsci.2014.10.063.
[45] S.A. Khairallah, A.T. Anderson, A. Rubenchik, W.E. King, Laser powder-bed fusion additive manufacturing: Physics of complex melt flow and formation mechanisms of

pores, spatter, and denudation zones, Acta Mater. 108 (2016) 36–45. https://doi.org/10.1016/j.actamat.2016.02.014.
[46] L. Scime, J. Beuth, Anomaly detection and classification in a laser powder bed additive manufacturing process using a trained computer vision algorithm, Addit. Manuf. 19 (2018) 114–126. https://doi.org/10.1016/j.addma.2017.11.009.
[47] S.A. Shevchik, C. Kenel, C. Leinenbach, K. Wasmer, Acoustic emission for in situ quality monitoring in additive manufacturing using spectral convolutional neural networks, Addit. Manuf. 21 (2018) 598–604. https://doi.org/10.1016/j.addma.2017.11.012.
[48] N.V.Y. Scarlett, P. Tyson, D. Fraser, S. Mayo, A. Maksimenko, Synchrotron x-ray CT characterization of titanium parts fabricated by additive manufacturing. Part I. Morphology, J. Synchrotron Radiat. 23 (2016) 1006–1014. https://doi.org/10.1107/S1600577516007359.
[49] N.V.Y. Scarlett, P. Tyson, D. Fraser, S. Mayo, A. Maksimenko, Synchrotron X-ray CT characterization of titanium parts fabricated by additive manufacturing. Part II. Defects, J. Synchrotron Radiat. 23 (2016) 1015–1023. https://doi.org/10.1107/S1600577516008018.
[50] S. Tammas-Williams, H. Zhao, F. Léonard, F. Derguti, I. Todd, P.B. Prangnell, XCT analysis of the influence of melt strategies on defect population in Ti-6Al-4V components manufactured by selective electron beam melting, Mater. Charact. 102 (2015) 47–61. https://doi.org/10.1016/j.matchar.2015.02.008.
[51] R. Cunningham, S.P. Narra, C. Montgomery, J. Beuth, A.D. Rollett, Synchrotron-based x-ray microtomography characterization of the effect of processing variables on porosity formation in laser power-bed additive manufacturing of Ti-6Al-4V, JOM. 69 (2017) 479–484. https://doi.org/10.1007/s11837-016-2234-1.
[52] S. Tammas-Williams, P. Prangnell, I. Todd, F. Léonard, S. Tammas-Williams, P.B. Prangnell, I. Todd, P.J. Withers, Assessment by x-ray CT of the effects of geometry and build direction on defects in titanium ALM parts, in: Conf. Ind. Comput. Tomogr., 2012.
[53] C. Kantzos, J. Pauza, R. Cunningham, S.P. Narra, J. Beuth, A. Rollett, An investigation of process parameter modifications on additively manufactured inconel 718 parts, J. Mater. Eng. Perform. 28 (2019) 620–626. https://doi.org/10.1007/s11665-018-3612-3.
[54] W. Tillmann, C. Schaak, J. Nellesen, M. Schaper, M.E. Aydinöz, K.-P. Hoyer, Hot isostatic pressing of IN718 components manufactured by selective laser melting, Addit. Manuf. 13 (2017) 93–102. https://doi.org/10.1016/j.addma.2016.11.006.
[55] B.A. Dowd, G.H. Campbell, D.P. Siddons, R.B. Marr, Developments in synchrotron x-ray computed microtomography at the national synchrotron light source, in: Proc. SPIE 3772, Dev. X-Ray Tomogr. II, 1999: pp. 224–236. https://doi.org/https://doi.org/10.1117/12.363725.
[56] A. Mostafaei, C. Hilla, E.L. Stevens, P. Nandwana, A.M. Elliott, M. Chmielus, Comparison of characterization methods for differently atomized nickel-based alloy 625 powders, Powder Technol. 333 (2018) 180–192. https://doi.org/10.1016/j.powtec.2018.04.014.
[57] K. Heim, F. Bernier, R. Pelletier, L.P. Lefebvre, High resolution pore size analysis in metallic powders by X-ray tomography, Case Stud. Nondestruct. Test. Eval. 6 (2016) 45–52. https://doi.org/10.1016/j.csndt.2016.09.002.
[58] C. Zhao, K. Fezzaa, R. Cunningham, H. Wen, F. De Carlo, L. Chen, A.D. Rollett, T. Sun, Real-time monitoring of laser powder bed fusion process using high-speed x-ray imaging and diffraction, Sci. Rep. 7 (2017). https://doi.org/https://doi.org/10.1038/s41598-017-

03761-2.
[59] N.D. Parab, C. Zhao, R. Cunningham, L.I. Escano, K. Fezzaa, W. Everhart, A.D. Rollett, L. Chen, T. Sun, Ultrafast x-ray imaging of laser–metal additive manufacturing processes, J. Synchrotron Radiat. 25 (2018) 1467–1477. https://doi.org/10.1107/S1600577518009554.
[60] Q. Guo, C. Zhao, M. Qu, L. Xiong, L.I. Escano, S. Mohammad, H. Hojjatzadeh, N.D. Parab, K. Fezzaa, W. Everhart, T. Sun, L. Chen, In-situ characterization and quantification of melt pool variation under constant input energy density in laser powder bed fusion additive manufacturing process, Addit. Manuf. 28 (2019) 600–609. https://doi.org/10.1016/j.addma.2019.04.021.
[61] C. Zhao, N.D. Parab, X. Li, K. Fezzaa, W. Tan, A.D. Rollett, T. Sun, Critical instability at moving keyhole tip generates porosity in laser melting, Science (80-.). 370 (2020) 1080–1086. https://doi.org/10.1126/science.abd1587.
[62] P.J. Chiang, R. Jiang, R. Cunningham, N. Parab, C. Zhao, K. Fezzaa, T. Sun, A.D. Rollett, In situ characterization of hot cracking using dynamic x-ray radiography, in: Adv. Real Time Imaging II, Springer International Publishing, 2019: pp. 77–85. https://doi.org/10.1007/978-3-030-06143-2_8.
[63] C. Lun, A. Leung, S. Marussi, M. Towrie, R.C. Atwood, P.J. Withers, P.D. Lee, The effect of powder oxidation on defect formation in laser additive manufacturing, Acta Mater. 166 (2019). https://doi.org/10.1016/j.actamat.2018.12.027.
[64] A.A. Martin, N.P. Calta, S.A. Khairallah, J. Wang, P.J. Depond, A.Y. Fong, V. Thampy, G.M. Guss, A.M. Kiss, K.H. Stone, C.J. Tassone, J. Nelson Weker, M.F. Toney, T. van Buuren, M.J. Matthews, Dynamics of pore formation during laser powder bed fusion additive manufacturing, Nat. Commun. 10 (2019) 1–10. https://doi.org/10.1038/s41467-019-10009-2.
[65] S.M.H. Hojjatzadeh, N.D. Parab, W. Yan, Q. Guo, L. Xiong, C. Zhao, M. Qu, L.I. Escano, X. Xiao, K. Fezzaa, W. Everhart, T. Sun, & L. Chen, Pore elimination mechanisms during 3D printing of metals, Nat. Commun. 10 (2019). https://doi.org/10.1038/s41467-019-10973-9.
[66] S.M.H. Hojjatzadeh, N.D. Parab, Q. Guo, M. Qu, L. Xiong, C. Zhao, L.I. Escano, K. Fezzaa, W. Everhart, T. Sun, L. Chen, Direct observation of pore formation mechanisms during LPBF additive manufacturing process and high energy density laser welding, Int. J. Mach. Tools Manuf. 153 (2020). https://doi.org/10.1016/j.ijmachtools.2020.103555.
[67] C. Kenel, D. Grolimund, X. Li, E. Panepucci, V.A. Samson, D.F. Sanchez, F. Marone, C. Leinenbach, In situ investigation of phase transformations in Ti-6Al-4V under additive manufacturing conditions combining laser melting and high-speed micro-X-ray diffraction, Sci. Rep. 7 (2017) 1–10. https://doi.org/10.1038/s41598-017-16760-0.
[68] L.I. Escano, N.D. Parab, L. Xiong, Q. Guo, C. Zhao, K. Fezzaa, W. Everhart, T. Sun, L. Chen, Revealing particle-scale powder spreading dynamics in powder-bed-based additive manufacturing process by high-speed x-ray imaging, Sci. Rep. 8 (2018) 1–11. https://doi.org/10.1038/s41598-018-33376-0.
[69] Q. Guo, C. Zhao, L.I. Escano, Z. Young, L. Xiong, K. Fezzaa, W. Everhart, B. Brown, T. Sun, L. Chen, Transient dynamics of powder spattering in laser powder bed fusion additive manufacturing process revealed by in-situ high-speed high-energy x-ray imaging, Acta Mater. 151 (2018) 169–180. https://doi.org/10.1016/j.actamat.2018.03.036.
[70] A. Uriondo, M. Esperon-Miguez, S. Perinpanayagam, The present and future of additive

manufacturing in the aerospace sector: A review of important aspects, Proc. Inst. Mech. Eng. Part G J. Aerosp. Eng. 229 (2015) 2132–2147. https://doi.org/10.1177/0954410014568797.

[71] E. Uhlmann, R. Kersting, T.B. Klein, M.F. Cruz, A.V. Borille, Additive manufacturing of titanium alloy for aircraft components, in: Procedia CIRP, Elsevier B.V., 2015: pp. 55–60. https://doi.org/10.1016/j.procir.2015.08.061.

[72] M. Geetha, A.K. Singh, R. Asokamani, A.K. Gogia, Ti based biomaterials, the ultimate choice for orthopaedic implants - A review, Prog. Mater. Sci. 54 (2009) 397–425. https://doi.org/10.1016/j.pmatsci.2008.06.004.

[73] M. Abdel-Hady Gepreel, M. Niinomi, Biocompatibility of Ti-alloys for long-term implantation, J. Mech. Behav. Biomed. Mater. 20 (2013) 407–415. https://doi.org/10.1016/j.jmbbm.2012.11.014.

[74] M. Yan, Microstructural characterization of as-sintered titanium and titanium alloys, in: Titan. Powder Metall. Sci. Technol. Appl., Elsevier Inc., 2015: pp. 555–578. https://doi.org/10.1016/B978-0-12-800054-0.00029-0.

[75] C. Leyens, M. Peters, Titanium and titanium alloys, Wiley-VCH Verlag GmbH & Co. KGaA, 2003.

[76] T. Ahmed, H.J. Rack, Phase transformations during cooling in α + β titanium alloys, Mater. Sci. Eng. A. 243 (1998) 206–211. https://doi.org/10.1016/s0921-5093(97)00802-2.

[77] S.M. Kelly, S.L. Kampe, Microstructural evolution in laser-deposited multilayer Ti-6Al-4V builds: Part II. Thermal modeling, Metall. Mater. Trans. A. 35A (2004) 1869–1879. https://doi.org/https://doi.org/10.1007/s11661-004-0095-7.

[78] R. Ding, Z.X. Guo, A. Wilson, Microstructural evolution of a Ti-6Al-4V alloy during thermomechanical processing, Mater. Sci. Eng. A. 327 (2002) 233–245. https://doi.org/10.1016/S0921-5093(01)01531-3.

[79] L. Thijs, F. Verhaeghe, T. Craeghs, J. Van Humbeeck, J.P. Kruth, A study of the microstructural evolution during selective laser melting of Ti-6Al-4V, Acta Mater. 58 (2010) 3303–3312. https://doi.org/10.1016/j.actamat.2010.02.004.

[80] X. Zhao, S. Li, M. Zhang, Y. Liu, T.B. Sercombe, S. Wang, Y. Hao, R. Yang, L.E. Murr, Comparison of the microstructures and mechanical properties of Ti-6Al-4V fabricated by selective laser melting and electron beam melting, Mater. Des. 95 (2016) 21–31. https://doi.org/10.1016/j.matdes.2015.12.135.

[81] B. Vrancken, L. Thijs, J.P. Kruth, J. Van Humbeeck, Heat treatment of Ti6Al4V produced by Selective Laser Melting: Microstructure and mechanical properties, J. Alloys Compd. 541 (2012) 177–185. https://doi.org/10.1016/j.jallcom.2012.07.022.

[82] T. Vilaro, C. Colin, J.D. Bartout, As-fabricated and heat-treated microstructures of the Ti-6Al-4V alloy processed by selective laser melting, Metall. Mater. Trans. A Phys. Metall. Mater. Sci. 42 (2011) 3190–3199. https://doi.org/10.1007/s11661-011-0731-y.

[83] J. Yang, H. Yu, J. Yin, M. Gao, Z. Wang, X. Zeng, Formation and control of martensite in Ti-6Al-4V alloy produced by selective laser melting, Mater. Des. 108 (2016) 308–318. https://doi.org/10.1016/j.matdes.2016.06.117.

[84] B. Wysocki, P. Maj, A. Krawczyńska, K. Rożniatowski, J. Zdunek, K.J. Kurzydłowski, W. Święszkowski, Microstructure and mechanical properties investigation of CP titanium processed by selective laser melting (SLM), J. Mater. Process. Technol. 241 (2017) 13–23. https://doi.org/10.1016/j.jmatprotec.2016.10.022.

[85] N. Kazantseva, P. Krakhmalev, M. Thuvander, I. Yadroitsev, N. Vinogradova, I. Ezhov,

Martensitic transformations in Ti-6Al-4V (ELI) alloy manufactured by 3D Printing, Mater. Charact. 146 (2018) 101–112. https://doi.org/10.1016/j.matchar.2018.09.042.
[86] W. Xu, M. Brandt, S. Sun, J. Elambasseril, Q. Liu, K. Latham, K. Xia, M. Qian, Additive manufacturing of strong and ductile Ti-6Al-4V by selective laser melting via in situ martensite decomposition, Acta Mater. 85 (2015) 74–84. https://doi.org/10.1016/j.actamat.2014.11.028.
[87] A. Zafari, M.R. Barati, K. Xia, Controlling martensitic decomposition during selective laser melting to achieve best ductility in high strength Ti-6Al-4V, Mater. Sci. Eng. A. 744 (2019) 445–455. https://doi.org/10.1016/j.msea.2018.12.047.
[88] L.E. Murr, E. V. Esquivel, S.A. Quinones, S.M. Gaytan, M.I. Lopez, E.Y. Martinez, F. Medina, D.H. Hernandez, E. Martinez, J.L. Martinez, S.W. Stafford, D.K. Brown, T. Hoppe, W. Meyers, U. Lindhe, R.B. Wicker, Microstructures and mechanical properties of electron beam-rapid manufactured Ti-6Al-4V biomedical prototypes compared to wrought Ti-6Al-4V, Mater. Charact. 60 (2009) 96–105. https://doi.org/10.1016/j.matchar.2008.07.006.
[89] K. Puebla, L.E. Murr, S.M. Gaytan, E. Martinez, F. Medina, R.B. Wicker, Effect of melt scan eate on microstructure and macrostructure for electron beam melting of Ti-6Al-4V, Mater. Sci. Appl. 3 (2012) 259–264. https://doi.org/10.4236/msa.2012.35038.
[90] P.A. Kobryn, S.L. Semiatin, Microstructure and texture evolution during solidification processing of Ti-6A1-4V, J. Mater. Process. Technol. 135 (2003) 330–339. https://doi.org/10.1016/S0924-0136(02)00865-8.
[91] S.P. Narra, R. Cunningham, J. Beuth, A.D. Rollett, Location specific solidification microstructure control in electron beam melting of Ti-6Al-4V, Addit. Manuf. 19 (2018) 160–166. https://doi.org/10.1016/j.addma.2017.10.003.
[92] L.E. Murr, E. Martinez, J. Hernandez, S. Collins, K.N. Amato, S.M. Gaytan, P.W. Shindo, Microstructures and properties of 17-4 PH stainless steel fabricated by selective laser melting, J. Mater. Res. Technol. 1 (2012) 167–177. https://doi.org/10.1016/S2238-7854(12)70029-7.
[93] H. Gu, H. Gong, D. Pal, K. Rafi, T. Starr, B. Stucker, Influences of energy density on porosity and microstructure of selective laser melted 17- 4PH stainless steel, in: Proc. 24th Annu. Int. Solid Free. Fabr. Symp., 2013.
[94] H.K. Rafi, D. Pal, N. Patil, T.L. Starr, B.E. Stucker, Microstructure and mechanical behavior of 17-4 precipitation hardenable steel processed by selective laser melting, J. Mater. Eng. Perform. 23 (2014) 4421–4428. https://doi.org/10.1007/s11665-014-1226-y.
[95] L. Facchini, N. Vicente, I. Lonardelli, E. Magalini, P. Robotti, M. Alberto, Metastable austenite in 17-4 precipitation-hardening stainless steel produced by selective laser melting, Adv. Eng. Mater. 12 (2010) 184–188. https://doi.org/10.1002/adem.200900259.
[96] J. Beuth, J. Fox, J. Gockel, R. Yang, H. Qiao, E. Soylemez, P. Reeseewatt, A. Anvari, S. Narra, N. Klingbeil, Process mapping for qualification across multiple direct metal additive manufacturing processes, in: Solid Free. Fabr. Symp., 2013.
[97] D. Rosenthal, Mathematical theory of heat distribution during welding and cutting, Weld. J. (1941). https://ci.nii.ac.jp/naid/10014566598/ (accessed February 12, 2020).
[98] M.H. McKetty, The AAPM/RSNA physics tutorial for residents: X-ray attenuation, Radiographics. 18 (1998) 151–163. https://doi.org/10.1148/radiographics.18.1.9460114.
[99] A. Thompson, I. Maskery, R.K. Leach, X-ray computed tomography for additive manufacturing: a review, Meas. Sci. Technol. 27 (2016) 072001.

https://doi.org/10.1088/0957-0233/27/7/072001.
[100] J. Radon, On the determination of functions from their integral values along certain manifolds, IEEE Trans. Med. Imaging. MI–5 (1986) 170–176. https://doi.org/10.1109/TMI.1986.4307775.
[101] M. van Ginkel, C.L. Luengo Hendriks, L.J. van Vliet, A short introduction to the Radon and Hough transforms and how they relate to each other, 2004.
[102] F. Marone, B. Münch, M. Stampanoni, Fast reconstruction algorithm dealing with tomography artifacts, in: S.R. Stock (Ed.), Dev. X-Ray Tomogr. VII, SPIE, 2010: p. 780410. https://doi.org/10.1117/12.859703.
[103] F. Natterer, 5. Reconstruction algorithms, in: Math. Comput. Tomogr., Society for Industrial and Applied Mathematics, 2001: pp. 102–157. https://doi.org/10.1137/1.9780898719284.ch5.
[104] A. Dogra, P. Bhalla, Image sharpening by gaussian and butterworth high pass filter, Biomed. Pharmacol. J. 7 (2014) 707–713. https://doi.org/10.13005/bpj/545.
[105] M.L. Rivers, tomoRecon: High-speed tomography reconstruction on workstations using multi-threading, in: Dev. X-Ray Tomogr. VIII, SPIE, 2012: p. 85060U. https://doi.org/10.1117/12.930022.
[106] A. Kak, M.S.-A.M. Philadelphia, U. PA, U. Society, U. 2001, Principles of computerized tomographic imaging, Med. Phys. 29 (2002) 107–107.
[107] R.N. Bracewell, Numerical transforms, Science (80-.). 248 (1990) 697. https://doi.org/10.1126/science.248.4956.697.
[108] A. Mirone, E. Gouillart, E. Brun, P. Tafforeau, J. Kieffer, The PyHST2 hybrid distributed code for high speed tomographic reconstruction with iterative reconstruction and a priori knowledge capabilities, Nucl. Instruments Methods Phys. Res. Sect. B Beam Interact. with Mater. Atoms. 324 (2014) 41–48. https://doi.org/https://doi.org/10.1016/j.nimb.2013.09.030.
[109] A. Biguri, M. Dosanjh, S. Hancock, M. Soleimani, TIGRE: a MATLAB-GPU toolbox for CBCT image reconstruction, Biomed. Phys. Eng. Express. 2 (2016) 055010.
[110] L. Vincent, P. Soille, Watersheds in digital spaces: an efficient algorithm based on immersion simulations, IEEE Trans. Pattern Anal. Mach. Intell. 13 (1991) 583–598. https://doi.org/10.1109/34.87344.
[111] D. Gürsoy, F. De Carlo, X. Xiao, C. Jacobsen, TomoPy: A framework for the analysis of synchrotron tomographic data, 21 (2014) 1188–1193. https://doi.org/10.1107/S1600577514013939.
[112] T. Mahale, Electron beam melting of advanced materials and structures, mass customization, mass personalization, 2009. https://repository.lib.ncsu.edu/handle/1840.16/4943 (accessed August 9, 2020).
[113] ASTM B962-17, Standard test methods for density of compacted or sintered powder metallurgy (PM) products using Archimedes' principle, West Conshohocken, 2017. https://doi.org/10.1520/B0962-14.
[114] EOS GmbH, Material data sheet for EOS titanium Ti64, 2016.
[115] H. Hou, C.C. Sun, Quantifying effects of particulate properties on powder flow properties using a ring shear tester, J. Pharm. Sci. 97 (2008) 4030–4039. https://doi.org/10.1002/jps.21288.
[116] S.K. Wilkinson, S.A. Turnbull, Z. Yan, E.H. Stitt, M. Marigo, A parametric evaluation of powder flowability using a Freeman rheometer through statistical and sensitivity analysis:

A discrete element method (DEM) study, Comput. Chem. Eng. 97 (2017) 161–174. https://doi.org/https://doi.org/10.1016/j.compchemeng.2016.11.034.

[117] A.V. Gusarov, I. Smurov, Modeling the interaction of laser radiation with powder bed at selective laser melting, Phys. Procedia. 5 (2010) 381–394. https://doi.org/https://doi.org/10.1016/j.phpro.2010.08.065.

[118] D. Gu, Y. Shen, Balling phenomena in direct laser sintering of stainless steel powder: Metallurgical mechanisms and control methods, Mater. Des. 30 (2009) 2903–2910. https://doi.org/https://doi.org/10.1016/j.matdes.2009.01.013.

[119] R. Cunningham, S.P. Narra, T. Ozturk, J. Beuth, A.D. Rollett, Evaluating the effect of processing parameters on porosity in electron beam melted Ti-6Al-4V via synchrotron X-ray microtomography, JOM. 68 (2016) 765–771. https://doi.org/10.1007/s11837-015-1802-0.

[120] A.B. Spierings, M. Voegtlin, T. Bauer, K. Wegener, Powder flowability characterisation methodology for powder-bed-based metal additive manufacturing, Prog. Addit. Manuf. 1 (2016) 9–20. https://doi.org/10.1007/s40964-015-0001-4.

[121] G.N. Sankin, W.N. Simmons, S.L. Zhu, P. Zhong, Shock wave interaction with laser-generated single bubbles, Phys. Rev. Lett. 95 (2005) 1–4. https://doi.org/10.1103/PhysRevLett.95.034501.

[122] L. Scime, Methods for the expansion of additive manufacturing process space and the development of in-situ process monitoring methodologies, Carnegie Mellon University, 2018.

[123] R. Al-Raoush, K.A. Alshibli, Distribution of local void ratio in porous media systems from 3D X-ray microtomography images, Phys. A Stat. Mech. Its Appl. 361 (2006) 441–456. https://doi.org/10.1016/j.physa.2005.05.043.

[124] F.H. Kim, D. Penumadu, J. Gregor, N. Kardjilov, I. Manke, High-resolution neutron and x-ray imaging of granular materials, J. Geotech. Geoenvironmental Eng. 139 (2013) 715–723. https://doi.org/10.1061/(asce)gt.1943-5606.0000809.

[125] L. Sinclair, C.L.A. Leung, S. Marussi, S.J. Clark, Y. Chen, M.P. Olbinado, A. Rack, J. Gardy, G.J. Baxter, P.D. Lee, In situ radiographic and ex situ tomographic analysis of pore interactions during multilayer builds in laser powder bed fusion, Addit. Manuf. 36 (2020) 101512. https://doi.org/10.1016/j.addma.2020.101512.

[126] S.A. Khairallah, A.A. Martin, J.R.I. Lee, G. Guss, N.P. Calta, J.A. Hammons, M.H. Nielsen, K. Chaput, E. Schwalbach, M.N. Shah, M.G. Chapman, T.M. Willey, A.M. Rubenchik, A.T. Anderson, Y. Morris Wang, M.J. Matthews, W.E. King, Controlling interdependent meso-nanosecond dynamics and defect generation in metal 3D printing, Science (80-.). 368 (2020) 660–665. https://doi.org/10.1126/science.aay7830.

[127] Z. Hu, H. Zhu, H. Zhang, X. Zeng, Experimental investigation on selective laser melting of 17-4PH stainless steel, Opt. Laser Technol. 87 (2017) 17–25. https://doi.org/10.1016/j.optlastec.2016.07.012.

[128] J. Pegues, M. Roach, R.S. Williamson, N. Shamsaei, Surface roughness effects on the fatigue strength of additively manufactured Ti-6Al-4V, Int. J. Fatigue. 116 (2018) 543–552. https://doi.org/10.1016/j.ijfatigue.2018.07.013.

[129] P. Edwards, M. Ramulu, Fatigue performance evaluation of selective laser melted Ti-6Al-4V, Mater. Sci. Eng. A. 598 (2014) 327–337. https://doi.org/10.1016/j.msea.2014.01.041.

[130] E. Wycisk, A. Solbach, S. Siddique, D. Herzog, F. Walther, C. Emmelmann, Effects of defects in laser additive manufactured Ti-6Al-4V on fatigue properties, Phys. Procedia. 56

(2014) 371–378. https://doi.org/10.1016/j.phpro.2014.08.120.
[131] Metallic materials properties development and standardization (MMPDS-05), 2010. https://app.knovel.com/hotlink/toc/id:kpMMPDSM11/metallic-materials-properties/metallic-materials-properties.
[132] R.W. Hertzberg, Deformation and fracture mechanics of engineering materials, 4th ed., John Wiley and Sons Inc., Hoboken, NJ, 1995.
[133] C.A. Kantzos, R.W. Cunningham, V. Tari, A.D. Rollett, Characterization of metal additive manufacturing surfaces using synchrotron X-ray CT and micromechanical modeling, Comput. Mech. 61 (2018) 575–580. https://doi.org/10.1007/s00466-017-1531-z.
[134] G. Kasperovich, J. Hausmann, Improvement of fatigue resistance and ductility of TiAl6V4 processed by selective laser melting, J. Mater. Process. Technol. 220 (2015) 202–214. https://doi.org/10.1016/j.jmatprotec.2015.01.025.